Adaptive Collocated Feedback for Noise Absorption in Acoustic Enclosures

by

M. Austin Creasy

Thesis submitted to the Faculty of the
Virginia Polytechnic Institute and State University
in partial fulfillment of the requirements for the degree of

Master of Science
in
Mechanical Engineering

Donald J. Leo, Chair
James P. Carneal
Daniel J. Inman
Martin E. Johnson

October 2006
Blacksburg, Virginia

Keywords: Acoustic Enclosure, Acoustics, Fairing, Feedback Control, Payload, PPF Control

Copyright
by
M. Austin Creasy
2006

Adaptive Collocated Feedback for Noise Absorption in Acoustic Enclosures

by

M. Austin Creasy

Abstract

This thesis focuses on adaptive feedback control for low frequency acoustic energy absorption in acoustic enclosures. The specific application chosen for this work is the reduction of high interior sound pressure levels (SPL) experienced during launch within launch vehicle payload fairings. Two acoustic enclosures are used in the research: the first being a symmetric cylindrical duct and the other being a full scale model of a payload fairing. The symmetric cylindrical duct is used to validate the ability of the adaptive controller to compensate for large changes in the interior acoustical properties. The payload fairing is used to validate that feedback control, for a large geometry, does absorb acoustic energy.

The feedback controller studied in this work is positive position feedback (PPF) used in conjunction with high and low pass Butterworth filters. An algorithm is formed from control experiments for setting the filter parameters of the PPF and Butterworth filters from non-adaptive control simulations and tests of the duct and payload fairing. This non-adaptive control shows internal SPL reductions of 2.2 dB in the cylindrical duct for the frequency range from 100 to 500 Hz and internal SPL reductions of 4.2 dB in the full scale fairing model for the frequency range from 50 to 250 Hz.

The experimentally formed control algorithm is then used as the basis for an adaptive controller that uses the collocated feedback signal to actively tune the control parameters. The cylindrical duct enclosure with a movable end cap is used to test the

adaptation properties of the controller. The movable end cap allows the frequencies of the acoustic modes to vary by more than 20 percent. Experiments show that a 10 percent change in the frequencies of the acoustic modes cause the closed-loop system to go unstable with a non-adaptive controller. The closed-loop system with the adaptive controller maintains stability and reduces the SPL throughout the 20 percent change of the acoustic modes' frequencies with a 2.3 dB SPL reduction before change and a 1.7 dB SPL reduction after the 20 percent change.

Acknowledgments

I would like to first thank Dr. Donald J. Leo for agreeing to be my advisor. His patience and encouragement was essential to the completion of this work. I would like to thank Dr. James P. Carneal, Dr. Daniel J. Inman, and Dr. Martin E. Johnson for serving on my advisory committee, with a special thanks to Dr. Carneal for answering all my acoustic questions at the beginning of this work and to Dr. Inman for showing me that graduate school can be enjoyable. I want to thank everyone at CIMSS for their help and for letting me take some of the equipment out of the lab for an extended period of time. A special thanks goes to Dr. Henry Sodano for helping me get started on my first experiments and to Vishnu Sundaresan for helping with computer updates. I want to thank Dr. Kevin Farinholt for all his input, help, and patience with this project and for being a good friend. I appreciate the support from Nanosonic, Inc. under purchase order 414969.

And most important of all I want to thank my wife, Mary, for being willing to support me and return to school and the student life again. Thanks for your love and support and for being my best friend in the world. I also want to thank Kate and Eliza for letting me take a little time from being Dad to compile this research into this document.

Finally, I want to thank my parents, bother, and sisters for helping shape who I am today.

Contents

List of Tables

List of Figures

Nomenclature

a - cylindrical duct radius or transfer function constant

$\boldsymbol{A}$,$\boldsymbol{B}$ - amplitude coefficients of pressure equation

A,B,C,D,E,F,G - transfer function coefficients

B - magnetic flux density

$B_{l\_2\_butter}$ - transfer function of 2nd order low-pass Butterworth filter

c - speed of sound in air

c_p - specific heat at constant pressure

dB - decibel

$\boldsymbol{F}$ - force

F_{1_butter} - 1st order Butterworth filter used to model amplifier dynamics

FFT - fast Fourier transform

FRF - frequency response function

f_{rN} - relaxation frequency of molecular nitrogen

f_{rO} - relaxation frequency of molecular oxygen

G - collocated plant transfer function

g - gain

G_1 - transfer function of middle location over collocated location

G_2 - transfer function of end location over collocated location

G_h - discretized 6th order high-pass Butterworth filter transfer function

$G_{h\_6\_butter}$ - transfer function of 6th order high-pass Butterworth filter

G_{h_butter} - high-pass Butterworth filter transfer function

G_l - discretized 2nd order low-pass Butterworth filter transfer function

G_{l_butter} - low-pass Butterworth filter transfer function

H - compensator transfer function

h - molar concentration of water vapor

H_1 - closed-loop transfer function of collocated location

H_2 - Closed-loop Transfer Function of P_2/V_i or P_2/V_e

H_3 - Closed-loop Transfer Function of P_3/V_i or P_3/V_e

hr - relative humidity

Hz - hertz

i - current

j - imaginary variable

k or $\boldsymbol{k}$ - wave number

K - PPF filter transfer function

K_i - PPF filter transfer function defined for a particular mode

K_{ppf} - multiple PPF transfer function added together

K_t - combined filter transfer function added together

L - duct length or electrical inductance

l - speaker wire length

L_e - speaker electrical inductance

m - actuator mass

m_{air} - air mass

m_s - dynamic speaker mass

mV - millivolt

n - order of a system

$\boldsymbol{p}$ - pressure

P_1 - pressure measurement of location 1

P_2 - pressure measurement of location 2

P_3 - pressure measurement of location 3

P_4 - pressure measurement of location 4

Pa - Pascal

PPF - positive position feedback

pr - Prandtl number

p_{ref} - reference pressure

p_s - atmospheric pressure

p_{s0} - reference atmospheric pressure

p_{sat} - saturated vapor pressure

p_t - total pressure

$p_{t\_control}$ - total pressure of controlled system

p_{t_ref} - total pressure of baseline system

R - mechanical damping or electrical resistance

R_e - speaker electrical resistance

RMS - root mean square

S - cylindrical duct area

s - mechanical stiffness or Laplace variable

SPL - sound pressure level

$SPL_{reduction}$ - sound pressure level reduction

t - time

T - time step or temperature

T_0 - reference atmospheric temperature

T_{01} - triple-point isotherm temperature

$\boldsymbol{u}$ - particle speed

V - volt

V_e - external disturbance

V_i - internal disturbance

x - location along duct

z - discrete Transfer Function variable

$\boldsymbol{Z}$ - impedance

$\boldsymbol{Z_a}$ - radiation impedance

$\boldsymbol{Z_e}$ - electrical impedance

$\boldsymbol{Z_m}$ - mechanical impedance

α - absorption coefficient or closed-loop pole spacing

α_k - thermal conduction absorption

α_m - molecular thermal relaxation absorption

α_s - spatial absorption

α_w - wall losses absorption

γ - ratio of specific heats

ζ - damping ratio

ζ_{CL} - closed-loop damping ratio

ζ_f or ζ_p - PPF filter damping ratio

η - filter coordinate or coefficient of shear viscosity

η_B - coefficient of bulk viscosity

θ - angle in degrees

κ - thermal conductivity

ξ - modal coordinate

ρ - air density

τ_s - relaxation time

ω - frequency (rad/s)

ω_{fp} - ratio of the PPF filter frequency to the pole frequency

ω_{pz} - ratio of the zero to the pole

Chapter 1

Introduction

1.1 Motivation

Satellite systems are subjected to the most strenuous loads that they will be exposed to in their lifetime during the first several minutes of launch due to the severe vibroacoustic environment in the launch vehicle payload fairing. Intense vibration and acoustic levels are caused by the airflow along the walls of the fairing and the booster (Kemp and Clark, 2003), the rocket engines (Lane *et al.*., 2006), rocket exhaust wave reflections from the ground (Estève, 2004), and shocks experienced during stage separations (Kemp and Clark, 2003). All these vibration and acoustic loads need to be accounted for in the structural design of the satellite.

Figure 1.1 shows a picture of a payload fairing used for launching the Cassini spacecraft on a Titan IVB/Centaur rocket (Courtesy of NASA/JPL-Caltech). The purpose of the fairing is to protect the spacecraft from damage during launch until deployment in space. With launch cost estimates of $10,000 to $12,000 per pound (Farinholt, 2001), any decrease in weight significantly reduces the cost of launching the satellite system but increases vibration and internal sound pressure level (SPL) where the SPL currently experienced by a payload during launch ranges between 120 and 160 decibels (dB) (Kemp and Clark, 2003, Kidner *et al*., 2006, Lane *et al*., 2006). The SPL in the internal enclosure of a fairing has increased as designers, in order to reduce the system weight, have moved from conventional materials that limit noise transmission at low frequency to composite materials which decreases structural damping and increases noise transmission at low frequency. Therefore a tradeoff between cost and SPL is made.

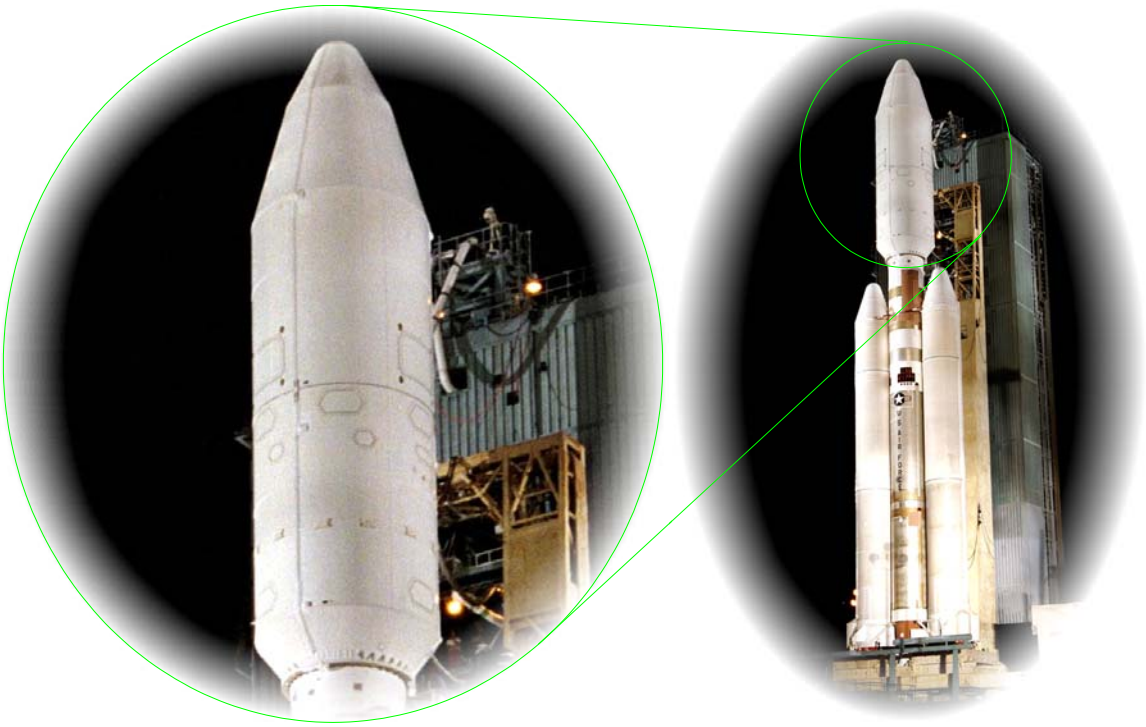

Figure 1.1. Payload fairing carrying the Cassini spacecraft on a Titan IVB/Centaur rocket (Wessen, 2005).

The high SPL can sometimes cause debilitating damage to a payload before deployment into space. Reports have indicated that anywhere from 40 to 60 percent of first-day satellite failures are from excessive vibration and SPL experienced by the payload during launch (Howard *et al*., 2005, Kemp and Clark, 2003). These failures require satellite designers to make their designs more robust, which usually adds a significant amount of weight to the design and offsets the advantages gained by using lighter weight composite fairings. Another issue of importance in satellite design is the use of light-weight components, such as thin films, membranes, and optics. These components are especially susceptible to low-frequency excitation (Kemp and Clark, 2003) and designing the components more robustly may cause compromised functionality of the components.

Currently, the SPL in payload fairings is reduced with passive devices such as Helmholtz resonators and acoustic blankets. Acoustic blankets work well at frequencies in which the blanket is thicker than a quarter of the length of the sound wave (Lane *et al*., 2006). Helmholtz resonators are efficient at passively damping lower acoustic modes, but are usually effective at one particular frequency (Estève and Johnson, 2005, Estève,

2004, Kinsler *et al*., 2000 pp 284-286). Therefore, additional resonators would be required for each low frequency mode to reduce the SPL over multiple modes, adding additional weight and taking up fairing space. Some active controllers (Clark and Gibbs, 1999, Farinholt, 2001, Lane *et al*., 2003, Lane *et al*., 2000) have been researched to introduce damping into the fairing system. These systems are usually designed assuming a particular enclosure where the interior acoustic characteristics are constant and unchanging.

1.2 Current Technology and Literature Review

Over the last 10 years several researchers have demonstrated noise control capabilities in payload fairings. Studies have used passive and active devices in an attempt to reduce overall weight and SPL. Continued research in passive devices has shown additional improvement in SPL reductions. Hybrid passive devices, where the passive system is used in parallel with an active system or the passive system is controlled in some form for setting the passive control properties, have also been studied. Research, the majority of which is associated with loud speakers, has shown that purely active devices have the capability to reduce low frequency SPL. This section will look at different passive and active devices and the current research associated with these devices for SPL reduction in launch vehicle payload fairings.

To familiarize the reader with acoustic enclosures and the internal properties of acoustic enclosures, Figure 1.2 shows the frequency response function (FRF) of the pressure measured in a reverberant room compared to an anechoic environment. A broadband disturbance source is placed in one corner of the room and the pressure measurement is obtained from another corner (Kinsler *et al*., 2000, p 354). The measured pressure comes from sound waves that travel directly from the disturbance source and from sound waves that are reflected from the boundaries of the enclosure. Once the enclosure has reached a steady state condition, the sound waves from the disturbance and the reflections will result in a standing wave pattern within the enclosure. The standing wave amplitude will be a function of the geometry of the enclosure and the acoustic wavelength. Standing waves at certain frequencies will have large amplitudes because

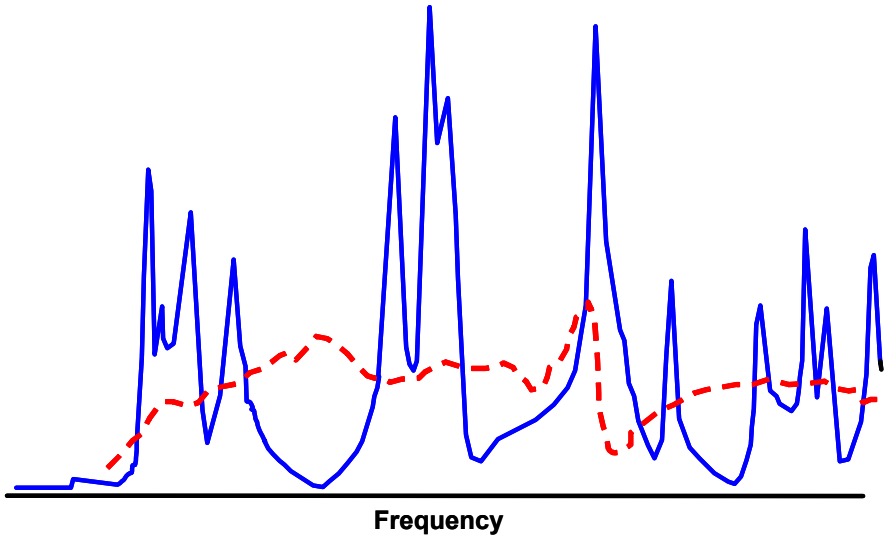

Figure 1.2. Experimental FRF of a reverberant room (solid blue line) and an anechoic environment (dashed red line) with the same disturbance source.

the reflected waves will be in-phase with the disturbance when the standing waves are formed and therefore increase the disturbance amplitude at that particular frequency. This increase is seen in Figure 1.2 for the reverberant room where pressure peaks are present at certain frequencies. An anechoic environment has little to no reflective pressure waves and therefore does not exhibit pressure peaks like a reverberant room.

Acoustic enclosures with highly reflective boundary conditions follow the characteristics of the reverberant room with pressure peaks at certain frequencies. These pressure peaks are called the acoustic modes of the enclosure and the frequencies associated with these modes are called the resonance frequencies. The sharpness of the pressure peak due to acoustic resonance is determined by the damping associated with the resonance frequency. The damping is dependent on the absorption of acoustic energy at the boundary of the enclosure which reduces the amplitude of the reflected pressure waves. For an anechoic room, the boundary absorbs almost all of the acoustic energy and the amplitude of the reflected pressure wave is almost zero. Therefore the damping in the acoustic modes is extremely high as seen in FRF of Figure 1.2 for the anechoic room. A reverberant room reflects the pressure wave with little energy absorption at the boundary and the acoustic modes' amplitudes are only limited by the energy absorbing properties of the air. The energy absorbing properties of air are very small and therefore the damping for enclosures without boundary absorbing properties is very low. Energy absorption designs attempt to reduce or eliminate the amplitude of the reflected acoustic

pressure waves. Reducing or eliminating these reflections effectively adds damping and absorbs acoustic energy which will cause the peak pressure at the acoustic resonances of the FRF to be reduced and reduce the overall SPL within the system.

Acoustic blankets are one of the devices included in a payload fairing that adds damping to the enclosure. Blankets add damping to the system by absorbing acoustic energy and dissipating the energy throughout the structure. Acoustic blankets are most effective at high frequencies because the ability of the blanket to absorb energy is dependent on the thickness being longer than a quarter of the acoustic wavelength. The wavelength is proportional to the speed of sound and inversely proportional to the frequency (Bies and Colin, 2003). Increasing the blanket thickness reduces the usable volume within a fairing and adds additional weight. The blanket thickness is determined by a tradeoff between SPL reduction and the added weight and volume constraints. Current research with acoustic blankets have investigated sound absorption properties as the thickness and density of the absorbing material is varied (Hughes *et al*., 1999). Hughes found that blankets achieving a 3 dB reduction in the 200 to 250 Hz frequency range weighed four times more than the baseline blanket. Kidner *et al*. (2006) suggested adding additional masses into the poro-elastic layers of the blanket at random locations. These additional masses were reported to act as resonant systems and increase the structural impedance and therefore reduce the structural vibration and transmission of energy into the fairing in the form of sound. The disadvantages of these approaches are that they add mass in the fairing and therefore increase the launch cost.

Multiple researchers have investigated the use of additional masses on the fairing walls and within the structure (Estève and Johnson, 2005, Estève, 2004, Howard *et al*., 2005, Lane *et al*., 2006). The researchers use different names for the devices, but they all function similarly to the additional mass added to the acoustic blankets, as reported by Kidner *et al*. These devices act as passive vibration absorbers in the fairing to reduce the transmission of energy into the acoustical domain.

Lane *et al*. (2003) also suggested using active means to reduce vibration and the transmission of energy into the interior of a fairing. The use of a single-crystal piezoelectric was suggested as the controlled actuator for vibration reduction and Lane *et al*. reported a potential 10 dB reduction over the 0 to 300 Hz frequency range in

simulations. Lane *et al*. also reported that model uncertainty and sensor noise reduced the actual SPL reduction to 3 dB. Lane *et al*. (2006) reported achieving 5 dB reduction over the 70 to 200 Hz frequency range using distributed active vibration absorbers in a composite cylinder that was about 2.8 meters long with a 1.2 meter radius.

Helmholtz resonators are passive absorbers that have been studied since the end of the 19th century (Rayleigh, 1877) and continued in the 21st century (Estève, 2004, Sacarcelik, 2004). Resonators are usually designed to add damping to one particular mode and if multiple modes are present, multiple resonators are needed. Lane *et al*. (2005) suggested using the hollow chambers within the walls of the composite fairing as resonators. This design would add no additional mass and occupy no additional volume within the fairing since the structure of the fairing holds the resonators. Tests showed that a 10 to 12 dB reduction was achieved over the bandwidth from 0 to 400 Hz. One issue with resonators is the fact that they are designed for damping a particular frequency, and a shift in the acoustic characteristics could detune the resonators causing less energy absorption. A promising solution to this problem was presented by Estève (2004) in the form of an adaptive resonator. The open area of the resonator is adjustable, therefore making the absorption frequency of the resonator adjustable. Any shifts in the acoustic characteristics could be accommodated by this adaptive design. Additional research using the adaptive resonator with the internal fairing chamber for noise absorption is one of the more promising solutions for this application.

Secondary acoustic sources have been studied as active absorbers for acoustic applications for more than 70 years. Lueg (1936) submitted a patent in 1934 using a feed forward control technique in a long enclosure for noise cancellation. A microphone measured the disturbance signal traveling in the enclosure and produced an out of phase signal with a speaker further down the enclosure to cancel out the signal. Within the last decade, research has continued on the work performed by Lueg. Clark *et al*. (1995, 1996, and 1999) has performed modeling and testing of acoustic enclosures using feedback control with speakers as the control actuators for absorbing acoustic energy. Clark *et al*. (1999) reported 10 dB local attenuation over the bandwidth from 100 to 400 Hz in a jet fuselage. Lane *et al*. (2000) reported a 6 dB global reduction for an aircraft fuselage implementing control on 5 modes below 150 Hz. Green (2000) reported 4 dB RMS

reduction in a plastic cylindrical duct over the bandwidth from 0 to 200 Hz using a specially designed lightweight speaker where the speaker driver was made from piezoceramic actuators attached to cantilever beams. The actuator was driven near the beams resonance frequency to produce sufficient stroke for driving the speaker to absorb acoustic energy. The speaker was effective at absorbing noise near the resonance of the beam, but Green reported that for multiple modal control, an additional actuator would be needed for each mode. Farinholt (2001) used PPF control on a Lexan payload fairing that was 2.6 meters tall with the largest diameter of 0.75 meters. Farinholt reported an average 4.2 dB reduction averaged over 6 microphones over the 50 to 250 Hz frequency range. Kemp and Clark (2003) suggested actively tuning a loud speaker in the nose of a fairing to globally absorb energy at a targeted modal frequency. Kemp and Clark reported a 4.9 dB peak reduction at the mode located at 69 Hz from 16 microphone measurements within a fairing. Sacarcelik (2004) used loud speakers in a composite test cylinder that was 2.8 meter long with a diameter of 2.46 meters. Using feed forward control, Sacarcelik reported a 2.2 dB global reduction in the cylinder.

1.3 Interior Acoustic Changes

Fairings and payloads come in numerous shapes and sizes, and are used with different launch conditions. The majority of active control studies for this application use non-changing systems for designing the controller. Geometric and launch variables could detune an active system and potentially cause instability. Figure 1.3 shows schematics of two different payload fairings showing the extremity of sizes available where the payload shown in each fairing is of similar size (1 meter diameter by 2 meters high) (Courtesy of NASA). Any active controller would need to be retuned for application in different fairings because of different interior acoustic characteristics caused by fairing and payload sizes. An adaptive controller could tune the controller for the initial system and keep the controller tuned for any interior acoustic characteristics changes caused during the launch.

The literature abounds with information on adaptive control designs and laws. Many books explaining the basic theory and schemes of adaptive control have been

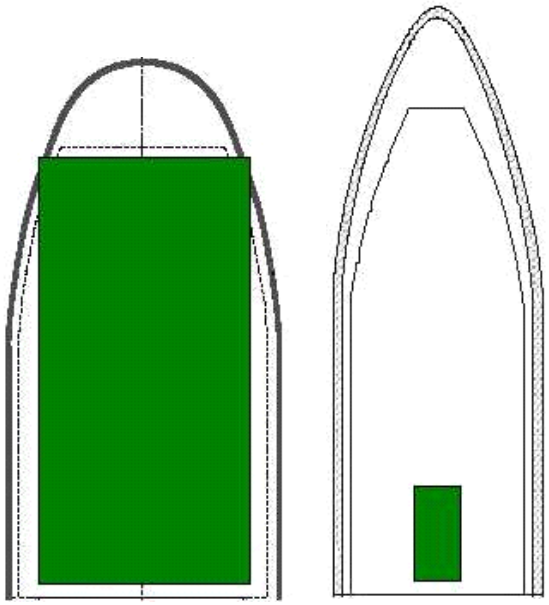

Figure 1.3. Schematics of a payload fairing for the Pegasus launch vehicle on the left and a payload fairing for the Atlas V launch vehicle on the right, each with a similar sized payload to show potential fairing size differences (Herring, 2006).

written including those by Astrom and Wittenmark (1995), Goodwin and Sin (1984), Krstic *et al*. (1995), Narendra and Annaswamy (1989), and Sastry and Bodson (1989). Adaptive control is needed when "… the plant is initially unknown, or only partially known, or it may be slowly varying" (Anderson, 2005). Figure 1.4 shows an example of an adaptive feedback block diagram similar to the diagram used by Astrom and Wittenmark (1995, p 2) to explain adaptive feedback. The additional parameter adjustment block contains some algorithm that can make changes to the controller depending on the input, the control signal, the output of the system, or some combination of the input, control signal, and output of the system.

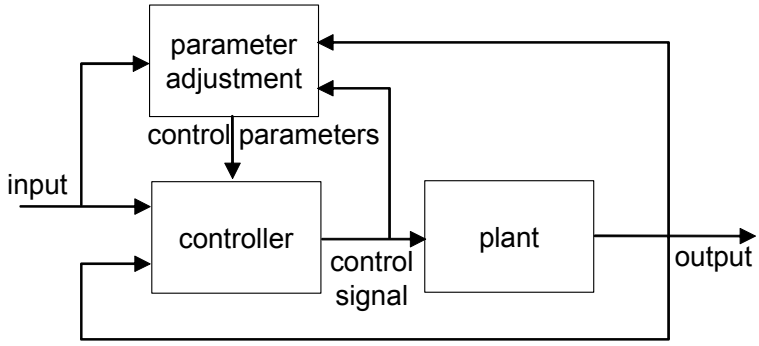

Figure 1.4. Block diagram of an adaptive feedback controller.

Few researchers have implemented adaptive control for sound absorption in payload fairings. Estève (2004) presented an adaptive resonator that could be used in a passive adaptive control scheme and McEver *et al*. (2003) used the adaptive control techniques of *Q*-parameterization and Generalized Predictive Control using an error microphone and control speaker. McEver *et al*. used the same composite test cylinder used by Sacarcelik and reported a reduction in the first acoustic mode of 6 dB globally. This active control research used a system with non-changing parameters for implementing control. With fairing and payload size variations, potential launch variations, and the need to reduce the SPL at low frequency, an adaptive controller is ideal for this application. An adaptive controller could adapt to the aforementioned variations and reduce the SPL at low frequency for this application. Therefore this research focuses on adaptive control of SPL for interior acoustic enclosures.

1.4 Contribution

Positive position feedback (PPF) is chosen for actively control of absorbing acoustic energy. PPF control has an inherent low frequency spillover when multiple modes are controlled that can increase the overall SPL of the system as explained in the literature. This work extends previous PPF control work by showing how bandpass filters, comprised of a sixth order high-pass Butterworth filter and a second order low-pass Butterworth filter, used in conjunction with the PPF filters can diminish the low frequency spillover effect. An algorithm is also presented for setting the parameters of the combined PPF and Butterworth filters where the algorithm is designed from simulations and testing of the duct and. This algorithm is then used to design an adaptive controller. The adaptive controller uses a fast fourier transform (FFT) of buffered data to identify the modes of the system in real time and set the filters for energy absorption. This adaptive controller is able to accommodate a 20 percent change in the frequencies of the acoustic modes of a system and maintain stability and reduce the SPL of the system.

1.5 Thesis Overview

The control work performed by Farinholt (2001) is continued in this research in terms of using positive position feedback (PPF) for acoustic energy absorption. Testing is performed within a cylindrical duct enclosure using non-adaptive feedback PPF control and the modified PPF controller using high and low-pass Butterworth filters to reduce controller spillover. An algorithm is presented for setting the PPF and Butterworth filters. The non-adaptive feedback control with PPF control using high and low-pass Butterworth filters is also used for control on a full sized model of a payload fairing. The presented algorithm is then used to design an adaptive controller which is tested on the cylindrical duct as the boundary conditions are changed.

Impedance modeling of the duct is presented in Chapter 2 with internal pressure estimates compared to the measured internal pressure. PPF control is introduced and simulated control results for the collocated position within the cylindrical duct are presented. Absorption coefficient calculations used for the pressure estimates are shown in Appendix A. Additional internal pressure estimates compared to measured internal pressures and additional simulated control results are shown in Appendix B. Measured control results using non-adaptive control with the feedback compensator designed using PPF and PPF in conjunction with high and low-pass Butterworth filters are presented in Chapter 3 for the duct and the fairing model. Additional non-adaptive control results for the duct and the fairing are shown in Appendix C. Adaptive control definitions are presented in Chapter 4 as well as the designed adaptive controller used for the duct. Adaptive control results where the duct length is reduced by 12 inches in real time will be shown with inch incremental results shown in Appendix D. Appendix E contains the code used for obtaining the impedance model, simulating the control, setting the non-adaptive controller, and setting and implementing the adaptive controller.

Chapter 2

Analytical Models

2.1 Introduction

The main focus of this research is to design an adaptive feedback controller to reduce the sound pressure level (SPL) during launch in small to medium sized payload fairings. Analytical modeling of a payload fairing or a similar structure has been performed by other researchers (Estève, 2004; Farinholt, 2001; Kemp and Clark, 2003; Lane *et al*., 2003; Li and Vipperman, 2005) and while not the focus of this work is being used in the developmental state. A system model can provide useful insights and understanding of the acoustic environment and allow tests of control concepts through simulation before demonstrating them in hardware. For these reasons a representative system is modeled in order to understand the basics of an acoustic enclosure, the basics of the controller that is eventually to be used with the payload and fairing, and how the SPL in the representative system is affected when control is added to that system. The system model consists of a cylindrical acoustic duct enclosure with a rigid end cap covering one end and a speaker covering the other end. This chapter contains an analytical impedance model of this cylindrical duct enclosure, the basic definition of the positive position feedback (PPF) controller, and an analytical control study of the closed-loop system where control is simulated on the model of the enclosure.

2.2 Analytical Model of a Cylindrical Duct Enclosure

The system modeled is a plastic cylindrical duct with a speaker attached to one end and a sheet metal plate, attached to plywood, placed on the other end. Analytical models of this cylindrical system, which assumes the enclosure to be rigid and smooth with a rigid end cap, have been studied in detail because of the simplicity of the geometry and the fact that plane waves can be assumed in the system at low frequency (Kinsler *et al*., 2000, p 272). Figure 2.1 shows a schematic of this system, similar to Kinsler *et al*. (2000, p 280), where *m* is the mass of the speaker, *s* is the stiffness of the speaker, and *R* is the damping in the speaker. This schematic assumes that the speaker can be modeled as a spring/mass/damper. The frequency range of interest for the model is limited to the range from 0 to 500 Hz to ensure plane waves in the system.

The acoustic behavior of the enclosure is dependent on the length, the cross sectional area, the dynamics of the driver (the speaker in this case), the dynamics of the end cap (assumed to be rigid), and any damping that is associated with the structure of the enclosure, the properties of air, and additional damping (added by the boundaries) that is not included in the dynamics of the driver. The exact properties used in this model are listed in Table 2.1 and are taken from a speaker properties data sheet (RadioShack, 1995); physical measurements; and approximations for the properties of air (Sengiel, 2005) as determined from the elevation of Blacksburg, Virginia and from the humidity, pressure, and temperature of the air found using a Lacrosse (model #WS8035U) weather station.

2.2.1 Impedance Model of the Cylindrical Duct Enclosure

The impedance model of the duct was derived by Kinsler *et al*. (2000, pp 272-283) and is repeated here for completeness. The plane waves in the enclosure produce a

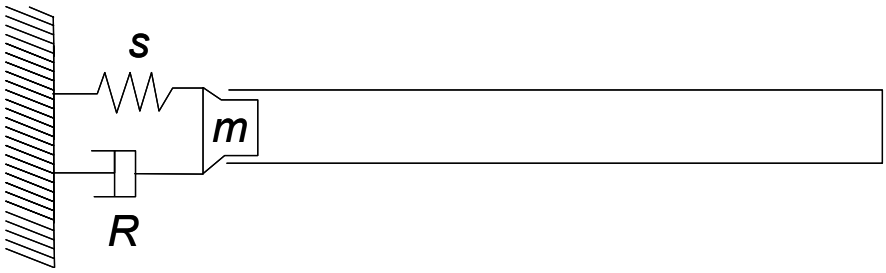

Figure 2.1. Schematic of the driver-cylindrical duct system where *R*, *s*, and *m* are the damping, stiffness, and mass of the driver respectively.

Table 2.1. Constants from duct measurements, the speaker data sheet, and air properties.

constant	symbol	value	units
duct radius	a	0.1016	m
duct cross sectional area	S	0.0324	m^2
duct length	L	1.8463	m
speaker dynamic mass	m_s	18.38	g
speaker mechanical compliance	s^{-1}	1174.63	μm/N
speaker electrical resistance	R_e	6.6	ohms
speaker electrical inductance	L_e	0.93	mH
speaker damping (assumed critical damping)	R	7.91	Ns/m
speaker magnetic flux density and wire length	Bl	6.77	T-m
air density	ρ	1.1877	kg/m^3
air speed of sound	c	345.25	m/s

produce a pressure (***p***) that is modeled with the following equation,

$$\mathbf{p}(x,t) = \mathbf{A}e^{j[\omega t + k(L-x)]} + \mathbf{B}e^{j[\omega t - k(L-x)]} \tag{2.1}$$

where ω is the frequency in rad/s, k is the wave number defined as ω/c where c is the speed of sound, L is the length of the duct, x is the location of interest along the duct, t is the time, and ***A*** and ***B*** are constants to be determined from the boundary conditions. Variables in bold text in this model are values that may be complex. The particle speed (***u***) of the air from the plane wave is defined as

$$\mathbf{u}(x,t) = -\frac{1}{\rho}\int\left(\frac{\partial \mathbf{p}}{\partial x}\right)dt\,. \tag{2.2}$$

Inserting Equation 2.1 into Equation 2.2, the particle speed of the air is

$$\mathbf{u}(x,t) = \frac{1}{\rho c}\left(\mathbf{A}e^{j[\omega t + k(L-x)]} - \mathbf{B}e^{j[\omega t - k(L-x)]}\right). \tag{2.3}$$

The general definition of the impedance of a point of a system, or a plane in this case because of the plane wave assumption, is defined as the force at that point divided by the velocity at that point and is

$$\mathbf{Z}(\omega) = \frac{\mathbf{F}(\omega)}{\mathbf{u}(\omega)} \tag{2.4}$$

where the force and the particle velocity are assumed to be at steady state. This assumption makes the impedance a function of frequency.

The radiation impedance is defined as $\boldsymbol{Z_a}$ where the acoustic force is the pressure, from Equation 2.1, multiplied by the cross sectional area, S, and the particle velocity

comes from Equation 2.3. The radiation impedance is

$$\mathbf{Z}_a(\omega) = \rho c S \frac{\mathbf{A}e^{j[\omega t + k(L-x)]} + \mathbf{B}e^{j[\omega t - k(L-x)]}}{\mathbf{A}e^{j[\omega t + k(L-x)]} - \mathbf{B}e^{j[\omega t - k(L-x)]}} \tag{2.5}$$

where the time variable will cancel out leaving the impedance as a function of the wave number which is a function of frequency. Since the end cap is assumed to be rigid, the mechanical impedance of the end cap is infinity. The radiation impedance at the end cap will match the mechanical impedance of the end cap causing the constants ***A*** and ***B*** of Equation 2.5 to be equal. Using this equality, the radiation impedance at the speaker end ($x = 0$) is found to be

$$\mathbf{Z}_a(\omega) = \rho c S \frac{\mathbf{A}e^{jkL} + \mathbf{A}e^{-jkL}}{\mathbf{A}e^{jkL} - \mathbf{A}e^{-jkL}}. \tag{2.6}$$

Using Euler's identities and the definition of the wave number, Equation 2.6 reduces to

$$\mathbf{Z}_a(\omega) = -j\rho c S \cot {\omega L}/{c}. \tag{2.7}$$

Kinsler *et al*. states that resonance in the duct enclosure occurs when the reactance, or imaginary part, of this impedance is zero.

2.2.2 Mechanical/Electrical Impedance Model of the Speaker

As previously stated, the speaker mounted on the enclosure can be mechanically modeled as a mass/spring/damper as shown in Figure 2.1 and electrically modeled as a resistance and inductance (RL) electric circuit. An RL circuit equation of motion is

$$V = Ri + L\frac{di}{dt} \tag{2.8}$$

where the electrical impedance, found according to Ohm's law, is defined as the voltage divided by the current. Therefore, the electrical impedance ($\boldsymbol{Z_e}$) is

$$\mathbf{Z}_e(\omega) = R_e + j\omega L_e. \tag{2.9}$$

The mechanical equation of motion for the speaker is

$$m_s \frac{d^2x}{dt^2} = -R\frac{dx}{dt} - sx + F \tag{2.10}$$

where F is the force applied to the speaker from the electrical circuit (Kinsler *et al*., 2000, p.280). Using Equation 2.10 the mechanical impedance ($\boldsymbol{Z_m}$) can be found to be

$$\mathbf{Z}_m(\omega) = R + j(\omega m - {s}/{\omega}). \tag{2.11}$$

Eargle (2003, p 7) suggests adding an additional air mass to the mass of the speaker in order to more closely match measured data. This air mass value is found from the geometry of the speaker and air properties and is

$$m_{air} = 8\frac{a^3\rho}{c}. \tag{2.12}$$

2.2.3 Combined Impedance Model and Pressure Estimates

The combined electromechanical impedance model, as shown in Figure 2.2, is similar to one used by Leo and Limpert (2000) and explained in detail by Beranek (1996, pp 47-90). This combined impedance model can be simplified to find the overall impedance (***Z***) of the system as

$$\mathbf{Z}(\omega) = \mathbf{Z}_e(\omega) + \frac{\mathbf{Z}_m(\omega) + S^2\mathbf{Z}_a(\omega)}{(Bl)^2}, \tag{2.13}$$

where B is the magnetic flux density of the speaker and l is the length of the wire in the coil of the speaker. Ohm's law can be applied to find the current given any known input voltage into the speaker. The current can be used to calculate an approximate force into the speaker because the force is defined as (Beranek, 1996, p 70)

$$\mathbf{F}(\omega) = Bl\mathbf{i}(\omega). \tag{2.14}$$

The pressure at any point along the length of the cylindrical duct enclosure is represented by the following equation,

$$\mathbf{p}(x,\omega) = \mathbf{p}(0,\omega)\frac{\cos[k(L-x)]}{\cos kL} \tag{2.15}$$

where the pressure at position zero is defined as

$$\mathbf{p}(0,\omega) = \frac{\mathbf{F}\mathbf{Z}_a(\omega)}{S(\mathbf{Z}_a(\omega) + \mathbf{Z}_m(\omega))}, \tag{2.16}$$

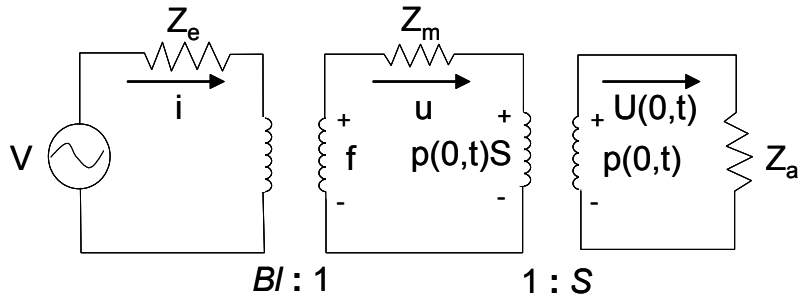

Figure 2.2. Combined electromechanical impedance model of a duct with a speaker attached to one end.

where the force, ***F***, is found from Equations 2.13 and 2.14 (Kinsler *et al*., 2000, p 281) when assuming steady state conditions. Now the pressure at any point within the enclosure can be modeled given the location of interest along the length of the duct and the frequency of the applied voltage. Figure 2.3 shows a frequency response function (FRF) (at x ≈ 0.04 m) and the approximate phase of the system with a simulated 0.05 volt input over a frequency range from 0 to 500 Hz with a frequency step of 0.5 Hz. The ordinate of the left plot is the estimated SPL in dB (reference 20e-6 Pa), the ordinate of the right plot is the phase in degrees, and the abscissa of both plots is the frequency in Hz. At this point in the model, the only damping in the system is the damping associated with the speaker, which adds damping to the lower frequency modes of the system, as seen in the magnitude plot, and has less effect on the damping of higher modes. The phase does not follow the pole/zero relationship seen in the magnitude plot because of the numerical precision of the computation caused by the low damping values of the zero frequencies above 150 Hz in the model. Adding additional damping to the model, as will be seen later in this chapter, fixes this phase irregularity.

2.2.4 Acoustic Energy Losses (Damping)

Additional damping is added to the system from the acoustic energy losses. Kinsler *et al*. (2000, pp 210-241) suggests adding an additional imaginary term to the wave number called the absorption coefficient and the wave number becomes

$$\mathbf{k} = k - j\alpha \,. \tag{2.17}$$

k is the complex wave number and α is the absorption coefficient which is a function of

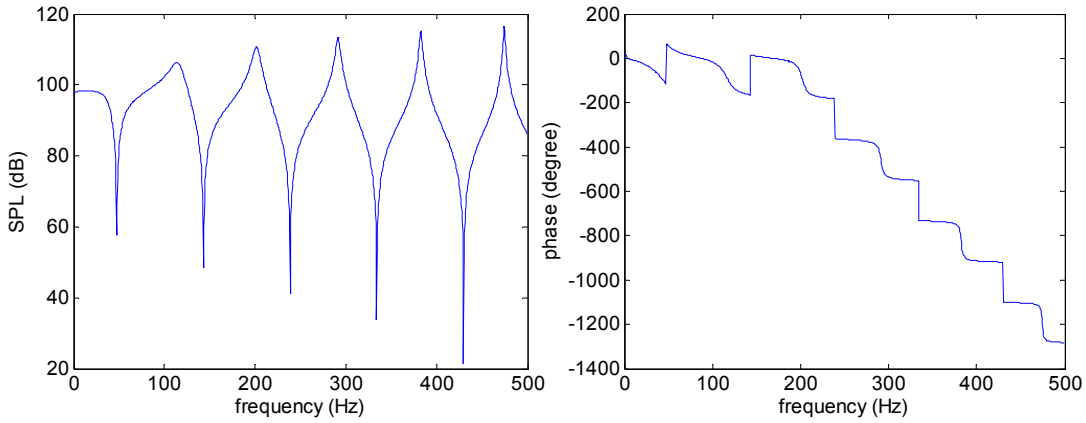

Figure 2.3. Analytical frequency response function of the enclosure simulated about 0.04 m away from the speaker.

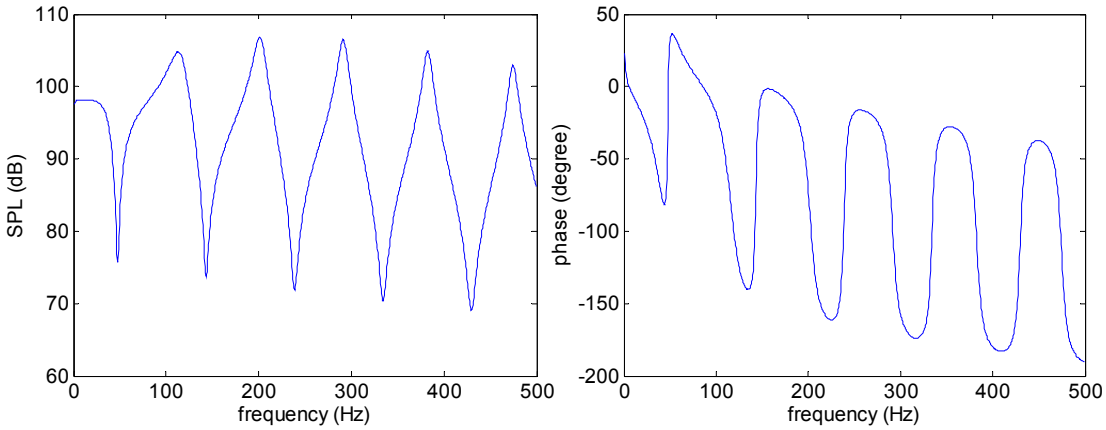

Figure 2.4. Analytical frequency response function of the enclosure simulated about 0.04 m away from the speaker with the absorption coefficient included in the model.

frequency and air properties. A more detailed discussion and literature review of the definition of the absorption coefficient is found in Appendix A. Equation 2.17 is used in the previous model derivation to replace the non-complex wave number to account for additional damping within the enclosure. Figure 2.4 shows the same results of the analytical model as seen in Figure 2.3, but uses the complex wave number in the equations of the model. The figure shows how additional damping is added to the higher modes of the system and the phase now follows the pole/zero relationship without the numerical precision errors.

2.3 Analytical Duct Model and Data Comparison

The modeling results discussed in the previous section are correlated to experiments on the acoustic enclosure shown in Figure 2.5. An 8 ohm, 8 inch Radio Shack speaker (RadioShack, 1995) is attached to one end of the cylindrical duct and a piece of ¾ inch plywood with a sheet metal plate attached is inserted into the other end. Pressure measurements are made in the duct with three ¼-inch PCB microphones (model 130D21); using a Dytran signal conditioner (model 4103C) for conditioning the microphone signals. One PCB microphone measurement location is about 2 inches from the speaker (sensitivity of 42.0 mV/Pa) and considered the collocated measurement location (P_1), the second PCB microphone measurement location (P_2) is about 38 inches from the speaker (sensitivity of 44.7 mV/Pa), and the last PCB microphone measurement location (P_3) is about ¾-inch from the rigid end cap (sensitivity of 39.8 mV/Pa). The

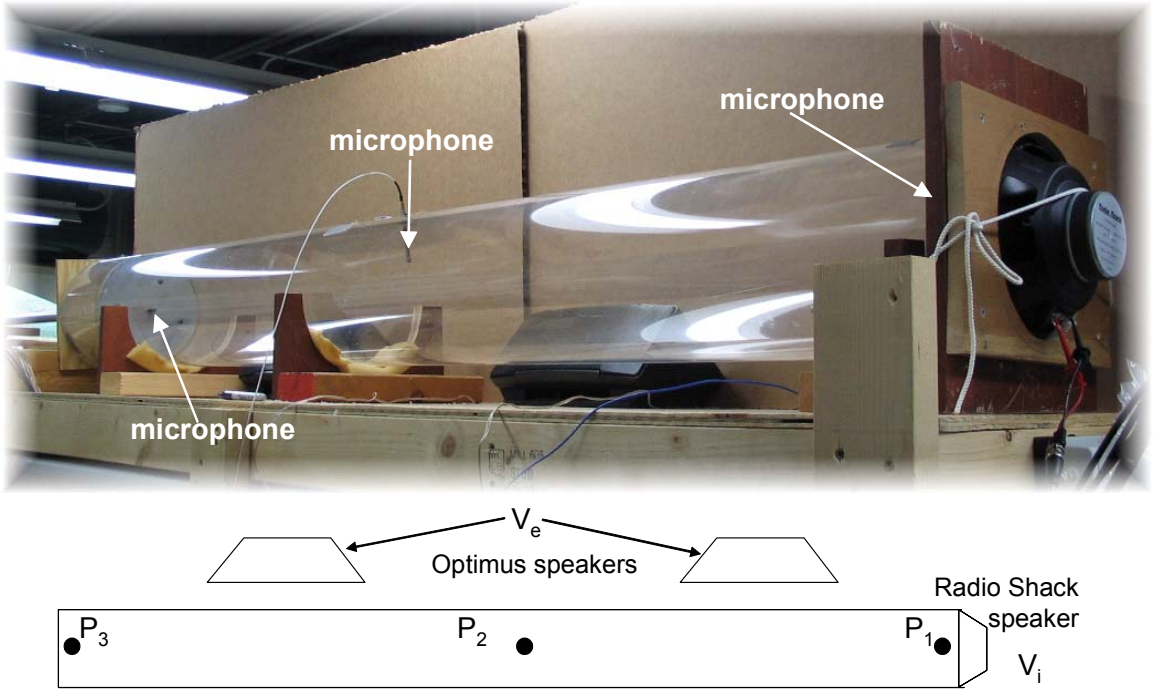

Figure 2.5. Photograph and schematic of the cylindrical duct test article with the pressure measurement locations labeled in the photograph and schematic and the disturbance voltages labeled in the schematic.

Radio Shack speaker, considered the control speaker, is attached to a ¾-inch board with a circular cut made to slip over the duct as seen on the right side of the photograph in the figure above. The voltage of disturbance signals sent to this speaker is labeled as V_i in the system schematic. The duct is supported at three points by ¾-inch boards with half circles cut out of them and layered with foam. Two Optimus speaker systems (Cat No: 12-1713), considered the external disturbance speaker, are placed along the side of the enclosure and are used to excite the system where the voltage of this external disturbance is labeled V_e in the system schematic. Testing is performed with broadband disturbance signals sent to both the Radio Shack speaker and the Optimus speaker systems as will be discussed. Further details of the end cap design are found in Chapter 4.

A Spectral Dynamics Siglab unit (model 20-42) is used to supply a random voltage (0.05 RMS) from 0 to 1000 Hz into the system and to measure the pressure at the microphone locations. A Hanning window is used to analyze the measured data and five data sets are averaged with 4096 data points captured for each set in calculating the autospectrum and transfer function of each microphone location. The Siglab random voltage is sent to a Realistic audio amplifier (model 32-2033A) to drive the control and

external disturbance speakers (depending on the experiment). Figure 2.6 shows the transfer function of the 0.05 RMS random 0 to 1000 Hz input to the amplifier over the output measured from the amplifier. This transfer function shows the dynamics of the amplifier where the magnitude of the amplifier has a rapid roll-up until 20 Hz and then continues to increase slowly until there is a flat response above 100 Hz. The phase drops off quickly at low frequency but steadies to a 0.10 degree/Hz drop after 200 Hz.

Figure 2.7 shows the collocated measured transfer function (P_1/V_i) in blue with the analytical model results (P_1/V_i) in green overlaid on the measured results. The ordinate of the magnitude plot is the voltage of the microphone measurement over the voltage of the Siglab voltage input. The model units are changed to correspond to the measured units by multiplying the sensitivities of each microphone by the model's estimated pressure level to obtain P_1 in units of volts. This change causes the model

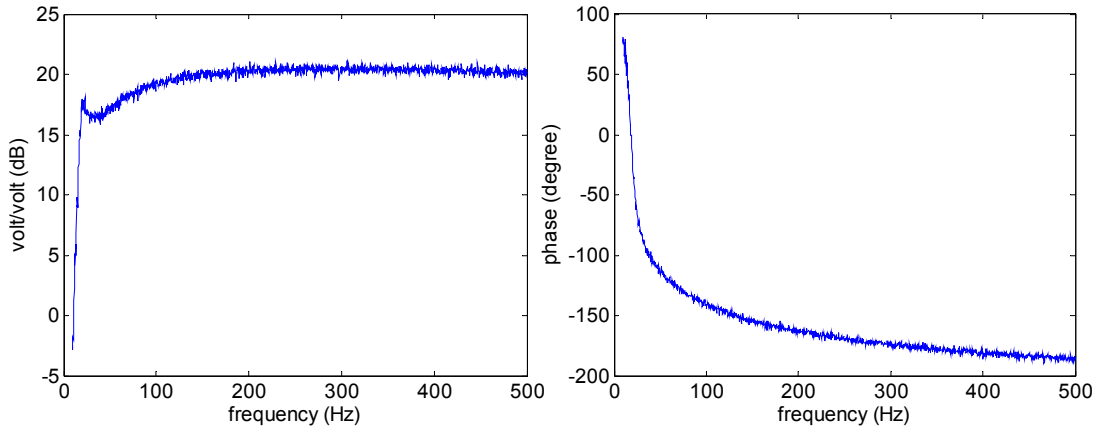

Figure 2.6. Frequency response function of the amplifier.

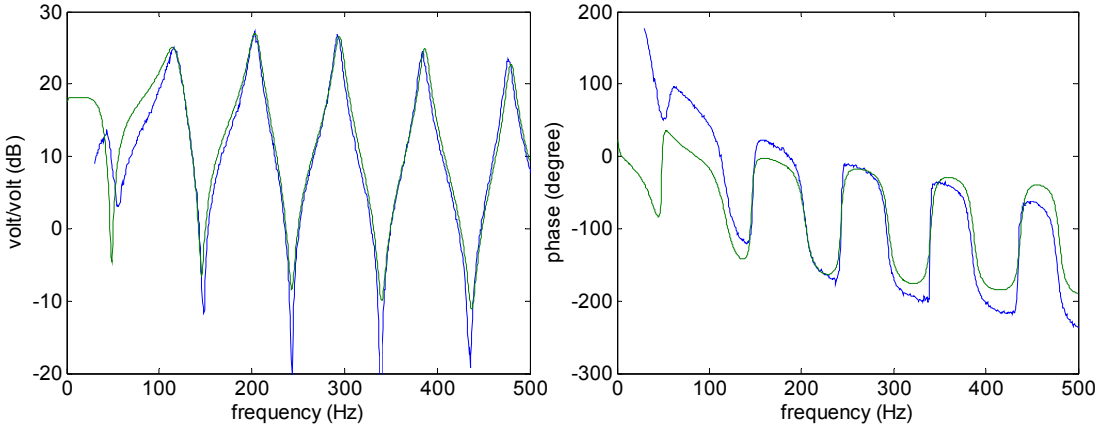

Figure 2.7. Measured collocated transfer function (blue) of the enclosure with the analytical model (green) overlaid on top.

simulations to be in the same units as the measured data which are microphone voltage over input disturbance voltage.

The major differences between the analytical results and the measured results are at low frequency and are caused by the un-modeled amplifier dynamics. Adding magnitude roll-up at low frequencies with an increase in the low frequency phase will allow the model to fit the measured data more accurately and will effectively be modeling the amplifier dynamics. To accommodate for the difference between the model and the measured data, a 1st order high pass Butterworth filter is used. The filter cutoff frequency is set at 300 rad/s and the transfer function of the filter is set to,

$$F_{1\_butter}(s) = \frac{s}{s+300}. \tag{2.18}$$

This filter rolls-up at 20 dB per decade at low frequency and levels out into a flat response of 0 dB above 50 Hz. The filter adds 90 degrees of phase at 0 Hz because of the zero added to the system. Figure 2.8 shows the collocated measured and analytical model transfer function (P_1/V_i) with the addition of the Butterworth filter. The figure shows a closer fit between the model and data for predicting the locations and magnitudes of the poles and zeros of the measured data. The largest discrepancies are still at low frequencies for the magnitude and the phase. The model also does not include the 0.1 degree/Hz phase drop above 200 Hz. Additional plots of the measured data overlaid with the analytical model for the P_2/V_i and P_3/V_i transfer functions can be seen in Appendix B. For the model to be improved and more closely match the measured data, a higher order filter, that more closely matches the amplifier dynamics as seen in Figure 2.6, is needed.

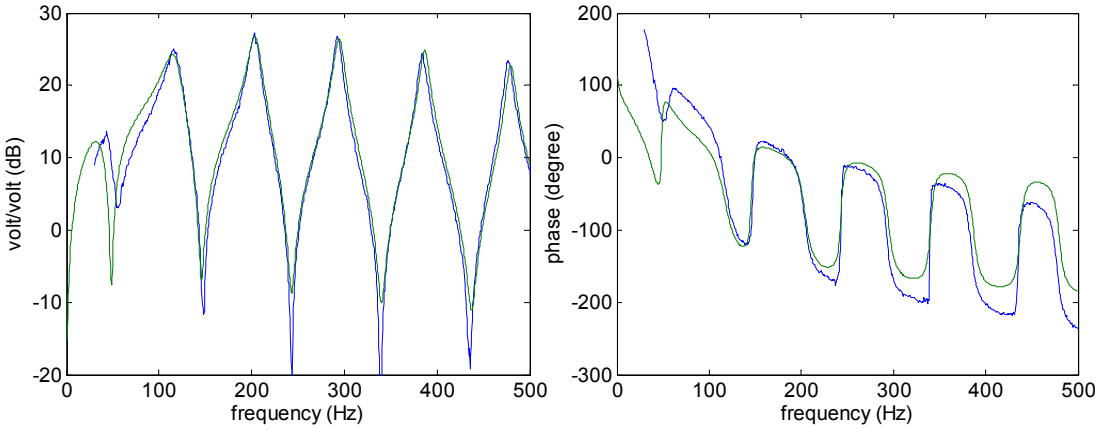

Figure 2.8. Measured collocated transfer function (blue) of the enclosure with the analytical model (green) and high pass filter overlaid on top.

Table 2.2 shows the pole frequencies, damping ratios, and zero frequencies for the model and Table 2.3 shows the pole frequencies, damping ratios, and zero frequencies for the measured transfer functions. A Matlab function is created, which can be seen in Appendix E, to analyze the model and the data, and is used to find the pole frequencies, damping ratios, and zero frequencies of the measured and modeled transfer functions. The pole frequencies are found by finding the peak values of each mode in the transfer function. The damping ratios (ζ) are then found according to the following equation (Inman, 2001, p 511),

$$\zeta = \frac{\omega_b - \omega_a}{\omega}, \tag{2.19}$$

where ω is the frequency of the pole, ω_b is a higher frequency value where the transfer

Table 2.2. Modeled pole frequencies, damping ratios, and zero frequencies for the first six modes of the model.

P_1 Location						
poles (Hz)	31.7	114.7	203.2	294.2	386.7	479.7
damping ratio	0.35	0.09	0.03	0.02	0.01	0.01
zeros (Hz)	48.2	144.7	241.2	337.7	434.2	-
P_2 Location						
poles (Hz)	42.2	122.2	203.7	291.2	386.7	478.7
damping ratio	0.29	0.50	0.03	0.32	0.01	0.01
zeros (Hz)	100.7	-	-	303.2	-	-
P_3 Location						
poles (Hz)	44.7	116.7	203.7	294.2	386.7	479.7
damping ratio	0.36	0.08	0.03	0.02	0.01	0.01
zeros (Hz)	-	-	-	-	-	-

Table 2.3. Measured pole frequencies, damping ratios, and zero frequencies for the first six modes of the data.

P_1 Location						
poles (Hz)	43.8	115.6	203.1	292.5	383.8	476.9
damping ratio	0.15	0.06	0.02	0.01	0.01	0.01
zeros (Hz)	56.3	148.1	243.1	339.4	435.6	531.9
P_2 Location						
poles (Hz)	43.8	121.9	203.1	289.4	383.8	475.6
damping ratio	0.14	0.53	0.02	0.07	0.01	0.01
zeros (Hz)	108.1	-	-	300.6	-	-
P_3 Location						
poles (Hz)	46.3	115.6	203.1	292.5	383.8	476.9
damping ratio	0.17	0.06	0.02	0.01	0.01	0.01
zeros (Hz)	-	-	-	-	-	-

Table 2.4. The percent change in the pole and zero frequencies between the model and the measured data with the measured data as the reference.

P_1 Location						
poles	-27.6 %	-0.8 %	0.1 %	0.6 %	0.8 %	0.6 %
zeros	-14.4 %	-2.3 %	-0.8 %	-0.5 %	-0.3 %	-
P_2 Location						
poles	-3.7 %	5.7 %	0.3 %	0.6 %	0.8 %	0.7 %
zeros	-6.8 %	-	-	0.9 %	-	-
P_3 Location						
poles	-3.5 %	1.0 %	0.3 %	0.6 %	0.8 %	0.6 %

function's magnitude drops 3 dB lower than the magnitude of the pole, and ω_a is a lower frequency value where the transfer function's magnitude also drops 3 dB lower than the magnitude of the pole. The zeros are initially estimated by looking for the lowest value of the magnitude between the found pole frequencies and setting the zero frequency to the associated minimum magnitude frequency. The zeros are ultimately determined by the phase characteristics of the transfer function. The last zero for the P_1 measurement of the model is not reported because the frequency limitation of the model. No zeros are reported for the P_3 location and only two zeros are reported at the P_2 location. The discrepancy in the analytical pole frequency values of the first mode for the three different measurement locations is caused by the high-pass Butterworth filter modeling the amplifier dynamics. The actual peak value for the first mode is changed for the different measurement locations when the filter is included in the model.

Table 2.4 shows the percentage changes between the model and the measured data for each pole and zero frequency at each mode. Except for the first pole and zero frequency, the majority of the model is within 5 percent of the measured data and within one percent above the third mode and is considered an adequate fit for this research. The damping ratios are not included in the table below because the majority of the modes are lightly damped and very small shifts can cause large divergences when the data is analyzed in this manner.

2.4 Controller and Analytical Duct Control Studies

Positive position feedback (PPF) is the controller chosen for this research. PPF is a filter with second-order dynamics that receives the system measurement and returns a

positive control signal back to the control actuator. Fanson and Caughey (1990) describe PPF controllers by first defining a second order equation of the system as follows,

$$\ddot{\xi} + 2\zeta\omega\dot{\xi} + \omega^2\xi = g\omega^2\eta \tag{2.20}$$

where ξ is the modal coordinate of the system, ζ is the damping ratio of the system, ω is the natural frequency of the system, g is the controller gain, and η is the filter coordinate. A second-order equation is also used to define the filter as follows,

$$\ddot{\eta} + 2\zeta_f\omega_f\dot{\eta} + \omega_f^2\eta = \omega_f^2\xi \tag{2.21}$$

where ζ_f is the damping ratio of the filter and ω_f is the natural frequency of the filter. The positive position terminology comes from the fact that the positive position of the modal coordinate of the system, Equation 2.20, is positively sent to the filter, Equation 2.21, and the positive position of the filter, again Equation 2.21, is positively sent to the system or modal coordinate, Equation 2.20. The filter is described in greater detail by DeGuilio (2000), Fanson and Caughey (1990), Goh (1983), and McEver (1999).

The transfer function of the PPF filter (K), Equation 2.21, takes the form

$$K(s) = \frac{g\omega_f^2}{s^2 + 2\zeta_f\omega_f s + \omega_f^2} \tag{2.22}$$

where the variables are the same as described above. This equation shows that the filter adds two additional poles to the system and no zeros. The frequency response of Equation 2.22 has some desirable characteristics when designing a controller in the frequency domain. First, is the ease of using the filter because the parameters can be easily tuned from a measured transfer function of the system. Second, is that above the resonant frequency of the filter, the magnitude rolls-off at 40 dB per decade. This roll-off causes the high frequency dynamics of the system to remain unaffected by the filter. One problem with the filter occurs when multiple filters are used to control multiple modes. The filter has a flat response at frequencies below the filter resonant frequency and will sometimes cause an increase in the magnitude response at lower frequencies. Figure 2.9 shows the bode plot of a representative PPF filter where the filter frequency is set at 233 Hz, the damping ratio is set at 0.08, and the gain is set at 1. The figure shows the flat response at low frequency and the roll-off of 40 dB per decade at high frequency. The phase of the filter is changing from 0 to 180 degrees near the resonance frequency of the

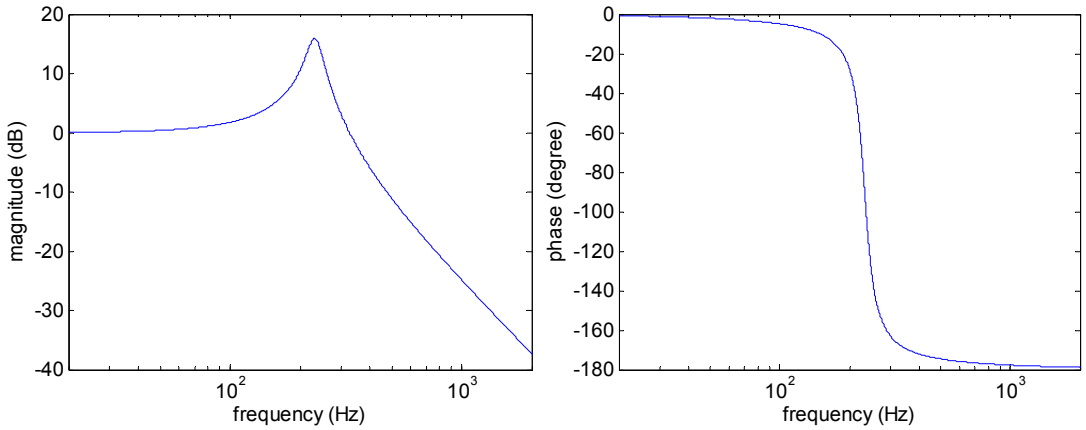

Figure 2.9. Bode plot of a PPF filter with a gain of 1, filter frequency of 233 Hz, and damping ratio of 0.08.

filter. The phase change causes the feedback signal to be out of phase with the input near the resonance frequency of the filter and therefore the output of the closed-loop system is reduced over the frequency range where the phase change is occurring.

2.4.1 Literature Review of PPF Filter Design

McEver (1999) derived an optimization algorithm for setting a PPF filter. The algorithm was designed from a pole/zero model of a system and was reported to be suitable for using with collocated actuator/sensor pairs where the pole/zero relationship would be similar to the pole/zero relationship of Figure 2.8. The result of the algorithm is as follows with the nomenclature following the algorithm:

1) Choose PPF filter gain g, positive if $\omega_{pz} > 1$, negative if $\omega_{pz} < 1$
2) Calculate ω_{fp} from the following equation

$$\omega_{fp} = \sqrt{\frac{1}{\left(1 - g\omega_{pz}^2\right)}} \tag{2.23}$$

3) Choose the closed-loop pole spacing α to be 1
4) Calculate the closed-loop damping ratio ζ_{CL} from equation

$$\zeta_{CL} = \sqrt{\frac{\omega_{fp}^2\left(1-g\right)+1-\alpha-1/\alpha}{4}} \tag{2.24}$$

5) Calculate the required PPF filter damping ratio ζ_f from equation

$$\zeta_f = \frac{\zeta_{CL}\left(1/\sqrt{\alpha}+\sqrt{\alpha}\right)}{\omega_{fp}}. \tag{2.25}$$

The definition of the variables from the above algorithm is as follows: ω_{pz} is the ratio of the zero to the pole (ω_z/ω_p) and will always be greater than one if the zero follows the pole in collocated measurements; ω_{fp} is the ratio of the PPF filter frequency to the pole frequency (ω_f/ω_p); α is the multiple of the two closed-loop frequencies from the system and the controller when the system and controller have the same damping ratio; ζ_{CL} is the closed-loop damping ratio; and ζ_f is the PPF filter damping ratio.

Fanson and Caughey (1987) provided equations for calculating the damping ratio and frequency of the filter using a root locus design. These equations were derived by Goh (1983) and the damping ratio (ζ_f) of the filter is

$$\zeta_f = \left[\frac{\left(1.02\zeta_p^2\right)^2}{\left(1.02\zeta_p^2\right)^2 + 0.16} \right]^{1/2} \tag{2.26}$$

where ζ_p is the damping of the particular mode of interest. The filter frequency (ω_f) is

$$\omega_f = \frac{\omega_p}{1.02\sqrt{1-\zeta_p^2}} \tag{2.27}$$

where ω_p is the pole frequency of the particular mode of interest. Fanson reports that the closed-loop system will be stable according to a Nyquist stability analysis as long as the filter gain is between 0 and 1.

Other authors (DeGuilio, 2000 and Farinholt, 2001) have reported setting the filter frequencies either at a set multiple of the system's pole frequencies or in a certain range above the system's pole frequencies. Then the filter can be tuned according to the results of the closed loop results. Both authors reported having stability issues with lower modes as multiple modes were controlled and suggested using an up/down approach which starts the design of the controller by setting the control filter for the highest mode to be controlled and continuing the filter designs to the lowest mode. Therefore as the flat response or low frequency spillover of the filter affects the lower modes, compensation with the next filter helps alleviate control spillover into lower modes.

2.4.2 Analytical Duct Control Studies

McEver's algorithm and Goh's equations are used to define PPF control parameters and then the parameters are used to simulate the closed-loop system

performance. The PPF filters are defined as transfer functions as shown in Equation 2.22. A PPF filter is designed for each mode to be controlled of the model using the two methosd presented for setting the control parameters. Each filter transfer function is summed together to form one compensator transfer function (K_{ppf}), where

$$K_{ppf}(s) = K_1(s) + K_2(s) + \ldots \tag{2.28}$$

and the subscripts of the individual PPF filters are determined by the mode where the PPF filter is designed. The simulated closed-loop transfer function (H_1) for the collocated position (P_1/V_i) with a positive compensator in the feedback loop (Dorf and Bishop, 2001, pp 65-66) is defined as

$$H_1(s) = \frac{G(s)}{1 - G(s)K_{ppf}(s)} \tag{2.29}$$

where G is the collocated model of the plant. The transfer functions for the other locations (P_2/V_i and P_3/V_i) are found by the following equations

$$H_2(s) = H_1(s)G_1(s) \tag{2.30}$$

$$H_3(s) = H_1(s)G_2(s) \tag{2.31}$$

where G_1 is the model result of P_2 divided by P_1 and G_2 is the model result of P_3 divided by P_1. Figure 2.10 shows a block diagram of the system where the variables from Equations 2.29, 2.30, and 2.31 are used to obtain the transfer functions of the closed-loop modeled system.

When designing the compensator, K_{ppf}, using McEver's optimization algorithm, the gains for each mode are initially set to 0.05. The ratios of the zero to the pole (ω_{pz}) are calculated from each mode where the counterpart frequency of the highest magnitude point of each mode is used to assume the pole frequency and the counterpart frequency of the lowest magnitude point following the pole frequency is used to assume the zero frequency. This ratio and the gain of each mode are inserted into Equation 2.23 to find

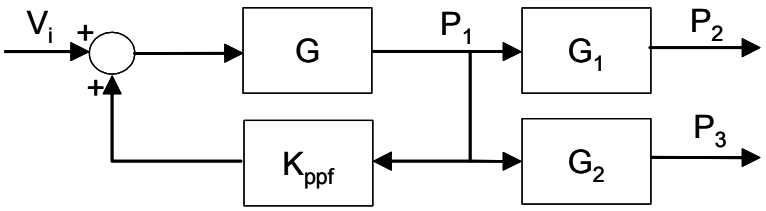

Figure 2.10. Control block diagram of the cylindrical duct used to obtain the simulated control of the system.

the PPF frequency for each filter. The closed-loop damping for each mode is found from Equation 2.24 assuming that α is 1. Equation 2.25 is then used to find the PPF damping ratio for the filter of each mode. The results of this algorithm are found in Table 2.5. Equation 2.22 is used to formulate a transfer function for each modal filter that is added together to form the overall compensator K_{ppf}.

Once the compensator is formed, Equation 2.29 is used to simulate the closed-loop system of the P_1/V_i transfer function. Figure 2.11 shows the uncontrolled model overlaid by the closed-loop model with 4 PPF filters designed using McEver's optimization algorithm for the second through fifth modes of the system. The magnitude increase of the second mode is caused by control spillover inherent when using multiple PPF filters. Analyzing the closed-loop response as each additional filter is added to the compensator shows the low frequency spillover increasing with each additional filter as reported by DeGuilio (2000). Appendix B shows a series of figures of the analytical control results (P_1/V_i) as additional filters are added to the compensator using a top/down approach. These figures show how the spillover is made more severe with the addition of each PPF filter. Appendix B also shows the analytical closed-loop results of this simulation for the P_2/V_i and P_3/V_i transfer functions.

Table 2.5. Positive position feedback controller properties obtained using McEver's algorithm.

mode	gain	frequency (Hz)	damping ratio
2	0.05	118.5	0.1144
3	0.05	209.5	0.0967
4	0.05	303.0	0.0860
5	0.05	398.0	0.0784

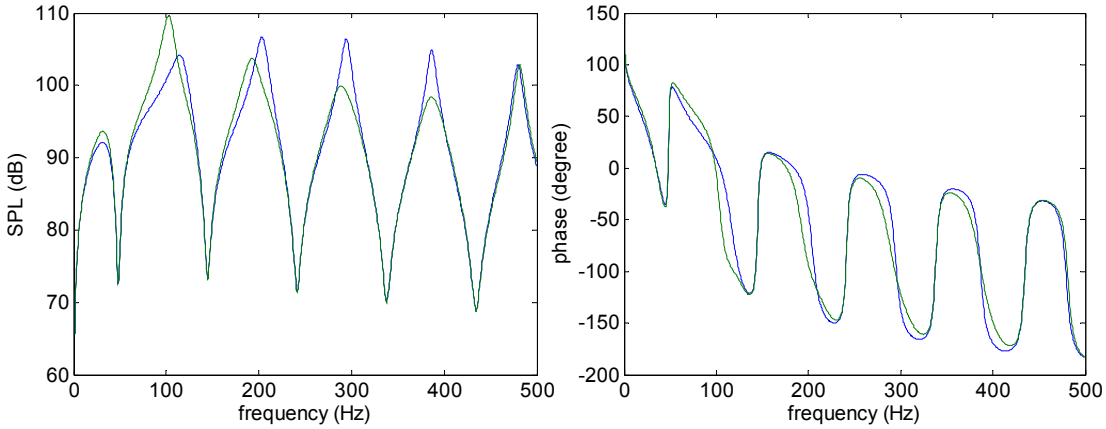

Figure 2.11. Analytical collocated transfer function model (blue) of the enclosure with the analytical closed-loop controlled (McEver's algorithm) model (green) overlaid on top.

The previous filter parameters defined using McEver's algorithm are retuned from the closed-loop results for improved closed-loop performance. Figure 2.12 shows the uncontrolled model (P_1/V_i) overlaid by the analytical closed-loop model with the frequencies from Table 2.5 retuned for better closed-loop performance. The filters for the second and third modes are reduced by 25 Hz and the filter for the fourth mode is reduced by 10 Hz. Again, Equation 2.22 is used to define each filter and the total compensator is the summation of each PPF filter transfer function. These filter values are found experimentally by changing the filter parameters incrementally up and down until the closed-loop response provides better results and Table 2.6 shows the filter parameter used in this retuned case. This change produces better magnitude results in the simulated closed-loop response, as the magnitude of the second mode is reduced significantly with the retuned PPF parameters. The damping added by the PPF filter for the second mode reduces the effects of the low frequency spillover from the filters of the higher modes. The closed-loop results for the P_2/V_i and P_3/V_i transfer functions in the duct with the filter frequencies retuned can be seen in Appendix B.

Next, Goh's equations are used to design the filter parameters for the second through the fifth modes of the model. The gains are set at 0.05 and Equations 2.26 and

Table 2.6. Positive position feedback controller properties obtained using McEver's algorithm with retuned frequency values.

mode	gain	frequency (Hz)	damping ratio
2	0.05	93.5	0.1144
3	0.05	184.5	0.0967
4	0.05	293.0	0.0860
5	0.05	398.0	0.0784

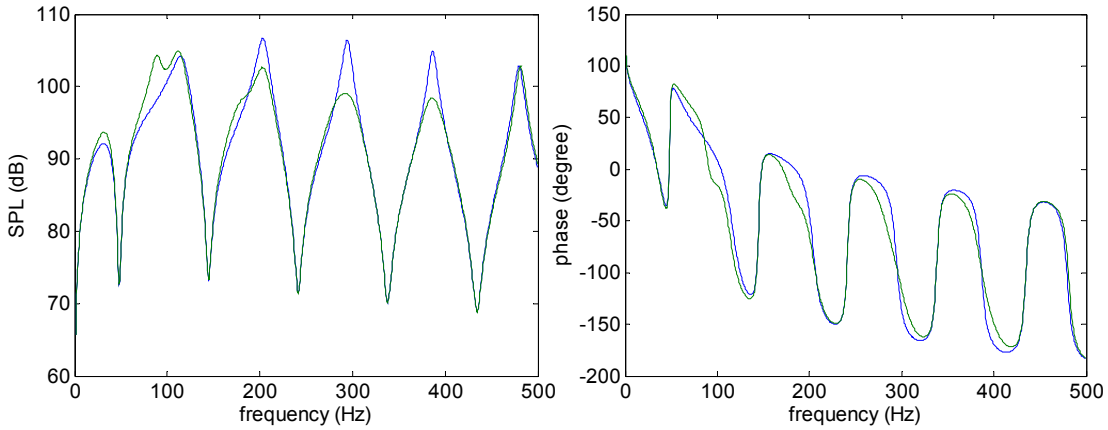

Figure 2.12. Analytical collocated transfer function model (blue) of the enclosure with the retuned analytical closed-loop controlled (McEver's algorithm) model (green) overlaid on top.

2.27 are used to set the filter parameters where the pole frequency of the system is assumed to be the frequency associated with the peak magnitude of each mode and the damping ratio is found using Equation 2.19. Table 2.7 shows the parameter values used for each PPF filter (K_i) where the compensator (K_{ppf}) is the sum of each PPF filter.

Figure 2.13 shows the uncontrolled model overlaid by the simulated closed-loop model with 4 PPF filters designed using Goh's equations. This design adds very low damping to the modes and causes a "notch" effect at the resonant frequency of each PPF filter. This "notch" effect causes a large reduction over a very small frequency band, but a very large increase in the magnitude of some modes outside of that small frequency band. Overall, the original peak magnitude of each mode is reduced, but the notch causes a split mode effect and one of the peaks on the side of each split is higher than the magnitude before control is added.

Adding additional damping to the PPF filters reduces this notch effect. So the damping is increased and the results re-simulated to eliminate the notch effect. Good simulation results require the filter damping ratios found for the fourth and fifth modes to be multiplied by 100, the damping ratio of the third mode to be multiplied by 50, and the damping ratio of the second mode to be multiplied by 8. The filter frequencies are

Table 2.7. Positive position feedback controller properties obtained using Goh's design equations.

mode	gain	frequency (Hz)	damping ratio
2	0.05	112.5	0.0205
3	0.05	199.2	0.0022
4	0.05	288.4	0.0007
5	0.05	379.1	0.0003

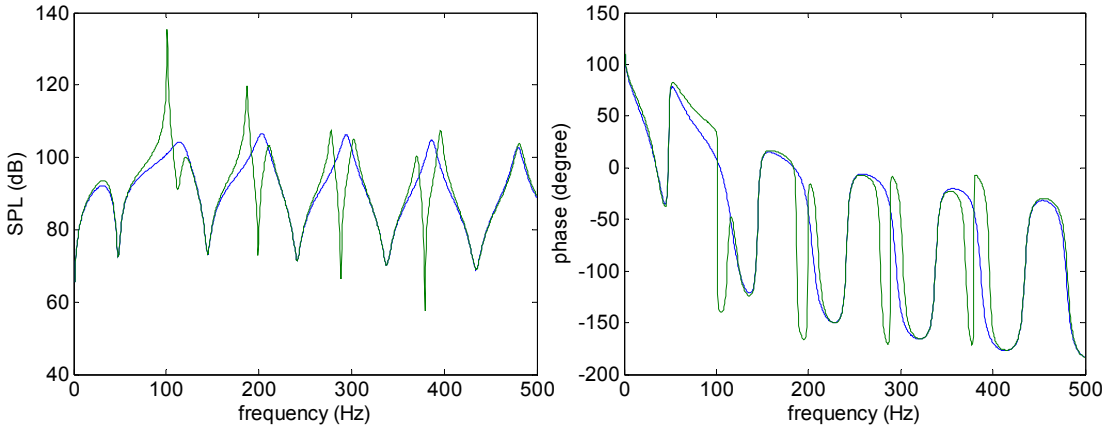

Figure 2.13. Analytical collocated transfer function model (blue) of the enclosure with the analytical closed loop controlled (Goh's equations) model (green) overlaid on top.

Table 2.8. Positive position feedback controller properties obtained using Goh's design equations with retuned frequency and damping ratio values.

mode	gain	frequency (Hz)	damping ratio
2	0.05	92.5	0.1632
3	0.05	184.2	0.1112
4	0.05	288.4	0.0665
5	0.05	389.1	0.0308

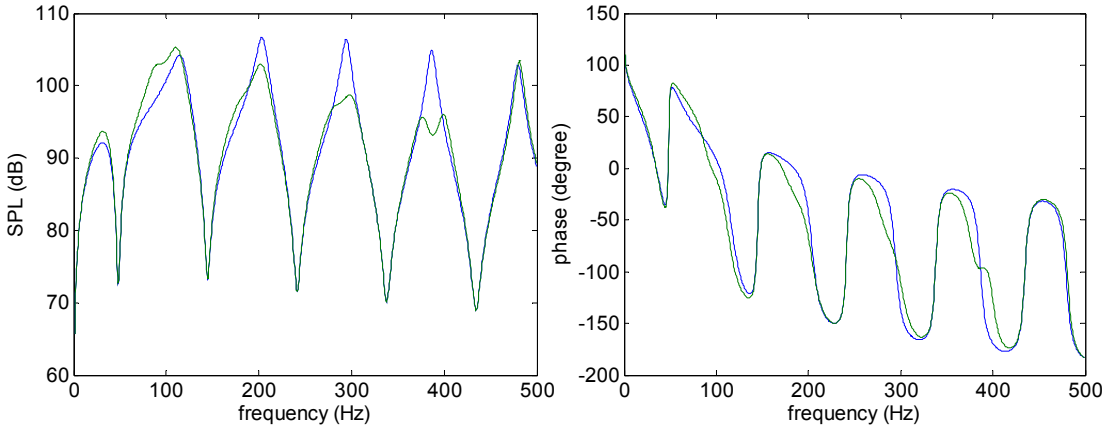

Figure 2.14. Analytical collocated model (blue) of the duct with the retuned analytical closed loop controlled (Goh's equations) model (green) overlaid on top.

retuned as well where the frequency of the second mode is decreased by 20 Hz, the frequency of the third mode is decreased by 15 Hz, and the frequency of the fifth mode is increased by 10 Hz. The exact values for each retuned filter can be seen in Table 2.8.

As before, the compensator (K_{ppf}) for the system is the summation of the transfer function of each PPF filter (K_i). Figure 2.14 shows the uncontrolled model (P_1/V_i) overlaid by the simulated closed-loop model results using the compensator defined from Table 2.8. This retuned controller produces magnitude reduction results that are better then the original simulations using Goh's equations and McEver's algorithm and comparable to the retuned case of McEver's algorithm.

2.5 Chapter Summary

In this chapter an impedance model of a cylindrical duct enclosure is presented. The model is verified with measured data from 0 to 500 Hz and the pole and zero frequencies, after the first pole and zero frequency, are within 5 percent of the measured data. The low frequency error is caused by the un-modeled amplifier dynamics. Positive position feedback (PPF) is presented as a potential controller for sound absorption by

adding additional damping to modes of interest in the system. PPF is defined and a literature review of work done on setting the filter parameters is presented. Analytical control studies are presented with 2 ways of setting the filter parameters, McEver's algorithm and Goh's equations. The closed-loop control studies are compared to the analytical model of the system without control in order to show the potential reduction in the SPL of the system when control is added over the frequency band where control is implemented. The next chapter will look at actual control results of measured data for the cylindrical duct that is modeled, how the spill-over at low frequency is diminished, how collocated measured data is used to estimate the closed-loop performance for different control schemes, and how the controller is used to reduce the SPL in the fairing model.

Chapter 3

Non-Adaptive Control

3.1 Introduction

The previous chapter presents a model for a cylindrical duct acoustic enclosure, defines positive position feedback (PPF) control, and simulates control on the model of the acoustic enclosure. Because the simulated control shows that energy absorption can be obtained using PPF control, the work presented in this chapter is the implementation of the control in the presence of an acoustic disturbance. This chapter focuses on employing control in the cylindrical duct and full scale fairing simulator when the interior acoustic characteristics are maintained constant. Implementing the control in a system with non-changing acoustic characteristics will be called non-adaptive control. Non-adaptive control is tested on both systems in two ways: (1) the disturbance and control signal are overlaid on the control actuator and (2) the disturbance signal is sent to another disturbance source in or by the system. The sound pressure reduction for the tests is quantified for the magnitude pressure reduction of the system by means of the sound pressure level (SPL) where the reduction of the SPL is the difference in the controlled and non-controlled cases. Also included in this chapter is an explanation of how spill-over into lower modes, caused by the use of multiple PPF filters, is diminished.

3.2 Positive Position Feedback Control on the Enclosure

The retuned control filters designed from the model using McEver's algorithm and Goh's equations in the previous chapter are tested on the cylindrical duct in order to

see the control effectiveness. The PPF filters are discretized using a z-transform (Smith, 1999, p 626) where a discretized PPF filter is

$$K(z)=\frac{\dfrac{(\omega T)^2 z^2}{(\omega T)^2+4\zeta(\omega T)+4}+\dfrac{2(\omega T)^2 z}{(\omega T)^2+4\zeta(\omega T)+4}+\dfrac{(\omega T)^2}{(\omega T)^2+4\zeta(\omega T)+4}}{z^2+\dfrac{\left(2(\omega T)^2-8\right)z}{(\omega T)^2+4\zeta(\omega T)+4}+\dfrac{(\omega T)^2-4\zeta(\omega T)+4}{(\omega T)^2+4\zeta(\omega T)+4}}. \quad (3.1)$$

The discretized transfer function is a function of filter frequency (ω), filter damping (ζ), and the discrete time step (T). The filter parameters obtained from both designs are used with Equation 3.1 to make discretized transfer functions of each PPF filter with the parameters taken from Tables 2.5 and 2.7. The control is applied using a dSpace 1104 processor board where the processor is coded from a Simulink block diagram. Figure 3.1 shows the block diagram where the collocated microphone signal (P_1 in Figure 2.5) and random disturbance signal (V_i in Figure 2.5) are inputs into the board. The collocated microphone signal and combined disturbance/control signal are outputs. The filter transfer function for each mode is added together to form one compensator transfer function (K_{ppf}) that is placed in the feedback path of the collocated microphone signal input. This feedback compensated signal is added to the disturbance signal and sent to the actuator. A Siglab unit is used to produce the disturbance signal and measure the transfer functions of the system as described in the previous chapter where the disturbance signal is a 0 to 1000 Hz random 0.05 RMS voltage.

The first control test uses the compensator designed using McEver's algorithm to find individual PPF filter parameters from simulations of the modeled cylindrical duct.

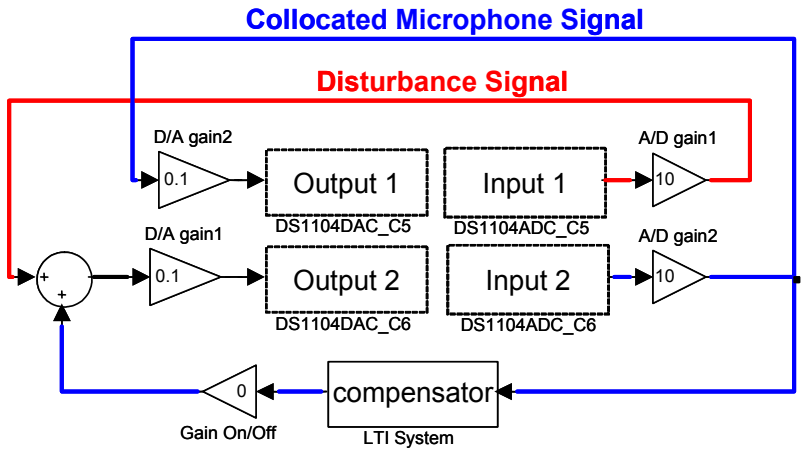

Figure 3.1. Simulink block diagram used to program the processor board showing the collocated microphone (blue) and disturbance (red) signal inputs.

Table 2.6 shows the parameters used with Equation 3.1 to define each modal filter with a sample rate of 5000 Hz. Each PPF filter is added together to form one compensator that is inserted into the compensator block of the block diagram of Figure 3.1. The diagram is compiled and downloaded to the dSpace processor. Control Desk software is used to control the On/Off gain in the feedback loop of Figure 3.1 where the gain is slowly increased from 0 in increments of 0.01. The control transfer function is periodically measured to see magnitude reductions and/or amplifications caused by control. The On/Off gain allows the control operator to see the percent difference of the actual control gain compared to the gains used to define the compensator in Table 2.6 from the analytical model.

The result of the measured collocated location transfer function (P_1/V_i) with the second through fifth modes controlled using the designed compensator from McEver's algorithm is shown in Figure 3.2 with the On/Off gain at 50 percent. This control result is overlain on the measured collocated location transfer function without control to show the magnitude reduction and amplification caused by control. The ordinate of the magnitude plot is the measured microphone voltage divided by the input disturbance voltage from Siglab in decibels, the ordinate of the phase plot is in degrees, and the abscissa is the frequency in Hz. The measured P_2/V_i and P_3/V_i transfer functions of the duct with and without control can be seen in Appendix C.

The gain of the controller is not increased to the designed gain in Table 2.6. The closed-loop response goes unstable at 75 percent of the defined compensator gain

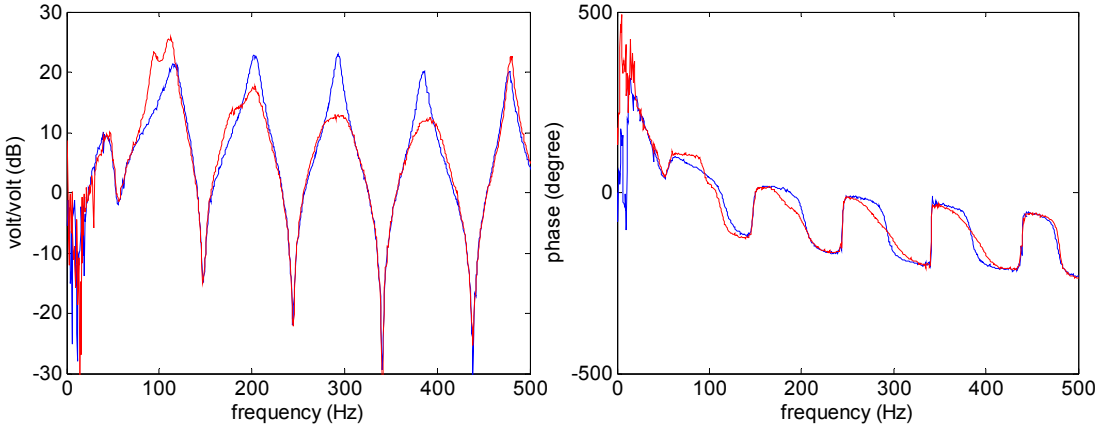

Figure 3.2. Measured collocated transfer function (blue) of the duct with the measured controlled (McEver's algorithm) closed-loop transfer function (red) overlaid on top.

because the spillover of the combined filters causes the magnitude of the second mode to increase infinitely. The control results with a 50 percent gain show that the compensator is adding damping to each of the four modes where control is applied. The sixth mode magnitude is slightly increased showing that some high frequency spillover is affecting the magnitudes of higher modes, but not significantly. The low frequency spillover, as explain by DeGuilio (2000), inherent with PPF control is increasing the magnitude of the lower modes. The spillover effect is not obvious in the third mode but is obvious in the second mode where the magnitude is increased pass the uncontrolled results. Damping is being added to the second mode as seen by the split peaks, but the overall magnitude of the mode is increased because of the spillover effect and energy is added to that mode.

To quantify the effectiveness of the controller, the SPL reduction is calculated, or the difference in SPL between the controlled and uncontrolled cases. The SPL is calculated from the autospectrum measurement of the microphone data. Bies and Hansen (2003, p 47) explain that the square of incoherent pressure signals can be added together to form one overall pressure p_t as follows,

$$\left(p_t^2\right) = \left(p_1^2\right) + \left(p_2^2\right) + \ldots \tag{3.2}$$

where p_i are the incoherent pressures. For this research the pressure of Equation 3.2 is replaced with the measured autospectrum voltage because the pressure is proportionally related to the voltage by the microphone sensitivity. The frequency range for the incoherent measurement is limited to the 100 to 500 Hz range unless otherwise stated. The SPL reduction can be found from

$$SPL_{reduction} = 20\log_{10}\left[p_{t\_control} \Big/ p_{t\_ref} \right] \tag{3.3}$$

where $p_{t\_control}$ is the total voltage of the controlled system calculated from the autospectrum data and p_{t_ref} is the total voltage of the baseline system calculated from the autospectrum data.

The SPL reduction for Figure 3.2 is found using Equations 3.2 and 3.3. The SPL reduction is 0.1, 2.4, and 0.0 dB for P_1, P_2, and P_3 measurements respectively as defined in Figure 2.5. These values indicate that SPL reduction is occurring in the middle of the duct and the SPL is the same for the controlled and baseline cases at the ends of the duct. The second mode's magnitude increases at P_1 and P_3 because of the low frequency

spillover inherent when using multiple PPF filters is the cause of there being no reduction at P_1 and P_3. The P_2/V_i transfer function has a node at the second mode and the magnitude is not increased at that mode. This low frequency spillover effect suggests that either fewer PPF filters need to be used with the system or the control needs to be modified to eliminate this spillover effect.

Next, the compensator designed from Goh's filter equations is used for acoustic energy absorption experiments in the duct. The parameters for each modal filter are found in Table 2.8. Again, the parameters are used with Equation 3.1 at a sampling rate of 5000 Hz to produce a transfer function (K_i) for each filter that are summed together to form one compensator (K_{ppf}). The block diagram from Figure 3.1 is used again to implement the control. Figure 3.3 shows the results of the P_1/V_i transfer functions for the non-controlled and the controlled cases with the compensator designed from Goh's equations. As before, stability is an issue when the gain value is increased to 75 percent, so the On/Off gain for the controlled results is set at 50 percent for the figure below. The SPL reductions for the controlled results are -0.7, 2.3, and -0.8 dB for the P_1, P_2, and P_3 measurements respectively. The negative sings indicate an increase in SPL and that the feedback controller is adding energy to the system. This increase is again caused by the inherent spillover associated with using multiple PPF filters for control. The control measurement plots for the P_2/V_i and P_3/V_i transfer functions can be found in Appendix C.

Both controllers described above and implemented for control with acoustic disturbances in the duct are absorbing acoustic energy at higher frequencies and adding energy to lower frequencies. Moving energy from high frequency to low frequency could

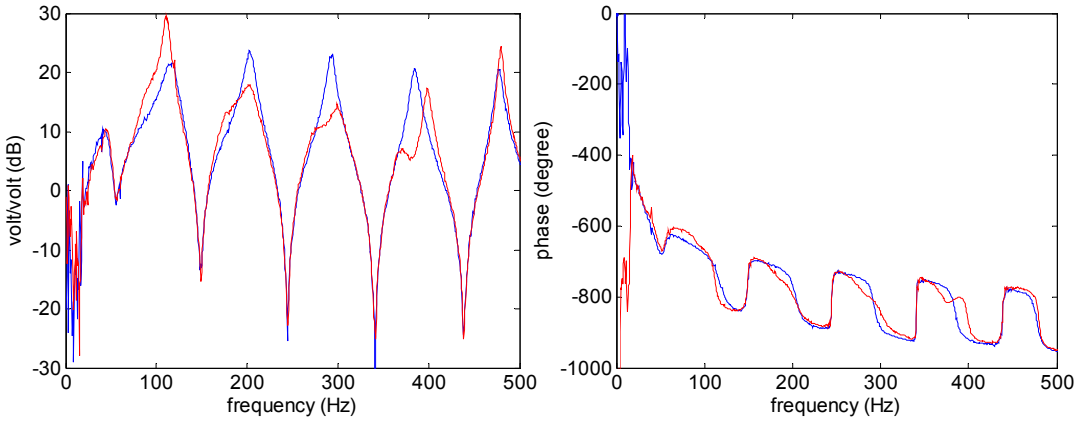

Figure 3.3. Measured collocated transfer function (blue) of the enclosure with the measured controlled (Goh's equations) closed-loop transfer function (red) overlaid on top.

be useful in certain applications, but is not practical for this application. Therefore the controller needs to be designed without low frequency spillover or the simultaneous use of multiple PPF filters will not be suitable for this application.

3.3 Positive Position Feedback Filter Modifications

Since the use of multiple PPF filters increases the magnitude of the second mode, changing the filter to reduce or eliminate the low frequency spill-over is vital for adding damping and globally absorbing acoustic energy. Figure 2.9 shows the bode plot of a representative PPF filter where the filter frequency is set at 233 Hz, the damping ratio is set at 0.08, and the gain is set at 1. This figure shows the high frequency roll-off of 40 dB per decade above the resonance filter frequency and the flat magnitude response at low frequency.

The low frequency flat response is the source of the low frequency spillover of the previous control results. The added closed-loop system damping is a result of the filter being out of phase with the disturbance therefore absorbing acoustic energy. A lightly damped filter is out of phase over a very short frequency band and is the reason for the "notch" effect as seen in Figure 2.13 of the simulated control results using Goh's equations. The filter phase of the flat response at low frequency is in-phase with the output and causes the closed-loop magnitude at lower frequencies to increase. This magnitude amplification is the spillover effect explained by DeGuilio (2000) and seen in the previous control results. The same amplification would happen at higher frequency, but the magnitude response is rolling-off and therefore causes little to no amplification. To reduce this spillover effect at low frequency a high-pass Butterworth filter is employed to add low frequency roll-up to the PPF filter. An additional low-pass Butterworth filter is used as well, to increase the high frequency roll-off rate.

3.3.1 Butterworth Filter and Combined Filter Definition

Butterworth filters are filters that have a flat frequency response over a certain frequency band and constant roll-off over the remaining frequency band. A high-pass Butterworth filter transfer function is

$$G_{h\_butter}(s) = \frac{s^n}{s^n + as^{n-1} + a_1 s^{n-2} \ldots + a_{n-2} s^2 + a_{n-1} s + \omega^n} \tag{3.4}$$

where ω is the cut-off frequency of the filter, a_j are constants, and n is the order of the filter. The transfer function of a low-pass Butterworth filter is

$$G_{l\_butter}(s) = \frac{\omega^n}{s^n + as^{n-1} + a_1 s^{n-2} \ldots + a_{n-2} s^2 + a_{n-1} s + \omega^n}. \tag{3.5}$$

The high-pass Butterworth filter adds n zeros at the origin of the s-plane and n poles, with the pole locations to be described below. The low-pass filter only adds n poles in the s-plane. The cut-off frequency of the filters is where the response changes from a flat response to a constant roll-off (low-pass filters) or from a constant roll-up to a flat response (high-pass filter).

The constants of the denominator for both the high- and low-pass Butterworth filters can be calculated (Smith, 2006, University of Illinois at Chicago, 2006) from the pole locations of the filter. All of the poles of the transfer function are located on a semicircle in the left half of the s-plane with a radius of ω. The poles will be evenly spaced on the semicircle and therefore the angle (θ) of lines from the origin to adjacent poles will be

$$\theta = 180/n. \tag{3.6}$$

Odd ordered filters will have one pole on the real axis and even ordered filters will have none on the real axis. Therefore, an odd ordered filter will have one pole on the real axis and the next two will be θ degrees away on the semicircle in the positive and negative directions, as found by Equation 3.6, creating a complex conjugate pair. The next set of poles will be θ away from the previously found poles and so forth creating additional complex conjugate pairs, until there is the same number of poles as the order of the filter. For an even filter, the first complex conjugate pair is

$$\theta = 90/n \tag{3.7}$$

away from the real axis on the semicircle. The remaining poles are found in the same fashion as an odd filter. Figure 3.4 shows an example of a sixth order Butterworth filter with the cut-off frequency set at 10 rad/s with the angles between the poles found from Equations 3.6 and 3.7 showing how the pole locations can be found in the s-plane.

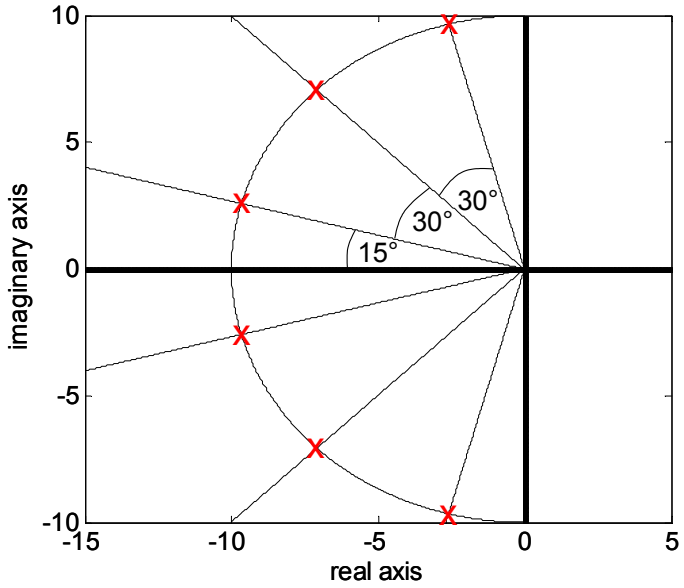

Figure 3.4. The poles of a low-pass sixth order Butterworth filter with the cut-off frequency set at 10 rad/s.

For this research a sixth order high-pass and a second order low-pass Butterworth filter are used because these filters provided good control results on the systems tested. Using the above description, a sixth order high-pass Butterworth filter transfer function is found to be

$$G_{h\_6\_butter}(s) = \frac{s^6}{s^6 + 2\omega a_1 s^5 + \omega^2 a_2 s^4 + 2\omega^3 a_3 s^3 + \omega^4 a_2 s^2 + 2\omega^5 a_1 s + \omega^6} \qquad (3.8)$$

where

$$a_1 = \sin(15^\circ) + \sin(45^\circ) + \sin(75^\circ)$$

$$a_2 = 3 + 4\sin(15^\circ)\sin(45^\circ) + 4\sin(15^\circ)\sin(75^\circ) + 4\sin(45^\circ)\sin(75^\circ)$$

$$a_3 = 2\sin(15^\circ) + 2\sin(45^\circ) + 2\sin(75^\circ) + 4\sin(15^\circ)\sin(45^\circ)\sin(75^\circ)$$

The second order low-pass filter is

$$G_{l\_2\_butter}(s) = \frac{\omega^2}{s^2 + \sqrt{2}\omega s + \omega^2}. \qquad (3.9)$$

Figure 3.5 shows a representative bode plot of the product of Equations 3.8 and 3.9 where the cutoff frequency for Equation 3.8 is set to 143 Hz and the cutoff frequency for Equation 3.9 is set to 233 Hz. Also included is the PPF filter from Figure 2.9 for visually comparing the PPF filter and the Butterworth filters. The combination Butterworth filter

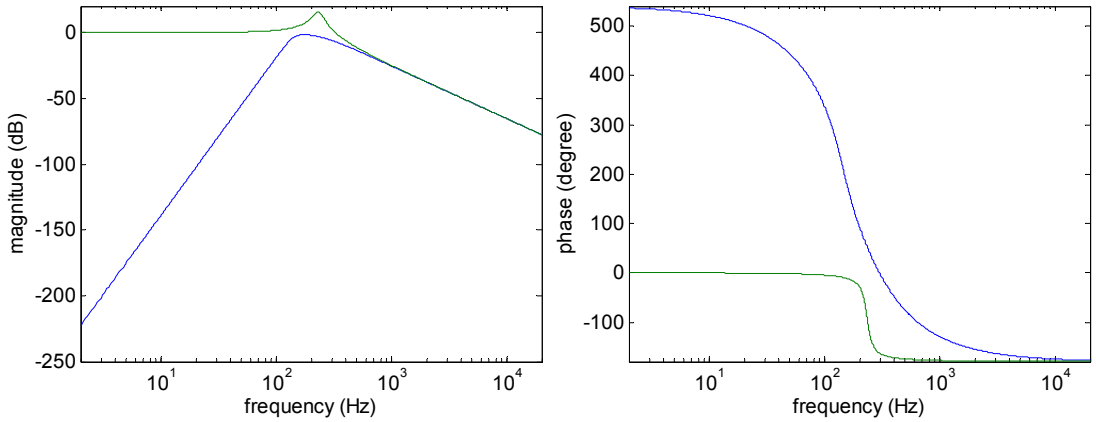

Figure 3.5. Bode plot of combination high and low-pass Butterworth filters (blue) overlaid with the PPF filter (green).

creates a modified bandpass filter. The band in this case is about 90 Hz. The combination Butterworth filter low frequency roll-up is 120 dB per decade and the high frequency roll-off is 40 dB per decade. This combination Butterworth filter is described as a modified bandpass filter because traditional Butterworth bandpass filters have the same roll-up and roll-off rate on each side of the flat response.

The PPF filter is changed by multiplying it by the modified Butterworth bandpass filter setting the bandpass where the PPF filter is to be applied. The combination of the three filters will be defined as the *combined filter*. Figure 3.6 shows a representative bode plot of the combined filter overlaid with the bode plot of the PPF filter for visual comparison. The combined filter low frequency roll-up is determined by the high-pass Butterworth filter which is 120 dB per decade. The combined filter high frequency roll-off is determined by the PPF filter and the low-pass Butterworth filter which results in a

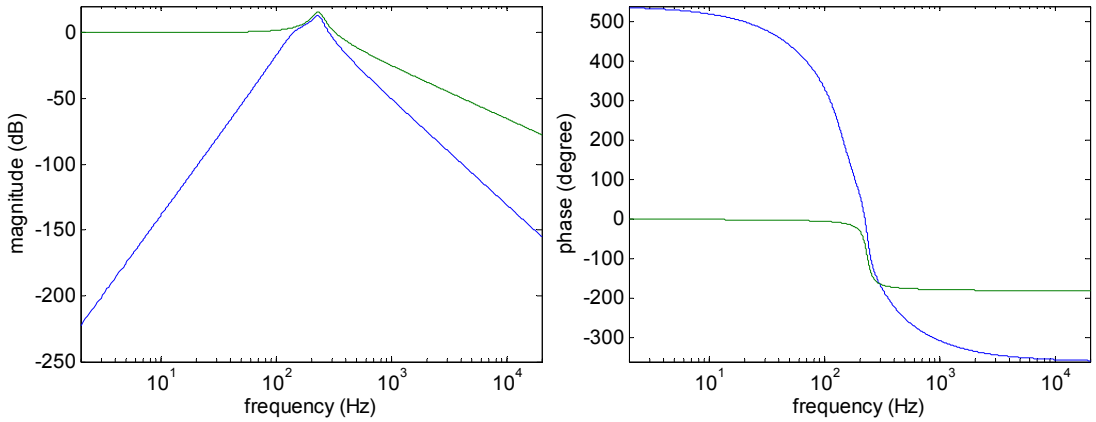

Figure 3.6. Bode plot of the combined filter (blue) overlaid with the bode plot of the PPF filter (green).

roll-off of 80 dB per decade. The combined filter contains 10 poles and 6 zeros and therefore the phase of the filter starts at 540 degrees because of the 6 zeros introduced by the high-pass Butterworth filter at the origin and levels off at -360 degrees. The phase at the location where the PPF filter adds damping to the closed-loop system is in phase with the output, therefore, for the feedback signal to be out of phase with the output the gains need to be negative.

The discretized form of the high-pass and low-pass Butterworth filters can be found using a z-transformation (Smith, 1999, p 626). The sixth order high-pass discretized Butterworth filter will be

$$G_h(z) = \frac{\frac{64}{T^6 A} z^6 - \frac{384}{T^6 A} z^5 + \frac{960}{T^6 A} z^4 - \frac{1280}{T^6 A} z^3 + \frac{960}{T^6 A} z^2 - \frac{384}{T^6 A} z + \frac{64}{T^6 A}}{z^6 + \frac{B}{A} z^5 + \frac{C}{A} z^4 + \frac{D}{A} z^3 + \frac{E}{A} z^2 + \frac{F}{A} z + \frac{G}{A}} \tag{3.10}$$

where

$$A = \frac{64}{T^6} + \frac{64\omega a}{T^5} + \frac{16\omega^2 b}{T^4} + \frac{16\omega^3 c}{T^3} + \frac{4\omega^4 b}{T^2} + \frac{4\omega^5 a}{T} + \omega^6$$

$$B = \frac{-384}{T^6} - \frac{256\omega a}{T^5} - \frac{32\omega^2 b}{T^4} + \frac{8\omega^4 b}{T^2} + \frac{16\omega^5 a}{T} + 6\omega^6$$

$$C = \frac{960}{T^6} + \frac{320\omega a}{T^5} - \frac{16\omega^2 b}{T^4} - \frac{48\omega^3 c}{T^3} - \frac{4\omega^4 b}{T^2} + \frac{20\omega^5 a}{T} + 15\omega^6$$

$$D = \frac{-1260}{T^6} + \frac{64\omega^2 b}{T^4} - \frac{16\omega^4 b}{T^2} + \frac{4\omega^5 a}{T} + 20\omega^6$$

$$E = \frac{960}{T^6} - \frac{320\omega a}{T^5} - \frac{16\omega^2 b}{T^4} + \frac{48\omega^3 c}{T^3} - \frac{4\omega^4 b}{T^2} - \frac{20\omega^5 a}{T} + 15\omega^6$$

$$F = \frac{-384}{T^6} + \frac{256\omega a}{T^5} - \frac{32\omega^2 b}{T^4} + \frac{8\omega^4 b}{T^2} - \frac{16\omega^5 a}{T} + 6\omega^6$$

$$G = \frac{64}{T^6} - \frac{64\omega a}{T^5} + \frac{16\omega^2 b}{T^4} - \frac{16\omega^3 c}{T^3} + \frac{4\omega^4 b}{T^2} - \frac{4\omega^5 a}{T} + \omega^6$$

The second order low-pass discretized Butterworth filter is

$$G_t(z) = \frac{\dfrac{(\omega T)^2 z^2}{(\omega T)^2 + 2\sqrt{2}(\omega T) + 4} + \dfrac{2(\omega T)^2 z}{(\omega T)^2 + 2\sqrt{2}(\omega T) + 4} + \dfrac{(\omega T)^2}{(\omega T)^2 + 2\sqrt{2}(\omega T) + 4}}{z^2 + \dfrac{\left(2(\omega T)^2 - 8\right)z}{(\omega T)^2 + 2\sqrt{2}(\omega T) + 4} + \dfrac{(\omega T)^2 + 2\sqrt{2}(\omega T) + 4}{(\omega T)^2 + 2\sqrt{2}(\omega T) + 4}}. \quad (3.11)$$

A top/down approach for designing the combined filters is employed as explained by DeGuilo (2000) for PPF filter design. The combined filters for each mode are added together to form one compensator, now defined as K_t, that is used in the Simulink control block diagram as shown in Figure 3.1. A sampling rate of 5000 Hz is used as with the previous control measurements. The measured collocated transfer function (P_1/V_i) of the duct with and without control is shown in Figure 3.7 with the parameters of the combined filters shown in Table 3.1. As before, the plots of the P_2/V_i and P_3/V_i transfer functions for the controlled and uncontrolled cases can be seen in Appendix C.

The addition of the Butterworth filters to the PPF filter eliminates any substantial low frequency spillover in the closed-loop transfer functions. Eliminating this spillover causes the speaker to actively add damping to the lower modes more effectively and absorb acoustic energy at all locations. The SPL reduction of the closed-loop system, of

Table 3.1. Combined filter properties for control simulation. Frequencies are in Hz.

mode	gain	PPF frequency	damping ratio	high-pass cutoff	low-pass cutoff
2	-0.0265	143	0.08	53	143
3	-0.0219	233	0.08	143	233
4	-0.0236	325	0.08	233	325
5	-0.0235	419	0.08	325	419
6	-0.0147	510	0.08	419	510

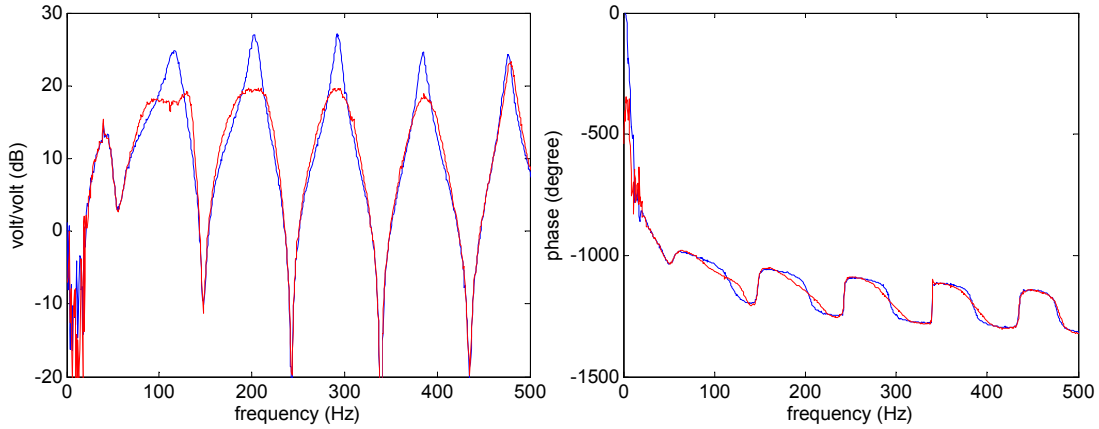

Figure 3.7. Measured collocated transfer function (blue) of the duct with the closed-loop measured controlled (combined filters) transfer function (red) overlaid on top using combined filters for control.

Figure 3.7, is 2.8 dB for P_1, 2.0 dB for the P_2, and 1.9 dB for P_3. At this point the use of McEver's algorithm and Goh's equations are abandoned because they are derived assuming the dynamics of the control filter to be only the PPF filter which has two poles. The combined filter has 10 poles and 6 zeros. The parameters used to obtain good closed-loop performance of just the PPF portion of the combined filter are substantially different from the PPF filter parameters using McEver's algorithm and Goh's equations. The complexity of the combined filter made a mathematical model difficult to obtain. Therefore, simulations and experiments are used to create a new algorithm for setting the combined filters to provide good closed-loop performance with the ability to easily retune the system to obtain near optimal performance.

3.3.2 Combined Filter Parameter Algorithm

Experiments changing the parameters of the combined filter and analyzing the controlled results produce basic guidelines for setting the filter parameters. The band pass is set around the mode of interest by setting the high-pass Butterworth filter cutoff frequency to the zero preceding the mode of interest and setting the low-pass Butterworth filter cutoff frequency to the zero following the mode of interest. The damping ratio of the PPF filter needs to be set to a low value (usually less than 0.15). The PPF filter frequency is found to produce good closed loop results with the frequency set near the zero trailing the mode of interest. The gains should be set with a top/down approach where the gain for the highest mode of interest is incrementally decreased, since a negative gain is needed, until good closed-loop results are measured. Then the gain for the next highest mode is set and so forth. Once all the parameters are selected, the final closed-loop transfer function can be measured. Once the gains are set, the frequency and damping ratios can be fine tuned following a bottom/up routine, starting at the lowest mode of interest.

To summarize the algorithm parameter selection routine:

1) Measure broadband transfer function from control actuator.
2) Set PPF filters damping ratio to small value ($\zeta < 0.15$)
3) Set PPF filter frequency and high pass Butterworth cutoff frequency to the zero following the mode of interest.

4) Set low pass Butterworth cutoff frequency to the zero preceding the mode of interest.
5) Use a top/down approach to set the gains for the individual modal filters.
6) Use a bottom/up approach to fine tune frequency and damping ratio parameters for better performance.

3.3.3 Closed-Loop Simulations using Uncontrolled Measured Data

The main focus of this research is to make an adaptive controller for a payload fairing. Since modeling the payload fairing is not a part of this research, another way of simulating the closed-loop response of the system is needed. At this point, only the model is used to simulate controlled results, but without a model the only thing available that could characterize the system is the measured data. Therefore the measured collocated transfer function (P_1/V_i) is used to simulate the closed-loop response given a control compensator (K_t). The closed-loop response is simulated by replacing the model of the collocated system (G) from Equation 2.29 with the collocated measured transfer function (P_1/V_i). The expression for the simulated closed-loop response becomes a function of frequency and is

$$H_1(\omega) = \frac{(P_1/V_i)(\omega)}{1-(P_1/V_i)(\omega)K_t(\omega)}. \tag{3.12}$$

The results at the P_2 and P_3 are found by the following equations

$$H_2(\omega) = H_1(\omega)G_1(\omega) \tag{3.13}$$

$$H_3(\omega) = H_1(\omega)G_2(\omega), \tag{3.14}$$

both repeated from Equation 2.30 and 2.31 as function of frequency, where G_1 is now P_2/V_i and G_2 is now P_3/V_i. Equation 3.12 is used to simulate the control results of Figure 3.7 using the filter properties as defined in Table 3.1 to formulate K_t. The results of the closed-loop simulated system compared to the measured controlled and uncontrolled transfer functions are seen in Figure 3.8. The simulated results produce good approximations of the actual controlled system in multiple tests using the cylindrical duct and the fairing that are not mentioned here. Closed-loop simulation is needed in order to automate the filter parameter selection and assisted in creating the combined filter algorithm. The abscissa of this transfer function shows the frequency from 0 to 1000 Hz

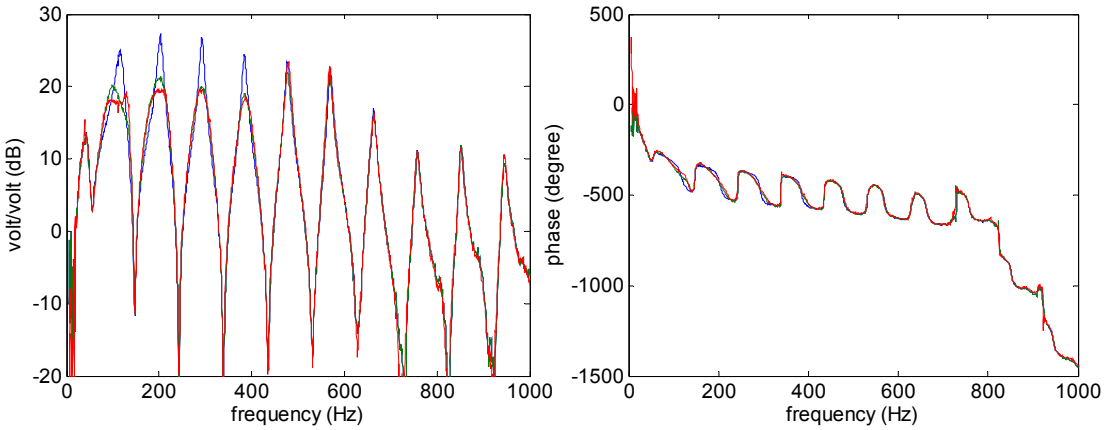

Figure 3.8. Measured collocated transfer function (blue) of the duct overlaid by the measured controlled transfer function (red) and the closed-loop data model transfer function (green).

to show that the controller did not introduce magnitude amplifications at higher frequencies.

3.3.4 Automated Code for Setting Combined Compensator

The combined filter algorithm and Equation 3.12 are used to create an automated code that sets the combined filter parameters. The code requires the measured collocated transfer function (P_1/V_i) from the control actuator. This measurement is analyzed to find the zeros of the system from the magnitude plot of the transfer function. The code sets the filter damping ratios to a user defined value, usually set for $\zeta = 0.08$ for control applied to the duct. The frequencies of the combined filters are set according to the algorithm from the extracted zeros of the data. Next the gains are set with the top/down approach. An optimization routine is used in order to quickly simulate the maximum gain, since the gains needed to be negative, where the system would go unstable using the simulated closed-loop response of the data. The code monitors the simulated closed-loop phase of the system as the gain for one modal filter is changed in the optimization routine and compares the phase from the measured data with the phase of the simulated closed-loop system. The code looks for a substantial phase change in the closed-loop simulation where the phase of a pole acts like the phase of a zero. This phase shift indicates instability because the phase of a pole crossing into the right half of the s-plane increases by 90 degrees indicating an unstable system. Figure 3.9 shows an example of this phase change that the code searches for.

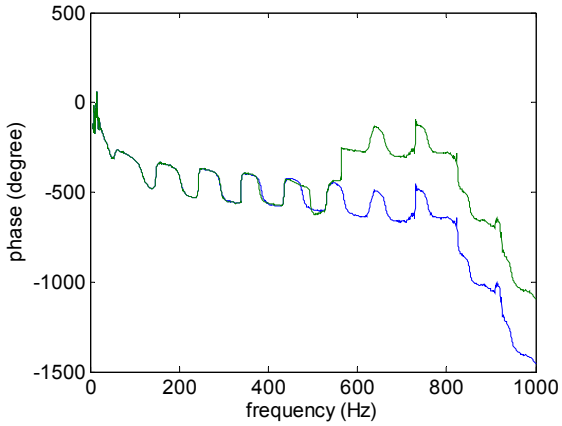

Figure 3.9. Measured collocated phase (blue) overlaid by the simulated closed-loop phase (green) of an unstable system.

Once the simulated results find the maximum gain value, where the simulated result does not indicate instability, the gain is reduced by 20 percent and the optimization routine finds the gain for the next modal filter in the same approach. Once the gains are found, a simulated closed-loop response is plotted, similar to Figure 3.8. The results of the simulated controller can then be visually analyzed by looking at the reductions in the transfer function magnitude and the parameters can be retuned by the control designer in the simulation code, depending on where additional damping is needed. The system can be re-simulated to view the tuned parameter changes on the closed-loop system. A copy of the code used for the cylindrical duct can be found in Appendix E.

3.4 Fairing Control

A schematic of the payload fairing system used in this research can be seen in Figure 3.10. The shell is made from sheet metal riveted together with an external support

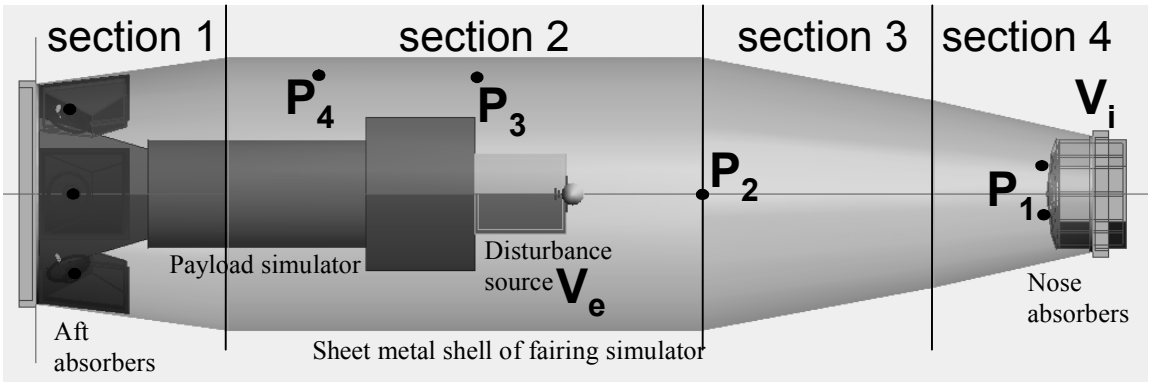

Figure 3.10. Schematic of the side view of the payload fairing.

structure made from wood supporting the shell. The fairing is 233 inches long where section 1 is 42.5 inches long and gradually increases up from a 48.6 inch diameter to a 60.3 inch diameter. Section 2 maintains the 60.3 inch diameter and is 104.4 inches long. Section 3 is 51.3 inches long and tapers down to a 41.2 inch diameter. Section 4 is 34.8 inches long and tapers down from a 41.2 inch diameter to a 25.6 inch diameter. As the figure shows, a simulated payload, about 100 inches long, is inserted into the fairing as well as two sets of control absorbers in the aft and nose of the fairing. The simulated payload is made out of a metal barrel with a large plywood box attached to the barrel in the center of the fairing.

A disturbance source is placed in front of the simulated payload with the speaker facing the nose absorbers. PCB microphones are placed at various locations within the fairing to monitor the SPL and provide signals for feedback control. A total of six microphones are placed within the fairing. Three are placed with one in front of each of the three speakers in the nose of the fairing (defined as P_1 with the sensitivities defined in the next paragraph). One microphone is placed two feet in front of the disturbance source (defined as P_2 with a microphone sensitivity of 37.8 mV/Pa), and two more are place in locations behind the disturbance source along the simulated payload fairing (defined as P_3 with a microphone sensitivity of 31.9 mV/Pa and P_4 with a microphone sensitivity of 45.2 mV/Pa).

Figure 3.11 shows a schematic of the fairing by looking up from the aft absorbers to the nose absorbers in order to see the shape of the three control speakers in the nose. The majority of this research focuses on control of the nose speakers because they

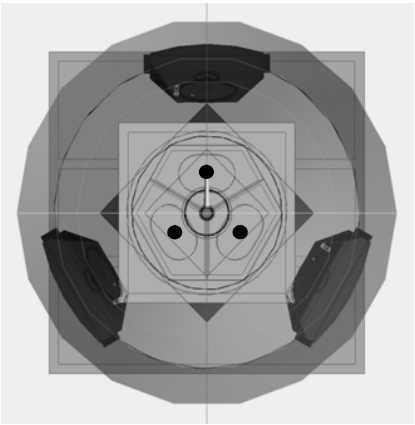

Figure 3.11. Schematic of the bottom of the fairing looking up at the nose absorbers.

provide more control authority over the system then the aft speaker and only results from the nose actuators are presented. The three speakers placed in the nose are three Alpine 6”x9” speakers (model SPR-69LP) inserted in speaker boxes made from medium density fiberboard (MDF). The collocated microphones are placed directly in front of the speakers and have sensitivities of 45.9 mV/Pa, 44.7 mV/Pa, and 37.4 mV/Pa. Two Zetex audio amplifiers (model ZXCD1000 class D), with two input and two output channels each, are used to power the speakers. The amplifiers have a relatively flat magnitude response and the phase only drops by a couple degrees every 500 Hz.

3.4.1 Baseline Fairing Measurements

The collocated transfer function (P_1/V_i) of the fairing is more complex than the collocated transfer function of the cylindrical duct because the fairing is a larger system and the geometry is more complex. The collocated transfer function is measured with the same Siglab unit used to measure the transfer functions of the duct. Figure 3.12 shows the Simulink block diagram that is used to code dSpace to assist in measuring P_1/V_i for the system with and without control. The P_1 measurement is the averaged time data of the three collocated microphones.

The averaged collocated fairing transfer function (P_1/V_i) is shown in Figure 3.13. The transfer function shows where the pole frequencies of the system are by the peaks of the transfer functions. Between 0 and 325 Hz every pole is followed by a zero as seen in the magnitude and phase plots where the magnitude decreases and the phase increases

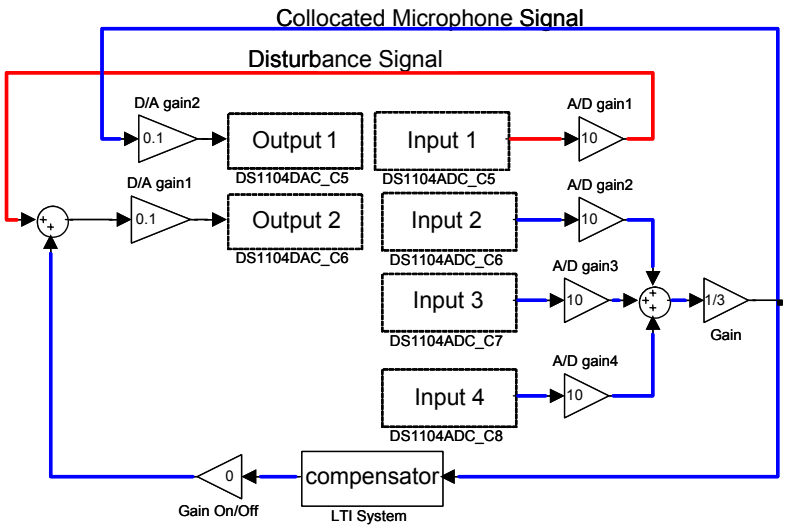

Figure 3.12. Simulink block diagram showing the collocated microphone (blue) and disturbance (red) signals used for the fairing measurements and control.

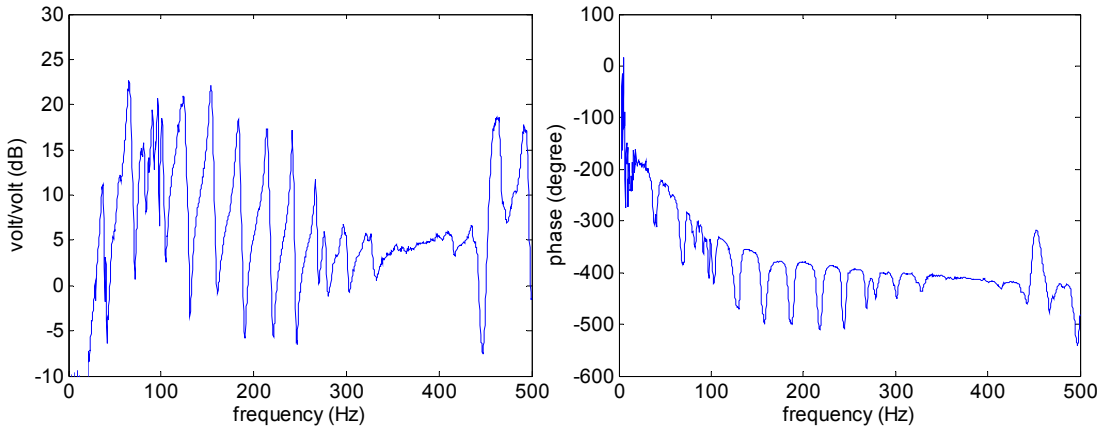

Figure 3.13. Measured collocated transfer function of the payload fairing.

because of the zero. Unlike the transfer function of the duct, the zero frequencies follow very closely to the preceding pole frequencies and get closer at higher frequencies until there is pole/zero cancellation between 325 and 450 Hz. This cancellation is seen in the flat responses of the magnitude and phase plots. At 450 Hz, a zero precedes the pole and causes the phase to increase before a pole brings the phase down. Table 3.2 shows the frequencies of the poles and zeros of the transfer function found from the frequency associated with the maximum magnitude values of the peaks and the minimum magnitude values between the peaks respectively. Over the range of 72 to 106 Hz the transfer function has several poles and zeros closely spaced together as seen in the magnitude and phase diagram. These closely spaced poles and zeroes are probably caused by the radial modes of the system. The reported pole frequency over the 72 to 106 Hz range is the frequency associated with the maximum magnitude value in that range since the poles and zeros are so closely aligned. The phase drop at low frequency is probably caused by the amplifier as seen and explained previously with the phase drop in the duct. The magnitude response of the P_2/V_i and P_3/V_i transfer functions of the fairing, as defined in Figure 3.10, can be seen in Appendix C.

The pole/zero cancellation in the 325 to 450 Hz range is caused by the proximity of the three collocated microphones to the speakers. This cause is determined by analyzing the transfer functions of each collocated microphone as the disturbance signal

Table 3.2. Fairing pole and zero frequency location of the first 9 modes.

modes	1	2	3	4	5	6	7	8	9
pole (Hz)	36.9	65.6	96.6	124	154	183	214	242	267
zero (Hz)	41.9	72.2	106	131	161	190	221	247	271

is sent to each individual speaker. These transfer function plots can be seen in Appendix C. The figures show how the collocated transfer functions for each particular speaker are different than the transfer functions for the other two microphone locations. The frequency locations of the zeros and the magnitude values of the zeros are different. These differences are the result of the near field effects of the speakers with the proximity of the microphones.

3.4.2 Control of the Fairing Simulator

The averaged collocated transfer function of the fairing is used to design a controller for the fairing using the combined filters and proportional feedback. Control simulations and experiments show that for this particular system, setting the proportional feedback gain to -0.15 produces good closed-loop results and maintains stability. The proportional feedback controller adds substantial damping to the lower modes. The automated combined compensator code is used to identify and set the combined filters for 7 modes in the fairing (modes 3 through 9) with the addition of the proportional feedback included in the compensator. The control parameters found with the automated code are in Table 3.3. Once the transfer function of the filters for each mode is designed, the filters are summed together to form one feedback compensator transfer function (K_t) and the block diagram from Figure 3.12 is used to create the control code for the dSpace processor. When control is implemented the On/Off gain is slowly increased during the experiments to insure stability in the system during control experiments. No additional modes are controlled because additional filters for higher modes cause the order of the total compensator to increase and numerical limitations of the dSpace processor with the total compensator causes the system to stop working.

The measured collocated closed-loop transfer function (P_l/V_i) obtained using the control parameters from Table 3.3 is shown in Figure 3.14. Again, as with the duct control, the disturbance signal and the controlled signal are overlaid on the same actuator

Table 3.3. Controller parameters for each combined filter for modes 3 through 9 of the fairing.

modes	3	4	5	6	7	8	9
gain	-0.1251	-0.1251	-0.2477	-0.2143	-0.1416	-0.1203	-0.2339
PPF frequency	127.5	127.5	156.3	184.8	214.8	239.6	262.6
PPF damping	0.08	0.08	0.08	0.08	0.08	0.08	0.08
H-pass Butterworth	105.6	105.6	131.3	160.9	190.3	221.3	246.9
L-pass Butterworth	131.3	131.3	160.9	190.3	221.3	246.9	270.6

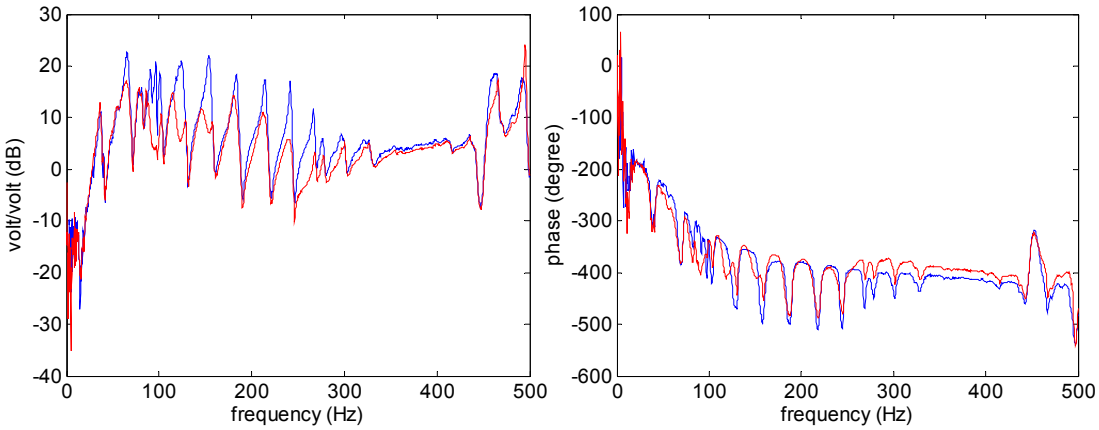

Figure 3.14. Measured collocated location transfer function (blue) of the fairing with the measured closed-loop controlled transfer function (red) overlaid on top.

as the block diagram of Figure 3.12 indicates. The disturbance signal is maintained at 0.05 volts (RMS) from the Siglab unit and the transfer functions and autospectrum data are recorded for 5 averages, with the use of a Hanning window and 4096 data points taken for each average. The average SPL reduction from 50 to 250 Hz at P_1 is 4.4 dB. The magnitudes of the transfer functions for (P_2/V_i) and (P_4/V_i) within the fairing can be seen in Appendix C and the SPL reduction from 50 to 250 Hz is 4.0 and 4.2 dB respectively. The SPL reductions are calculated from Equations 3.2 and 3.3 as previously explained.

3.5 Control for an External Excitation

The previous results for the duct and the fairing show that SPL reduction can be achieved using the combined filters. The previous results are not practical for a real world application because the disturbance will not come from the actuator that is used for control. Therefore, the controllers designed in the previous sections are used when the system is excited by a different actuator (V_e) in or by the system.

3.5.1 Duct External Disturbance

Two Optimus 4 ohm speaker systems (Cat No:12-1713) are used to excite the internal acoustic environment of the cylindrical duct. These two speaker systems are placed on the same side of the duct, facing the side of the duct as shown in Figure 2.5. One speaker system is about 2 feet away from the control speaker and the other is about 4 feet way from the control speaker. The controller previously designed for the duct with

the combined filters is used with these external speakers exciting the system. The block diagram from Figure 3.1 is used except the disturbance signal is sent to the Optimus speakers instead of added to the control signal and sent to the control speaker. The Siglab unit is used to measure the signals from the disturbance signal (V_e) and the microphone measurements. The magnitudes of the P_1/V_e, P_2/V_e, and P_3/V_e transfer functions are shown in Figure 3.15. All three figures show that additional damping is added to the system by the decrease in the magnitude peaks. The SPL reductions are 2.4, 1.7, and 1.7dB for P_1, P_2, and P_3 measurements respectively. As before, these reductions are calculated from the autospectrum response of the microphone measurements at the specified locations.

3.5.2 Fairing Disturbance Excitation

As previously stated, the fairing system has an additional speaker placed within the fairing as shown in the schematic in Figure 3.10. The fairing compensator previously designed is used with the nose absorbers while the disturbance signal is sent to the

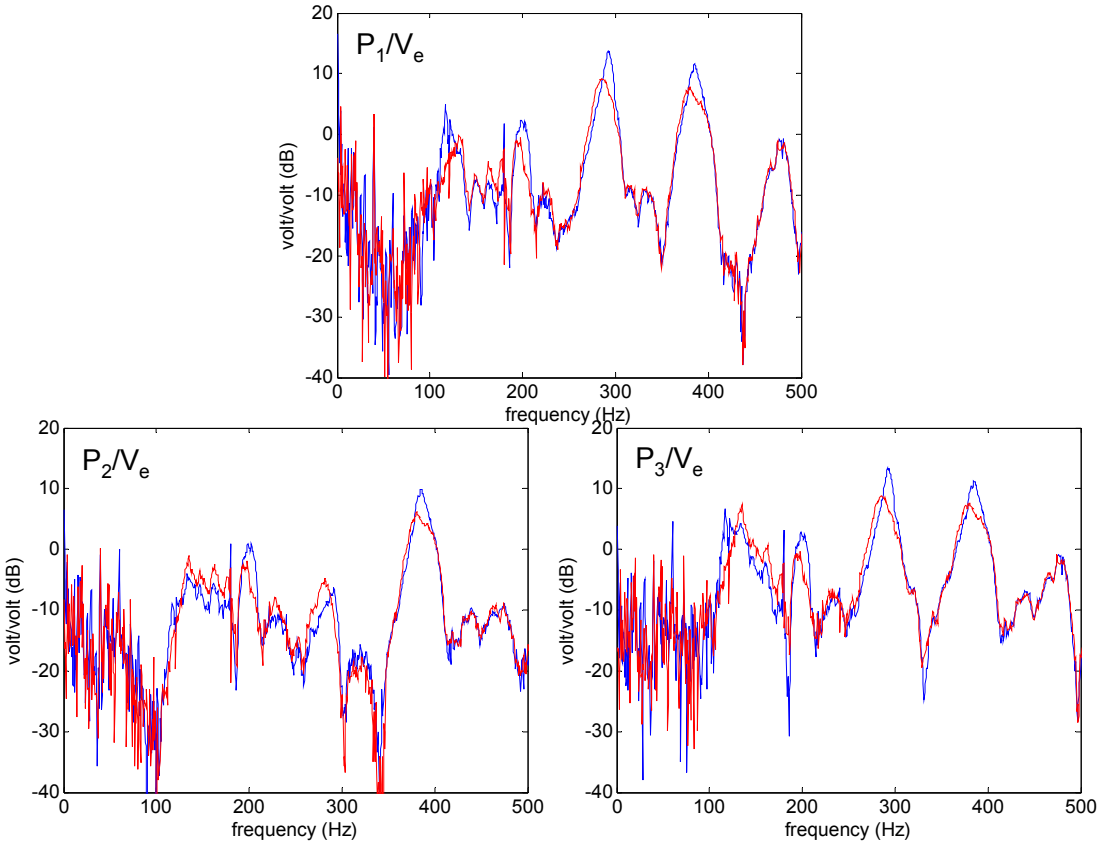

Figure 3.15. Measured transfer function magnitudes of the microphone measurements over the disturbance input for the three measurement locations of the cylindrical duct.

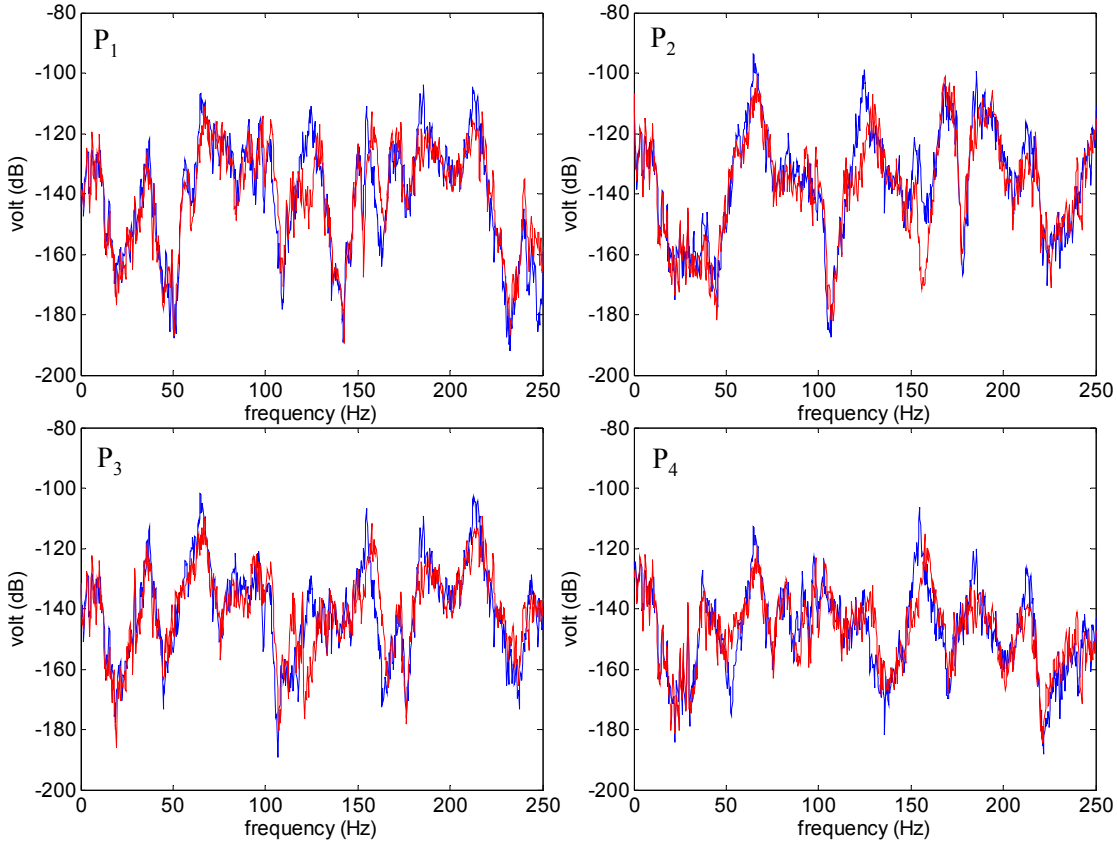

Figure 3.16. Measured autospectrum data of the fairing with the measurement location in the top left corner of each plot.

disturbance source. The results are measured at the four measurement locations as previously defined in Figure 3.10. The SPL reductions are 1.5 dB, 1.5 dB, 2.0 dB, and 1.9 dB for P_1, P_2, P_3, and P_4 respectively over the 50 to 250 Hz frequency range which is the frequency range where control is added. Figure 3.16 shows the baseline autospectrum response of these four microphone locations with the closed-loop controlled autospectrum response overlaid on top. Each measurement shows how the peak responses are reduced when the control is added to the system.

3.6 Chapter Summary

In this chapter PPF closed-loop control results from McEver's algorithm and Goh's equations are presented. Also observed and discussed is the low frequency spill-over that causes magnitude increases at lower modes when multiple PPF filters are applied, as the model showed and the literature stated. High- and low-pass Butterworth

filters are shown to be useful in effectively eliminating the majority of this low frequency spill-over. A new algorithm is presented for setting the combined filter parameters. Control results for the cylindrical duct and the fairing are presented that showed SPL reduction in both test scenarios: (1) the overlaid disturbance and control signals on one actuator and (2) the separate disturbance and control signals on separate actuators. The next chapter will look at the robustness of the controller with changes in the system and introduce an adaptive controller for system changes.

Chapter 4

Adaptive Control

4.1 Introduction

The previous chapter presents how positive position feedback (PPF) control, when used in conjunction with high- and low-pass Butterworth filters, is effective at absorbing energy in an acoustic enclosure. Control results with acoustic excitation in the cylindrical duct and in the fairing show that the internal sound pressure level (SPL) is reduced using collocated feedback. Once the controller is shown to work on both systems, the work shifts to analyzing the robustness of the controller to system changes and designing an adaptive controller to maintain the SPL reduction as the changes occur. Changes that are made to the geometry of the fairing, payload, and cylindrical duct are implemented with the intent to change the internal acoustic characteristics of each system and are presented in this chapter. The duct geometry is easily modified as will be explained, thereby changing the acoustic characteristics. The fairing geometry is difficult to change because the size and complexity of the geometry makes boundary changes difficult to implement. This chapter will present the robustness of the non-adaptive controller to changes in the cylindrical duct and will present an adaptive controller used for updating the control compensator in order to maintain SPL reduction despite system changes. This adaptive controller is shown to reduce the SPL of the cylindrical duct with 20 percent changes in the acoustic modes' frequencies of the duct where these changes cause the closed-loop non-adaptive controlled system to go unstable.

4.2 Controller Robustness Tests

The design of the combined filters, described in the previous chapter, is to add damping to the acoustic modes of the enclosure. Changes in the frequency location of these modes may compromise the effectiveness of the compensator to actively damp the modes and, depending on the degree of the change, may cause the system to go unstable. Changes in the acoustic characteristics of the enclosures are influenced by geometric and boundary changes therefore, changes in the boundaries are used to change the internal acoustic characteristics for testing controller robustness.

4.2.1 Attempted Fairing Robustness Test

Payload fairings come in slightly different shapes and many different sizes as shown in Figure 1.2. The previous chapter shows how a collocated transfer function from the absorber actuators in the nose can be used to design a non-adaptive controller for energy absorption within the fairing for SPL reduction at low frequency. One issue that is excluded from that discussion and design is potential changes in the acoustic environment. Different size payloads and launch conditions can change the acoustic environment inside the fairing and detune an active controller. This work is not meant to study all the potential changes and quantify them, but to realize that changes may occur and design a controller that can accommodate for these changes.

Changing the simulated payload in the fairing is impractical because of the size and the way the payload and fairing are constructed. The payload is made from a metal drum with a large plywood box attached to the end. The payload is bolted to the aft end cap and held in place in the fairing with wire attached to the side of the fairing and can not be easily extracted. One suggestion for changing the size of the payload was to add hinged arms to the side of the payload, without removing the payload, that would lay flat against the payload (maintaining close to the current geometry) and could be opened during control testing changing the geometry of the payload. Before this design was constructed and implemented, flat panels were inserted into the fairing along side the payload in the manner and location in which the hinged arms were to be set. The transfer functions were measured and the frequencies of the acoustic modes shifted by less than 1 percent. The panels did add some noticeable damping to some of the modes when the transfer functions were analyzed but modal frequency shifting was the intent of the

design. The next suggestion was to remove the nose cap and nose absorbers of the fairing during experiments using the aft absorbers for control. The largest change observed was 5 Hz in the highest mode of interest for control, shifting the modal frequencies by less than 2 percent. Therefore, no actual testing has been performed on the robustness of the controller within the fairing because its size and complex geometry made changing the acoustic properties difficult, within the time allotted for this research.

4.2.2 Cylindrical Duct Robustness Test

The cylindrical duct is easily designed to incorporate changes in the geometry, where the geometric changes cause large changes in the acoustic characteristics of the enclosure. Figure 4.1 is a picture of the end cap design of the duct. The end cap is made like a piston cylinder device where the end cap fits inside the duct and the connecting rod of the piston is used to change the length of the cylindrical duct and the interior acoustic characteristics. Table 4.1 shows the pole and zero frequencies and damping ratios associated with each of the first 6 modes for a cylindrical duct length of 72 inches, and for a duct length of 60 inches. Below these measured values, the table shows the percent change in the pole and zero frequencies and the damping ratios for the different duct lengths. This data shows that a duct length change of 17 percent will cause the pole and zero frequencies to change by more than 20 percent, excluding the first pole and zero. The first pole and zero did not shift like the other poles and zeros because of its coupling with the speaker resonance.

Table 4.1. Measured pole and zero frequencies values and damping ratios for the first six modes of the duct at a length of 72 inches and 60 inches.

72 inch cylindrical duct						
poles (Hz)	43.8	115.6	203.1	292.5	383.8	476.9
damping ratio	0.15	0.06	0.02	0.01	0.01	0.01
zeros (Hz)	56.3	148.1	243.1	339.4	435.6	531.9
60 inch cylindrical duct						
poles (Hz)	39.4	142.5	243.8	353.1	462.5	573.8
damping ratio	0.16	0.06	0.02	0.01	0.01	0.02
zeros (Hz)	56.3	182.5	297.5	413.1	528.1	647.5
Change (percentage)						
poles (Hz)	-10.0	23.2	20.0	20.7	20.5	20.3
damping ratio	5.8	-1.2	13.1	10.4	-10.1	197.8
zeros (Hz)	0	23.2	22.4	21.7	21.2	21.7

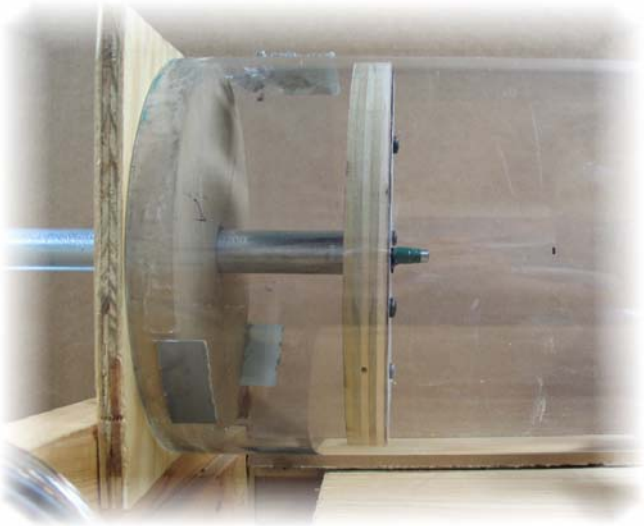

Figure 4.1. Photograph of the end cap piston design.

The non-adaptive controller designed in the previous chapter for the duct length at 72 inches is used for the robustness testing. The length of the duct is changed in one inch decrements for measuring the robustness of the non-adaptive controller. The control parameters are maintained at the values shown in Table 3.1 of the previous chapter. Table 4.2 shows the SPL reduction as the length of the duct is reduced where the disturbance signal is overlaid on the control actuator (defined as V_i in figure 2.5). The reported SPL reduction is the average SPL reduction of the P_1, P_2, and P_3 measurements. After a 4 percent duct length change, the controller starts to increase the SPL in the duct and the system goes unstable after a 10 percent duct length change. The 10 percent length change is equivalent to an 8 percent change in the modes' frequencies. Figure 4.2 shows the measured collocated magnitude of the transfer functions (P_1/V_i) of the duct as the length is changed by 2 inch decrements for the controlled and uncontrolled cases. A series of figures showing the transfer functions of the duct with changes in inch decrements for the P_1/V_i, P_2/V_i, and P_3/V_i transfer functions can be seen in Appendix D. The values from Table 4.2 and measurements from Figure 4.2 show that any appreciable change in the duct length will require the control parameters to be retuned or adapted for continued SPL reduction.

Table 4.2. Non-adaptive control SPL reduction as the length of the duct is shortened.

length (inches)	72	71	70	69	68	67	66
SPL (dB)	2.2	1.6	0.6	0.0	-1.6	-2.6	-10.2

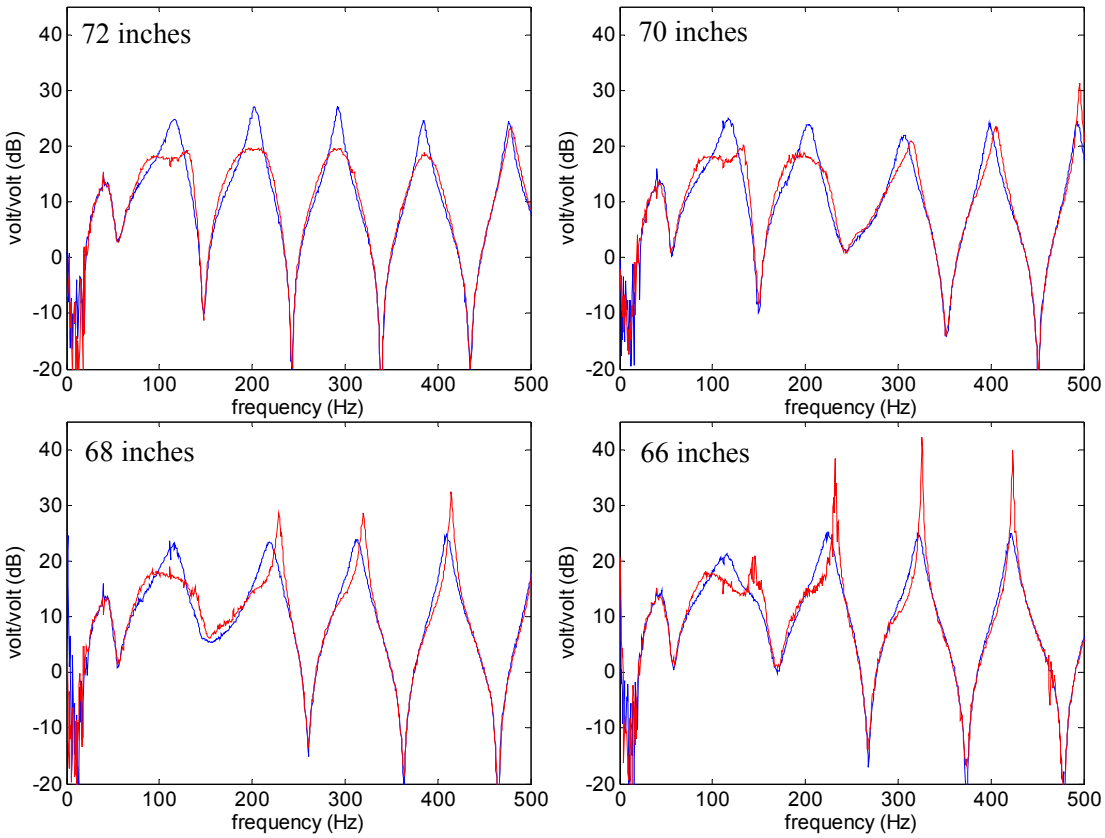

Figure 4.2. Measured collocated magnitude results of the transfer functions (blue) of the duct with the closed-loop measured non-adaptive controlled magnitude results of the transfer functions (red) overlaid on top for 2 inch decrement changes in the duct length.

The same non-adaptive controller is also used with an external disturbance (defined as V_e in figure 2.5) exciting the duct as the length is changed. The system goes unstable after an 11 percent change in the length of the duct and a 9 percent change in the frequencies of the modes. The controller performs well with length changes of less than 5 percent as can be seen in the SPL reductions of Table 4.3. Again, these SPL reductions are the average SPL reduction of the P_1, P_2, and P_3 measurements. SPL reductions are maintained at close to 2 dB or higher for duct length reductions of less than 5 percent which coincides with a length change of 4 inches. Figure 4.3 shows the measured collocated transfer functions (P_1/V_e) as the duct length is decreased by 2 inch decrements. As before, a series of transfer functions can be seen in Appendix D that show the results

Table 4.3. Non-adaptive control SPL reduction as the length of the duct is shortened with an external disturbance.

length (inches)	72	71	70	69	68	67	66	65
SPL (dB)	1.9	1.5	3.0	2.1	2.3	0.0	-2.9	-9.6

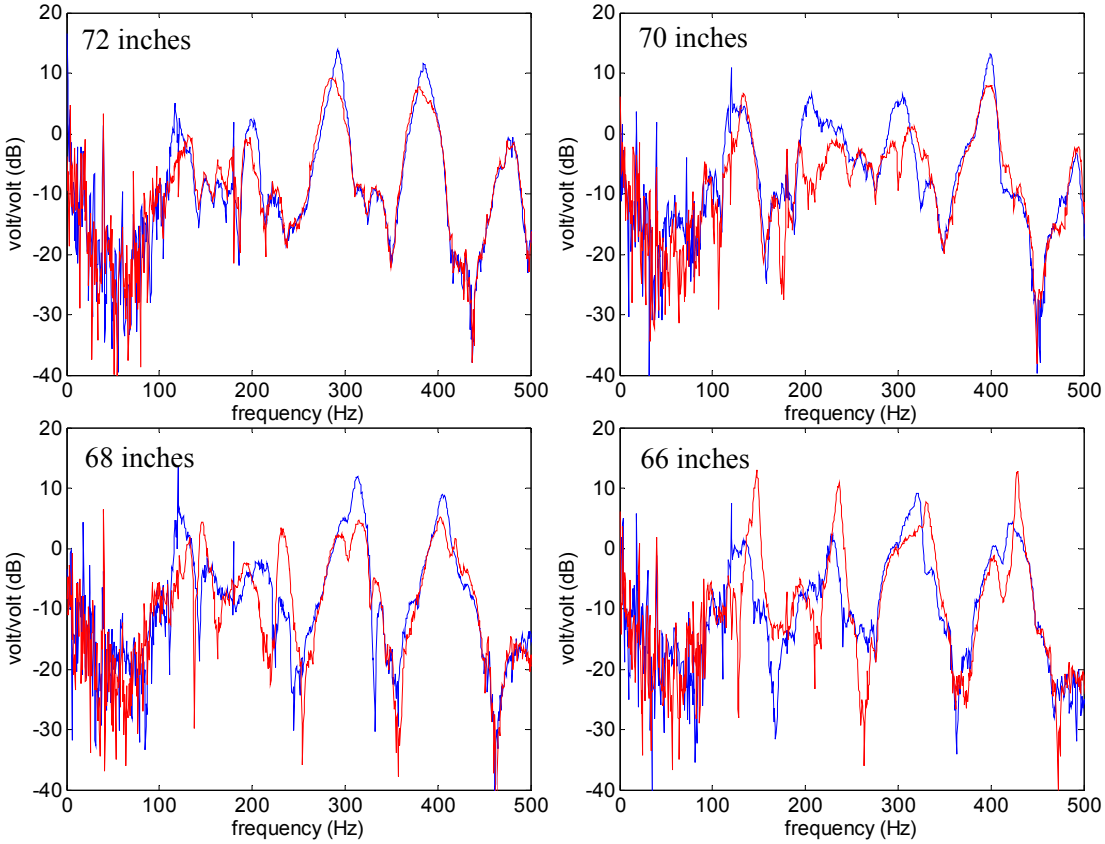

Figure 4.3. Measured collocated magnitude results of the transfer functions (blue) of the duct with the closed-loop measured non-adaptive controlled magnitude results of the transfer functions (red) overlaid on top for 2 inch decrement changes in the duct length.

as the duct length is decreased by one inch decrements for the P_1/V_e, P_2/V_e, and P_3/V_e transfer functions.

These cylindrical duct results show that large changes in the system will cause instability with feedback control. The robustness of the controller on the fairing has not been tested because of difficulty in changing the frequency values of the acoustic modes of the system. This inability to easily change the acoustic modes does not imply that the frequencies of the acoustic modes of a fairing will not change. Therefore an adaptive controller will be beneficial and could prevent instabilities that will happen if a non-adaptive controller is used and large changes do occur.

4.3 Adaptive Control Design

As explained in Chapter 1 by Anderson (2005), an adaptive controller is needed when the plant or system is time varying. In this research, the plant varies as the

geometry of the system varies, causing the acoustic characteristics to be time variant depending on the time variance of the geometry. Therefore, an adaptive controller is needed to eliminate the instability seen previously with the non-adaptive controller with geometric changes of the enclosure. The block diagram from Figure 1.4 is adjusted for this research and Figure 4.4 shows this adjusted block diagram. The adaptive controller is designed to use the previously presented combined filter algorithm to update the compensator for any changes in the system by following the collocated zero frequency changes.

The basic architecture of the parameter adjustment block from Figure 4.4 is as follows. The time data of the collocated microphone is buffered for 2048 points and used to calculate a fast fourier transform (FFT) of the data to obtain frequency characteristics of the system. The FFT is performed approximately every 0.4 seconds during the control with a controller sample rate of 5000 Hz. Due to limitations of the processor, the transfer function is not measured because the processor is unable to perform two FFT calculations while sampling at this rate. Therefore the collocated FFT is used to extract the zero frequencies of the system. The zero frequency values are then buffered for each zero location and averaged with previously found zeros. Since adaptation speed is currently not a priority, twenty zeros are buffered for each zero frequency and averaged using a moving average, but the total time for completely updating the controller, to system changes is approximately 8 seconds. No accommodations for rate changes or step changes in the system characteristics are included in the adaptive controller at this point.

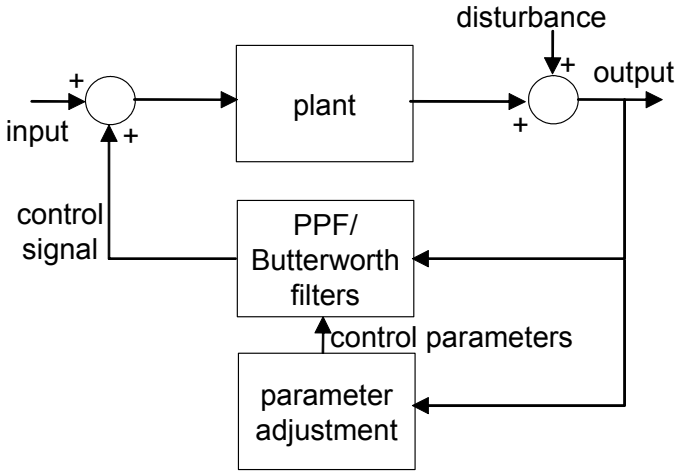

Figure 4.4. Block diagram of the adaptive feedback controller used in this research.

The damping ratios of the PPF filters are maintained constant and the gains are maintained constant from the initial identification of the controller as explained in the previous chapter and found with the automated combined filter code. The actual Simulink block diagram and code for the above parameter adjustment block can be seen in Appendix E.

4.4 Adaptive Control Results

The cylindrical duct is used to test the adaptive controller. The first set of testing is performed with the disturbance signal and the control signal overlaid on the same actuator. Figure 4.5 shows the Simulink block diagram modified from Figure 3.1 to include the parameter adjustment block for changing the compensator. The parameter adjustment block finds the frequencies of the zeros and uses the combined filter algorithm to set the total compensator. Therefore, any changes in the system will be tracked by the FFT and the compensator will be adapted accordingly.

The controller is initially set for the duct length of 72 inches and the damping and gains for the non-adaptive controller of this length are maintained constant for the adaptive controller. First, the disturbance signal is applied and then the controller is turned on by increasing the On/Off gain from 0 to 1 in increments of 0.01. Once the

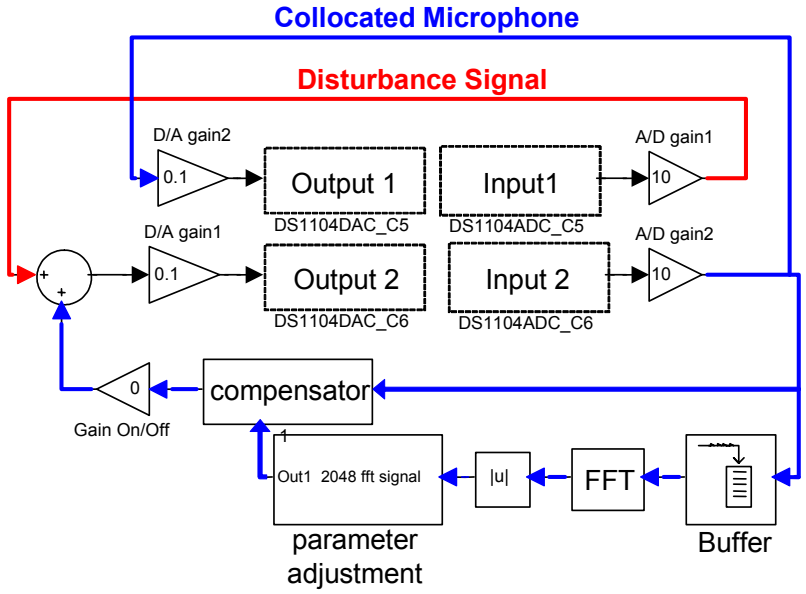

Figure 4.5. Simulink block diagram showing the collocated microphone (blue) and disturbance (red) signals with the compensator in the feedback loop of the microphone signal and the parameter adjustment block setting the compensator parameters.

On/Off gain is set to 1, the length of the duct is reduced in 1-inch decrements until the duct is 60 inches in length. The transfer functions (P_1/V_i, P_2/V_i, and P_3/V_i) are measured at every increment. Figure 4.6 shows the closed-loop magnitude response of the collocated transfer functions (P_1/V_i) using the adaptive controller (in black), the non-adaptive controller (in red until the system is unstable), and the baseline measurements

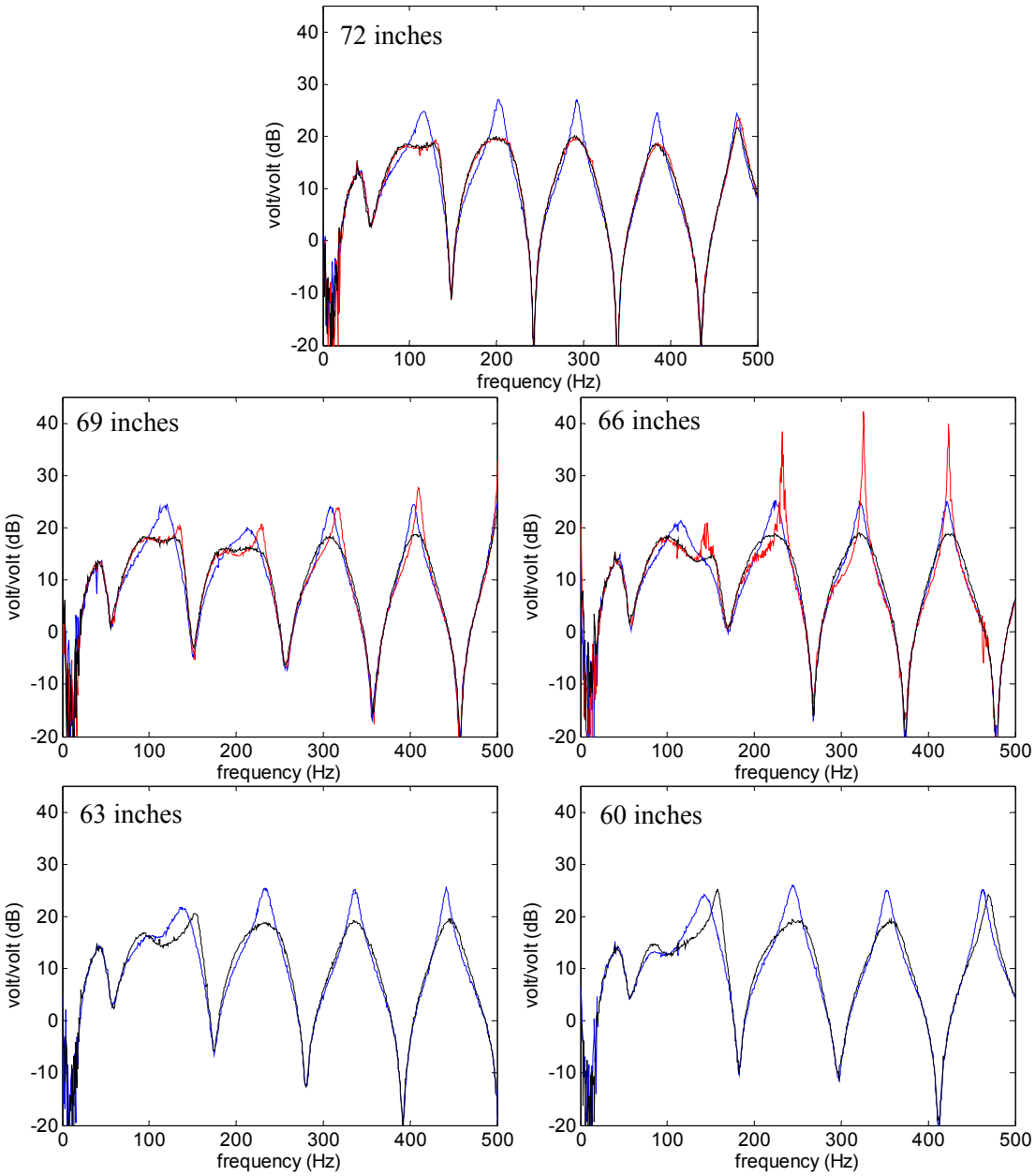

Figure 4.6. Measured collocated transfer functions (blue) of the duct with the measured collocated transfer functions of the non-adaptive controlled results (red) and the adaptive controlled results (black) for 3 inch decrements in duct length. The non-adaptive controlled results are not shown in the last two plots because the system is unstable.

(in blue) in 3 inch decrements. The plots show that adaptive control reduces the overall magnitude response of the system as the system changes, where non-adaptive control increases the magnitude response and eventually causes the system to go unstable. The adaptive controller maintains stability and continues decreasing the SPL as the duct length changes for the entire 12 inches. The SPL reduction results for each incremental measurement with adaptive control compared to the non-adaptive control are shown in Table 4.4. The reported values show that after a duct length change of 2 inches, less than a 3 percent change in the frequencies of the modes of the system, the non-adaptive controller does not reduce the SPL of the system. All the reductions reported are calculated over a frequency range of 100 to 500 Hz.

The same test described above is repeated with an external excitation (V_e) on the duct. Figure 4.7 shows the closed-loop magnitude response of the transfer functions (P_1/V_e) with an external excitation using the adaptive controller (in black) and the non-adaptive controller (in red) overlaid on the baseline measurements (in blue) in 3 inch decrements. As before, the adaptive controller keeps the system from going unstable and absorbs acoustic energy through the 12 inch change. Table 4.5 quantifies the controller reduction as SPL reduction. The adaptive controller did increase the SPL at the P_3 location of the duct at a 7-inch decrement, but this increase is the only instance recorded when the adaptive control causes an increase in the SPL at any location.

Table 4.4. SPL reductions for the duct using the non-adaptive control and adaptive control with the disturbance signal overlaid with the control signal on the same actuator.

duct length	P_1		P_2		P_3	
	non-adaptive	adaptive	non-adaptive	adaptive	non-adaptive	adaptive
72 inch	2.8	2.8	2.0	2.2	1.9	1.9
71 inch	1.9	2.6	1.4	1.8	1.4	1.7
70 inch	0.8	2.3	0.4	1.2	0.5	1.6
69 inch	0.6	2.1	-0.5	0.9	0.0	1.2
68 inch	-1.2	2.2	-2.3	1.4	-1.3	1.4
67 inch	-2.7	2.7	-2.9	2.2	-2.2	1.8
66 inch	-9.9	2.4	-11.3	1.9	-9.5	1.5
65 inch	unstable	2.6	unstable	1.9	unstable	1.6
64 inch	unstable	1.8	unstable	1.5	unstable	0.8
63 inch	unstable	2.8	unstable	2.4	unstable	1.8
62 inch	unstable	2.3	unstable	2.1	unstable	1.2
61 inch	unstable	2.5	unstable	2.6	unstable	1.2
60 inch	unstable	1.9	unstable	2.1	unstable	1.0

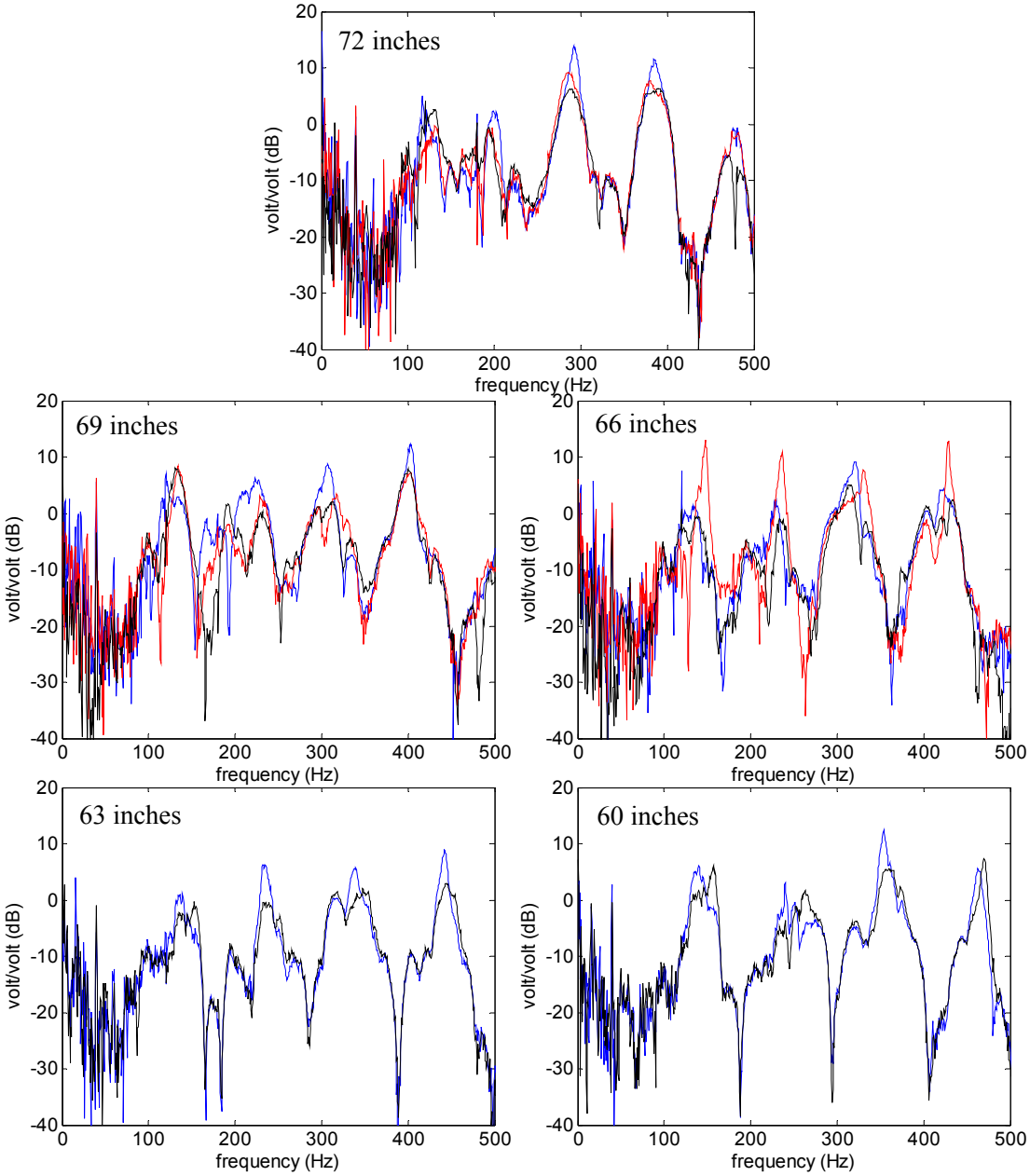

Figure 4.7. Measured collocated transfer functions (blue) of the duct with the measured collocated transfer functions of the non-adaptive controlled results (red) and the adaptive controlled results (black). The non-adaptive controlled results are not shown in the last two plots because the system is unstable.

Figure 4.8 shows the non-dimensional averaged pressure of P_1, P_2, and P_3 in the duct for the non-adaptive control, adaptive control, and baseline cases. The non-dimensional variable is the baseline average pressure of P_1, P_2, and P_3 at each 1-inch decrement and is the black line at 1 in the figure. Any control value below 1 will indicate that energy is absorbed in the duct and the SPL is reduced. Any control value above 1

Table 4.5. SPL reductions for the duct using the non-adaptive control and adaptive control with the disturbance signal sent to an external actuator.

duct change	P_1		P_2		P_3	
	non-adaptive	adaptive	non-adaptive	adaptive	non-adaptive	adaptive
72 inch	2.4	2.7	1.7	2.1	1.7	1.9
71 inch	1.6	1.4	1.6	1.2	1.3	0.9
70 inch	3.6	2.3	3.0	2.3	2.2	1.5
69 inch	2.7	2.4	2.5	2.5	1.1	1.3
68 inch	3.4	2.1	1.3	1.4	2.1	1.4
67 inch	0.8	1.1	-0.4	0.3	-0.4	0.7
66 inch	-2.3	1.5	-3.6	0.4	-2.8	0.7
65 inch	-9.9	0.5	-7.0	0.5	-11.9	-0.1
64 inch	unstable	1.7	unstable	1.4	unstable	0.9
63 inch	unstable	1.9	unstable	1.1	unstable	1.0
62 inch	unstable	1.2	unstable	0.7	unstable	0.6
61 inch	unstable	2.1	unstable	1.8	unstable	1.3
60 inch	unstable	1.4	unstable	1.7	unstable	1.0

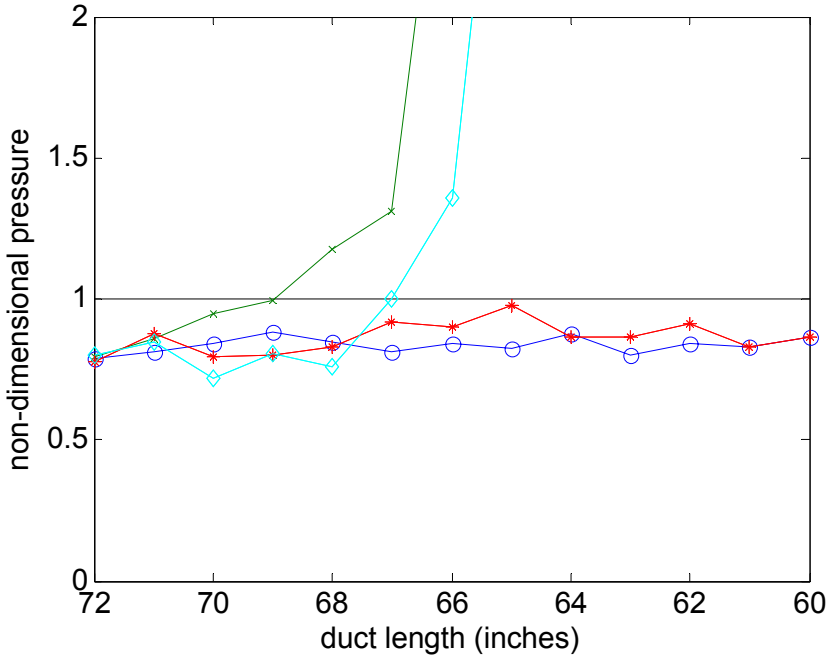

Figure 4.8. Non-dimensional pressure of the duct as the length is decreased. The non-dimensional variable is the baseline pressure without control (black), the non-adaptive control for the excitation from V_i and V_e are green and cyan respectively, and the adaptive control for the excitation from V_i and V_e are blue and red respectively.

will indicate that energy is added to the system and the SPL is increased. The non-dimensional pressure of the non-adaptive control found from the disturbance signals as V_i and V_e are the green and cyan lines respectively. The non-dimensional pressure for the adaptive control found from the disturbance signals as V_i and V_e are the blue and red lines

respectively. This figure shows that the non-adaptive control quickly goes unstable after the length of the duct is changed more then 4 inches while the adaptive control reduces the SPL through the 12-inch change.

Several limitations should be mentioned about this adaptive controller. The dSpace 1104 processor board used for this research causes the majority of the limitations encountered. The number of control filters used is limited because of the numerical precision of the processor. Experiments show that this limitation is a function of how closely spaced the modes are, the frequency of the highest mode being controlled, and the number of modes being controlled. When the numerical precision of the processor is approached, the control signal is occasionally discontinuous and the speaker makes a popping sound. When the precision is significantly surpassed the speaker pops and the dSpace system stops producing a control signal. For this reasons, only five modes of the duct are controlled using the combined filters and only four modes of the fairing are controlled with the addition of the proportional feedback.

As previously stated, the geometry of the fairing makes changing the acoustic characteristics difficult and therefore the adaptive controller is only tested to see that stability is maintained within the fairing and that there is little deviation in the closed-loop performance. The automated combined filter code from Chapter 3 is used to set the gains and damping ratios of each filter for the third through sixth modes of the fairing. Table 4.6 shows the values where the damping ratios and gains are set and the filter frequencies are set by the adaptive controller. Figure 4.9 shows the magnitude within the fairing for the P_1/V_i, P_2/V_i, and P_4/V_i transfer functions as defined in Figure 3.10. Since the control filters are only set up to the sixth mode, the SPL reduction is calculated for the 50 to 200 Hz range. The SPL reduction for P_1, P_2, and P_4 measurements are 4.7 dB, 4.0 dB, and 3.4 dB respectively.

Table 4.6. Controller parameters for the adaptive controller of the fairing.

modes	3	4	5	6	proportional
gain	-0.0702	-0.1221	-0.0585	-0.0237	-0.150
damping ratio	0.12	0.12	0.12	0.12	

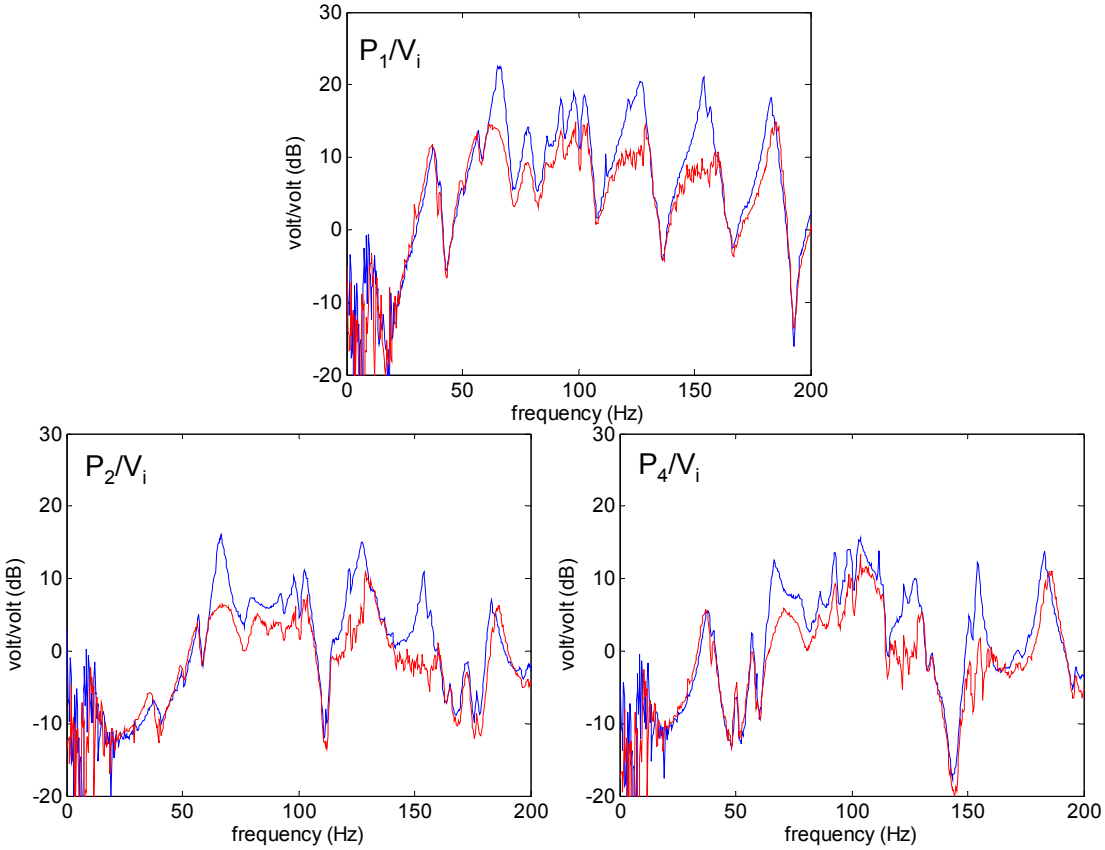

Figure 4.9. Measured transfer functions (blue) of the fairing with the measured transfer functions of the adaptive controlled results (red) overlaid on top.

This same adaptive controller is used with the disturbance sent to the disturbance speaker (V_e) in the payload fairing. Again, the measurement locations in the fairing are the P_1/V_e, P_2/V_e, and P_4/V_e transfer functions. The magnitudes of the transfer functions are shown in Figure 4.10 and the SPL reduction at P_1, P_2, and P_4 are 4.0 dB, 2.3 dB, and 1.6 dB respectively. These values show that SPL reduction is achieved in the fairing. The adaptive code is able to set the combined filter frequencies to values that absorb acoustic energy in the fairing.

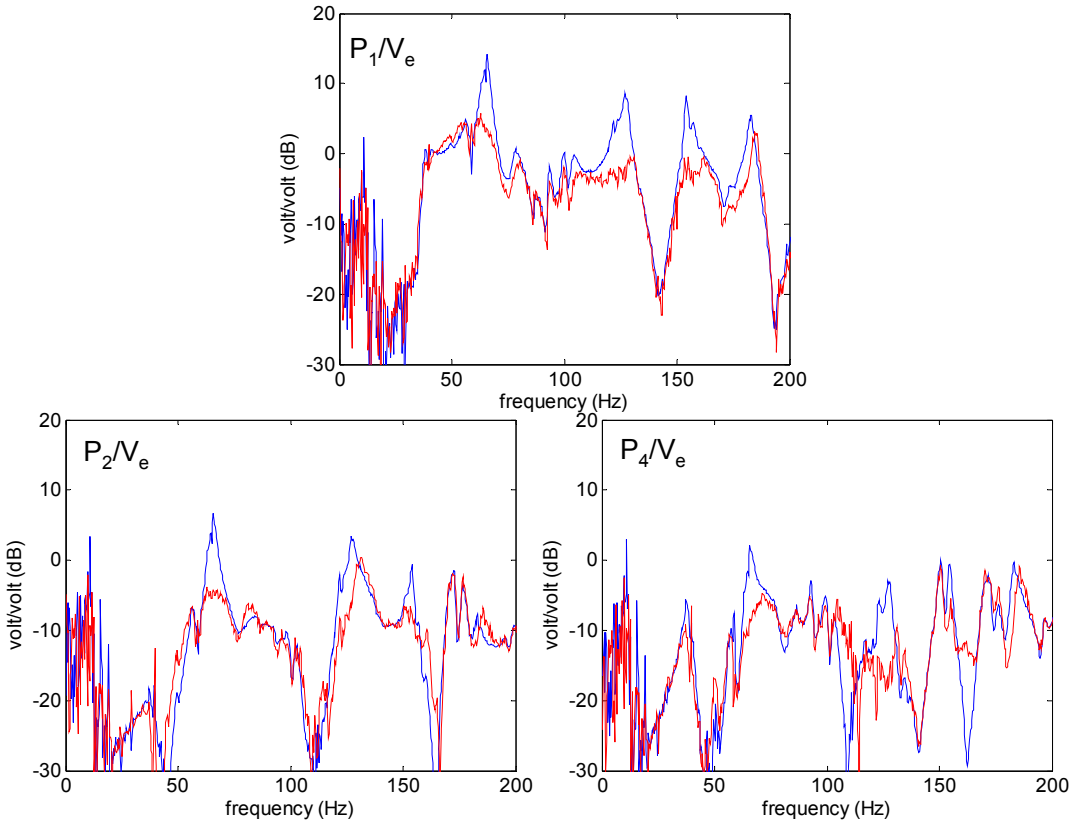

Figure 4.10. Measured transfer functions (blue) of the fairing with the measured transfer functions of the adaptive controlled results (red) overlaid on top.

4.5 Chapter Summary

In this chapter the robustness of the non-adaptive controller is examined. Due to the impracticality of easily changing the fairing, the robustness is only examined in the cylindrical duct by changing the duct length. The results show that small changes in the length, of 5 percent or less, causes the SPL to increase over the levels before control is added and a change of approximately 10 percent causes the system to go unstable. Therefore, an adaptive controller is designed to keep the system stable and reduce the SPL of the system. The adaptive controller is shown to work with the duct for reducing the SPL, with changes in the duct length of 15 percent with the frequencies of the acoustic modes changing by 20 percent. The cylindrical duct results show that the adaptation scheme works, and because the adaptive controller is shown to maintain the same reductions in the fairing as the non-adaptive controller, the adaptive controller should work in the payload fairing, as well.

Chapter 5

Conclusions

The primary object of this work was to demonstrate the use of feedback control for the absorption of acoustic energy inside the interior of launch vehicle payload fairings. The motivation of this work was avoiding added weight of payload designs for structural integrity against high sound pressure levels (SPL) experienced during launch. This primary objective was addressed by reducing SPL with an adaptive feedback controller designed for non-static interior acoustic characteristics due to different geometries and launch conditions. The majority of the research was performed on a cylindrical duct where the boundary condition was altered to change the interior acoustic characteristics for testing the adaptation abilities of the controller. Two dB reduction in the duct was achieved over the 100 to 500 Hz frequency range and positive dB reduction was maintained through a 20 percent modal frequency change. The motivation of launch weight was not addressed in detail in this research and was addressed by a research at the company funding this work. The current design of the controller and absorbers weighs 25 pounds without including the weight of the power supply and wiring. This system achieved a 4 dB reduction in the fairing simulator over the 50 to 250 Hz frequency range. Further work could reduce this weight further as this chapter will summarize the contributions of this work and will present suggestions for continued research.

5.1 Contribution

As stated, the focus of this work was acoustic energy absorption in vehicle payload fairings. The contributions of this research were (1) eliminating low frequency

spillover inherent with using multiple positive position feedback (PPF) filters for control with the use of a modified bandpass Butterworth filter consisting of a sixth order high-pass Butterworth filter and a second order low-pass Butterworth filter, (2) determining an algorithm for setting the PPF and Butterworth filter parameters close to an optimal operating point from examining collocated transfer functions, and (3) designing an adaptive controller that used the previous algorithm and filters to update in real time for actively absorbing acoustic energy from an acoustic enclosure as the system changes. Tests performed on the cylindrical duct showed that the adaptive controller is capable of adapting the control for a 20 percent change in the acoustic modes and providing good SPL reduction.

5.2 Future Work and Recommendations

The results of this work have left several areas for potential future work. These areas are a math model of the combined filter, system weight (the speakers, power supply, and processor), and optimization of the adaptive controller. A detailed mathematical model of the combined filter of the PPF and two Butterworth filters is not presented in this work. The algorithm for setting the combined filter parameters was designed from the simulations and experiments on the cylindrical duct and full scale fairing simulator. A mathematical model could help derive the optimal filter parameters for the filter without having to tune the filter parameters for better closed-loop results. Then the adaptive controller algorithm could be coded from the mathematical model to always maintain the combined filters at their optimal settings.

The motivation for this work was launch cost. Current off-the shelf speakers are not optimized for weight and the speaker boxes used in this research with the fairing were made from medium density fiberboard (MDF). Parallel work, performed by another researcher, looked at constructing speaker boxes from carbon fiber and aluminum honeycomb with a current system weight of 25 pounds. Speaker drivers are made from magnets and wire coils, and speaker structures are usually made from steel or aluminum supporting the magnet and cone. Future work could look at redesigning the speaker to eliminate a portion of this support structure or to use a driver device less massive than magnets since the speakers currently occupy half of the system mass.

The adaptive controller currently requires 8 seconds to completely update the parameter buffer of the moving average after changes have been made in the system and does not account for rates or step changes in the system. Future work on the adaptation parameters and algorithm could include rate and step changes in a system. Optimizing the adaptation code could significantly reduce the total adaptation time of 8 seconds.

This proposed future work will serve as a step toward completing the research necessary for implementing this adaptive controller to reduce the SPL in a payload fairing. This research also has the possibility for future work in other applications where vibration reduction needs to be actively controlled for a potential time-varying structure. Mathematical modeling of the combined filter and reducing the time for the adaptation of the parameters will also be useful for implementing the adaptive controller in other applications.

Bibliography

Anderson, B. D. O., "Failures of Adaptive Control Theory and Their Resolution," *Communications in Information and Systems*, Vol. 5, No. 1, 2005, pp 1-20.

Astrom, K. J., Wittenmark, B. *Adaptive Control*, Reading, Massachusetts, Addison Wesley, 2nd ed., 1995.

Bass, H. E., Zuckerwar, A. J., Blackstock, D. T., Hester, D. M., "Atmospheric Absorption of Sound: Further Developments," *Journal of Acoustical Society of America*, Vol. 97, No. 1, Jan. 1995, pp 680-683.

Bass, H. E., Sutherland, L. C., Zuckerwar, A. J., "Atmospheric Absorption of Sound: Update," *Journal of Acoustical Society of America*, Vol. 88, No. 4, Oct. 1990, pp 2019-2021.

Beranek, L. L., *Acoustics*, Woodbury, New York, American Institute of Physics, 1996.

Bies, D. A., Hansen, C. H., *Engineering Noise Control Theory and Practice*, New York, New York, Spon Press, 3rd ed., 2003.

Clark, R. L., Gibbs, G. P., "Analysis, Testing, and Control of a Reverberant Sound Field within the Fuselage of a Business Jet," *Journal of Acoustical Society of America*, Vol. 105, No. 4, April 1999, pp 2277-2286.

Clark, R. L., Frampton, K. D., Cole, D. G., "Phase Compensation for Feedback Control of Enclosed Sound Fields," *Journal of Sound and Vibration*, Vol. 195, No 5, 1996, pp 701-718.

Clark, R. L., Cole, D. G., "Active Damping of Enclosed sound Fields Through Direct Rate Feedback Control," *Journal of Acoustical Society of America*, Vol. 97, No. 3, March 1995, pp 1710-1716.

DeGuilio, A. P., *A Comprehensive Experimental Evaluation of Actively Controlled Piezoceramics with Positive Position Feedback for Structural Damping*, Masters Thesis, Virginia Polytechnic Institute & State University, Mar. 2000.

Dorf, R. C., Bishop, R. H., *Modern Control Systems*, Upper Saddle River, New Jersey, Prentice Hall, 9th ed., 2001.

Eargle, J., *Loudspeaker Handbook*, Boston, Massachusetts, Kluwer Academic Publishers, 2nd ed., 2003.

Estève, S. J., Johnson, M. E., "Adaptive Helmholtz Resonators and Passive Vibration Absorbers for Cylinder Interior Noise Control," *Journal of Sound and Vibration*, Vol. 288, 2005, pp 1105-1130.

Estève, S. J., *Control of Sound Transmission into Payload Fairings Using Distributed Vibration Absorbers and Helmholtz Resonators*, PhD Dissertation, Virginia Polytechnic Institute & State University, May 2004.

Fanson, J. L., Caughey, T. K., "Positive Position Feedback Control for Large Space Structures," *AIAA Paper*, No. 87-0902, 1987, pp. 588-598.

Farinholt, K., *Modal and Impedance Modeling of a Conical Bore for Control Applications*, Masters Thesis, Virginia Polytechnic Institute & State University, Oct. 2001.

Green, K. W., *Piezoceramic Actuated Transducers for Interior Acoustic Noise Control*, Masters Thesis, Virginia Polytechnic Institute & State University, Aug. 2000.

Goodwin, G. C., Sin, K. S., *Adaptive Filtering Prediction and Control*, Englewood Cliffs, New Jersey, Prentice Hall, 1984.

Goh, C. J., *Analysis and Control of Quasi Distributed Parameter Systems*, PhD Dissertation, California Institute of Technology, 1983.

Herring, E., "Fairing Search Tool," *Access to Space*, NASA, 2006, retrieved on Sept. 13, 2006, from website: http://ats.gsfc.nasa.gov/ats3/tools/fairing_search.asp?proxyid=guest&xsection=3&subxsection=0

Hughes, W. O., McNelis, A. M., Himelblau H., "Investigation of Acoustic Fields for The Cassini Spacecraft: Reverberant Versus Launch Environments," AIAA journal paper 99-1985, 1999, pp 1193-1203.

Howard, C. Q., Hansen, C. H., Zander, A., "Vibro-Acoustic Noise Control Treatments for Payload Bays of Launch Vehicles: Discrete to Fuzzy Solutions," *Applied Acoustics*, Vol. 66, 2005, pp 1235-1261,

Inman, D. J., *Engineering Vibration*, Upper Saddle River, New Jersey, Prentice Hall, 2nd ed., 2001.

Kemp, J. D., Clark, R. L., "Noise Reduction in a Launch Vehicle Fairing Using Actively Tuned Loudspeakers," *Journal of the Acoustical Society of America*, Vol. 113, No.4, April 2003, pp 1986-1994.

Kidner, M. R. F., Fuller, C. R., Gardner, G., "Increase in Transmission Loss of Single Panels by Addition of Mass Inclusions to a Poro-Elastic Layer: Experimental Investigation," *Journal of Sound and Vibration*, Vol. 294, 2006, pp 466-472.

Kinsler, L. E., Frey, A. R., Coppens, A. B., Sanders, J. V., *Fundamentals of Acoustics*, New York, New York, John Wiley & Sons, 4th ed., 2000.

Krstic, M., Kanellakopoulos, I., Kokotovic, P. V., *Nonlinear and Adaptive Control Design*, New York, New York, Wiley, 1995.

Lane, S. A., Johnson, M., Fuller, C., Charpentier, A., "Active Control of Payload Fairing Noise," *Journal of Sound and Vibration*, Vol. 290, 2006, pp 794-819.

Lane, S. A., Richard, R. E., Kennedy, S. J., "Fairing Noise Control Using Tube-Shaped Resonators," *Journal of Spacecraft and Rockets*, Vol. 42, No. 4, 2005, pp 640-646.

Lane, S. A., Griffin, S., Leo, D., "Active Structural-Acoustic Control of Composite Fairings Using Single-Crystal Piezoelectric Actuators," *Smart Materials and Structures*, Vol. 12, 2003, pp 96-104.

Lane, S. A., Clark, R. L., Southward, S. C., "Active Control of Low Frequency Modes in an Aircraft Fuselage Using Spatially Weighted Arrays," *Journal of Vibration and Acoustics*, Vol. 122, 2000, pp 227-234.

Leo, D. J., Limpert, D., "Letters to the Editor, A Self-Sensing Technique for Active Acoustic Attenuation," *Journal of Sound and Vibration*, Vol. 235, No. 5, 2000, pp 863-873.

Li, D., Vipperman, J. S., "On the Noise Transmission and Control for a Cylindrical Chamber Core Composite Structure," *Journal of Sound and Vibration*, Vol. 288, 2005, pp 235-254.

Lueg, P., "Process of Silencing Sound Oscillations," 1936, US Patent 2, 043, 416.

McEver, M. A., Moon, S., Cole, D. G., Clark, R. L., "Adaptive Control for Interior Noise Control in Rocket Fairings," *AIAA 2003-1811*, 2003, pp 1-10.

McEver, M. A., *Optimal Vibration Suppression Using On-line Pole/Zero Identification*, Master's Thesis, Virginia Polytechnic Institute & State University, 1999.

Narendra, K. S., Annaswamy, A. M., *Stable Adaptive Systems*, Englewood Cliffs, New Jersey, Prentice Hall, 1980.

RadioShack, *8" Polypropylene Cone (400-1024A) Specifications Faxback Doc. # 15880 Woofer*, 1995, retrieved 7 Aug. 2006, from RadioShack support website: http://support.radioshack.com/support_audio/doc15/15880.htm

Rayleigh, L. (J. W. S. Strutt), *The Theory of Sound*, (New York: Dover Publications, 2nd ed, 1945 re-issue), Vol. II, 1877, p 170.

Sacarcelik, O., *Acoustic Devices for the Active & Passive Control of Sound in a Payload Compartment*, Masters Thesis, Virginia Polytechnic Institute & State University, May. 2004.

Sastry, S., Bodson, M., *Adaptive control: Stability, Convergence, and Robustness*, Englewood Cliffs, New Jersey, Prentice Hall, 1989.

Sengiel, E., Studiotechnik Aufnahmetechnik Tontechnik Forum Sengpielaudio, *Calculation: Speed of Sound in Humid Air*, retrieved 26 May 2005, from website: http://www.sengpielaudio.com/calculator-airpressure.htm

Smith, J. O., *Butterworth Lowpass Poles and Zeros*, Center for Computer Research in Music and Acoustics, 2006, retrieved 12 May 2006, from website: http://www-ccrma.stanford.edu/~jos/filters/Butterworth_Lowpass_Poles_Zeros.html

Smith, S. W., *The Scientist and Engineer's Guide to Digital Signal Processing*, San Diego, California, California Technical Publishing, 2nd ed., 1999.

University of Illinois at Chicago, *Design of a 5th Order Butterworth Low-Pass Filter using Sallen & Key Circuit*, 2006, retrieved 12 May 2006, from website: http://www.ece.uic.edu/~jmorisak/blpf.html

Wessen, A., *Cassini-Huygens Mission to Saturn & Titan*, Jet Propulsion Laboratory, California Institute of Technology, 2005, retrieved on Sept. 13, 2006, from website: http://saturn.jpl.nasa.gov/multimedia/images/image-details.cfm?imageID=949

Appendix A

Absorption Coefficient

A more detailed discussion can be found in Kinsler et al. (2000, pp 210-241)

Absorption can come from several different sources; viscosity, thermal conduction, molecular thermal relaxation of the air, and viscous losses and conduction from the rigid walls of the cylindrical duct. The viscosity absorption coefficient (α_s), also called the spatial absorption coefficient, for the air is a function of frequency, the speed of sound, and the relaxation time (τ_s). The equation is

$$\alpha_s = \frac{\omega}{c}\frac{1}{\sqrt{2}}\left[\frac{\sqrt{1+(\omega\tau_s)^2}-1}{1+(\omega\tau_s)^2}\right]^{\frac{1}{2}} \tag{A.1}$$

and should only be used for $\omega\tau_s << 1$, which implies a bound for the frequency range, and can be reduced to the following approximation,

$$\alpha_s \approx \frac{1}{2}\frac{\omega^2}{c}\tau_s . \tag{A.2}$$

The relaxation time is found using the following equation,

$$\tau_s = \left(\frac{4}{3}\eta + \eta_B\right)\Big/\rho c^2 , \tag{A.3}$$

where η is the coefficient of shear viscosity and η_B is the coefficient of bulk viscosity (usually assumed to be zero when the fluid is air). The shear viscosity can be found using the following equation,

$$\eta = {}^{1}\!/_{3}\,\rho_O l v , \tag{A.4}$$

where ρ_o is the equilibrium density, l is the mean free path of the gas atoms between successive collisions, and v is the average speed of the molecules in a perfect gas. This average speed can be found using

$$v = \sqrt{8rT_K / \pi}, \tag{A.5}$$

where r is the specific gas constant and T_K is the current temperature in absolute units. For this research the coefficient of shear viscosity is estimated from a properties table (Kinsler, 2000, p 528).

The thermal conduction absorption coefficient (α_κ) for air is a function of the equilibrium density, the speed of sound, frequency, thermal conductivity (κ), ratio of specific heats (γ), and the specific heat at constant pressure (c_p) and is

$$\alpha_\kappa = \frac{\omega^2}{2\rho_O c^3}\frac{(\gamma-1)\kappa}{c_P}. \tag{A.6}$$

The addition of the thermal conduction absorption and the viscosity absorption coefficients are termed the classical absorption coefficients.

The absorption coefficient for molecular thermal relaxation can replace the classical absorption coefficient with more accuracy in the lower frequency range and is therefore used in this research. The molecular thermal relaxation absorption coefficient (α_m) can be found from the following equation (Bass, 1990),

$$\begin{aligned}\alpha_m = {} & f^2\left(1.84\times10^{-11}\right)\left(\frac{p_s}{p_{s0}}\right)^{-1}\left(\frac{T}{T_0}\right)^{0.5} \\ & + f^2\left(\frac{T}{T_0}\right)^{-2.5}\left\{\frac{\left(1.278\times10^{-2}\right)e^{(-2239.1/T)}}{f_{r,O}+\left(f^2/f_{r,O}\right)}+\frac{\left(1.068\times10^{-1}\right)e^{(-3352/T)}}{f_{r,N}+\left(f^2/f_{r,N}\right)}\right\}\end{aligned} \tag{A.7}$$

where p_s is the atmospheric pressure, p_{s0} is the reference atmospheric pressure, T is the temperature in Kelvin, T_0 is the reference atmospheric temperature, f is the frequency in Hz, $f_{r,0}$ is the relaxation frequency of molecular oxygen, and $f_{r,N}$ is the relaxation frequency of molecular nitrogen. The relaxation frequency of molecular nitrogen is found from the following equation,

$$f_{r,N} = \frac{p_s}{p_{so}}\left(\frac{T_O}{T}\right)^{1/2}\left(9 + 280he^{-4.17\left[\left(\frac{T_O}{T}\right)^{1/3}-1\right]}\right) \tag{A.8}$$

and the relaxation frequency of molecular oxygen is found from the following equation,

$$f_{r,O} = \frac{p_s}{p_{so}}\left(24 + 40400h\frac{(0.02+h)}{(0.391+h)}\right) \tag{A.9}$$

where h is the percent of the molar concentration of water vapor. The molar concentration of water vapor can be found by

$$h = h_r\left(\frac{p_{sat}}{p_{so}}\right)\left(\frac{p_s}{p_{so}}\right)^{-1}, \tag{A.10}$$

where h_r is the relative humidity in percent and p_{sat} is the saturated vapor pressure which is found from the following equation (Bass, 1995),

$$p_{sat} = p_{so} \times 10^{\left(-6.8346\left(T_{01}/T\right)^{1.261}+4.6151\right)} \tag{A.11}$$

where T_{01} is the triple-point isotherm temperature.

The absorption coefficient for wall losses (viscous and thermal) (α_w) is defined as

$$\alpha_w = \frac{1}{ac}\left(\frac{\eta\omega}{2\rho}\right)^{0.5}\left(1+\frac{\gamma-1}{\sqrt{\Pr}}\right) \tag{A.12}$$

where Pr is the Prandtl number of air and a is the radius of the duct.

When the absorption losses are small, an assumption can be made that the total absorption is the sum of each individual absorption coefficient, therefore the total absorption coefficient is

$$\alpha = \sum_i \alpha_i \ . \tag{A.13}$$

The absorption coefficient used in Chapter 2 is the sum of the molecular thermal relaxation absorption coefficient and the wall losses absorption coefficient. All the constants used in equations A.1 through A.13 can be found in Table A.1. The actual absorption values calculated are increased by an order of magnitude for the model to more closely match the measured data.

Table A.1. Constants and units used in the absorption coefficient calculations.

variable/constant	symbol	value	units
spatial absorption	α_s	function of freq.	m^{-1}
coefficient of shear viscosity	η	1.88×10^{5}	Pa-s
coefficient of bulk viscosity	η_B	0	Pa-s
density	ρ	1.1877	kg/m^3
speed of sound	c	345.25	m/s
relaxation time	τ_s	1.7706×10^{-10}	s
thermal conduction absorption	α_κ	function of freq.	m^{-1}
ratio of specific heats	γ	1.402	unitless
thermal conductivity	κ	0.0263	W/(mK)
specific heat at constant pressure	c_p	1010	J/(kgK)
molecular thermal relaxation absorption	α_m	function of freq.	m^{-1}
atmospheric pressure	p_s	100,677.32	Pa
reference atmospheric pressure	p_{s0}	101,325	Pa
temperature	T	295.15	K
reference atmospheric temperature	T_0	273.15	K
relaxation frequency of molecular oxygen	$f_{r,0}$	41,225	Hz
relaxation frequency of molecular nitrogen	$f_{r,N}$	399.19	Hz
relative humidity	h_r	50	percent
molar concentration of water vapor	h	1.31	percent
saturated vapor pressure	p_{sat}	2,642.2	Pa
triple-point isotherm temperature	T_{01}	273.16	K
wall losses absorption	α_w	function of freq.	m^{-1}
Prandtl number	Pr	0.710	unitless
radius	a	0.1016	m

Appendix B

Additional Analytical Results

B.1 Analytical Cylindrical Duct Response

The P_2/V_i transfer fucntion of the cylindrical duct, defined from Figure 2.5, with the analytical model overlaid for comparison can be seen in Figure B.1. The analytical model is adjusted for the sensitivity of the microphone. Figure B.2 shows the P_3/V_i transfer function of the cylindrical duct with the analytical model overlaid for comparison. The ordinate of the magnitude plots for both figures is of the microphone voltage output over the speaker voltage input in decibels. The ordinate of the phase plots for both figures is in degrees and the abscissa for all the plots is the frequency in Hz.

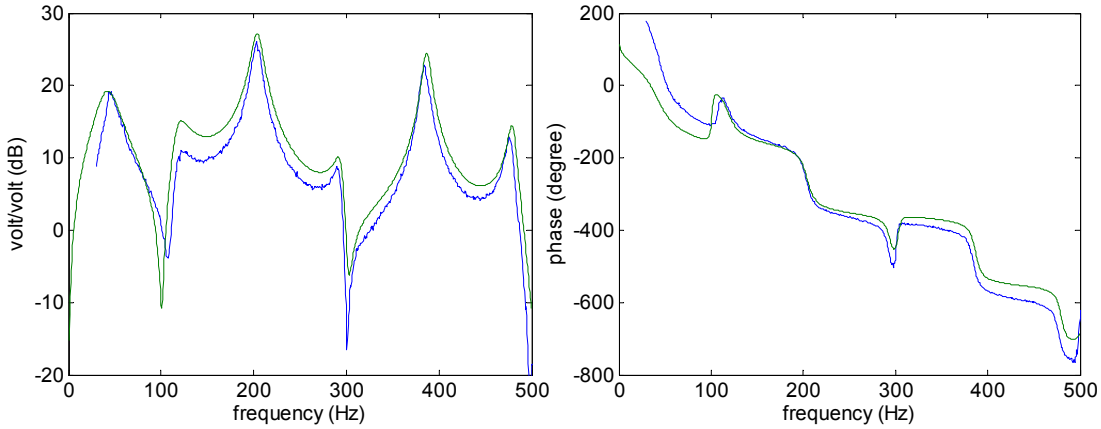

Figure B.1. Measured P_2/V_i transfer function (blue) of the duct with the analytical model (green) overlaid on top.

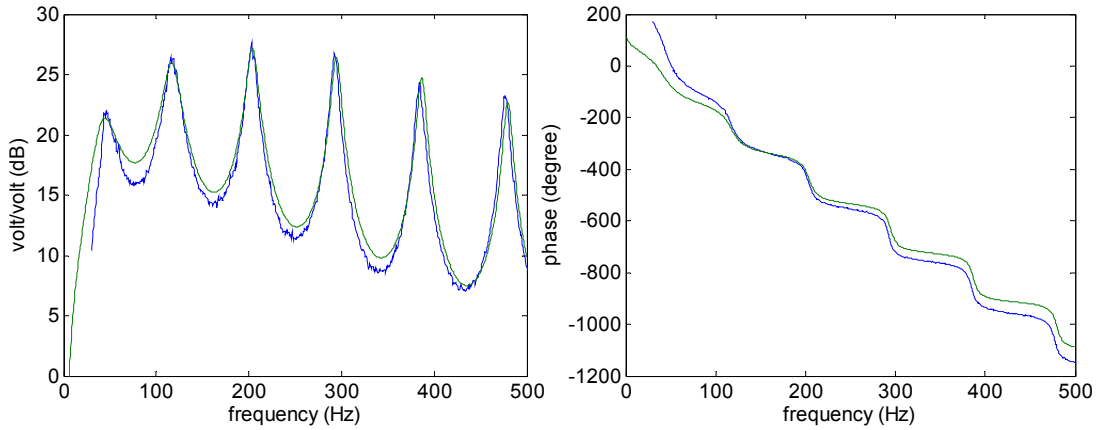

Figure B.2. Measured P_3/V_i transfer function (blue) of the duct with the analytical model (green) overlaid on top.

B.2 Analytical Control Response

The analytical control response is the closed-loop estimated results of the system using the model derived in Chapter 2 for the system and with two different filter approximation schemes. The analytical control filters are from McEver's optimization algorithm and Goh's filter equations as explained in Chapter 2. Results are shown for both the P_2/V_i and P_3/V_i transfer functions of the duct using McEver's algorithm as well as Goh's equations. Also shown, are results using the retuned filter parameters. A series of figures will show the spillover effect that results from adding multiple PPF filters for control to the system. The ordinate of the magnitude plots is the approximated SPL, in decibels, and the ordinate of the phase plots is in degrees. The abscissa of all the plots is the frequency in Hz.

B.2.1 McEver's Algorithm

Figure B.3 shows the P_2/V_i transfer function model overlaid by the analytical closed-loop controlled estimate where the feedback filter is designed from McEver's algorithm. Figure B.4 shows the P_3/V_i transfer function model overlaid by the analytical closed-loop estimate using the same feedback filter.

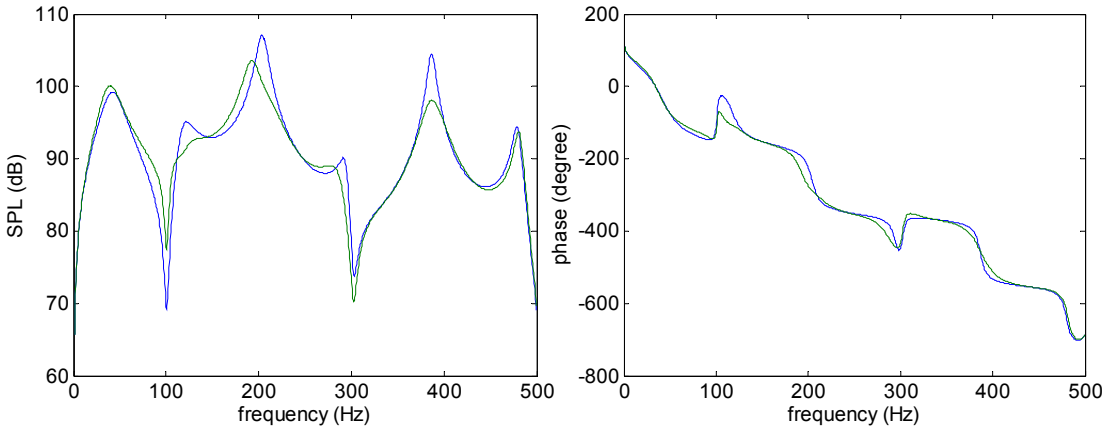

Figure B.3. Analytical model of P_2/V_i (blue) of the duct with the analytical closed-loop controlled estimate (green) overlaid on top.

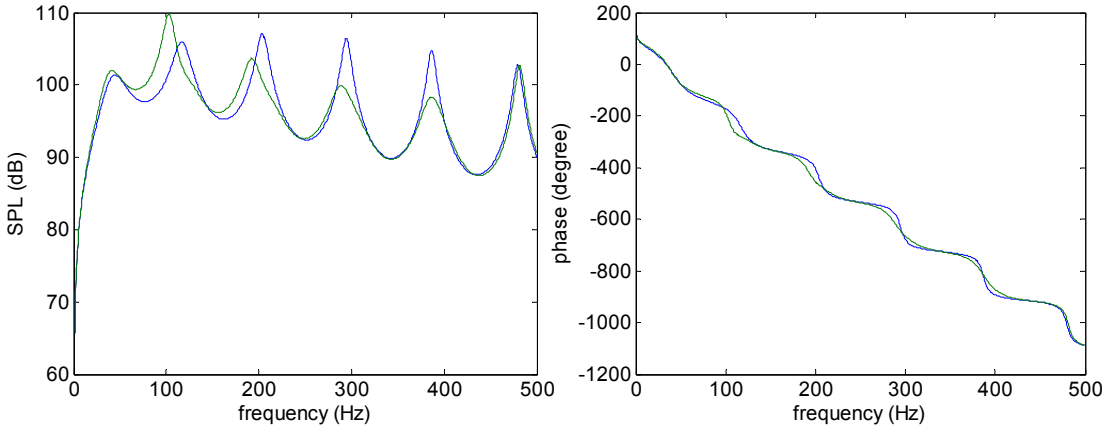

Figure B.4. Analytical model of P_3/V_i (blue) of the duct with the analytical closed-loop controlled estimate (green) overlaid on top.

Figures B.5 through B.8 is the series of figures showing the effects of spillover as additional PPF filters are added to the feedback compensator for control (Figure B.5 has 1 filter, Figure B.6 has 2 filters, etc.). As the additional filters are added to the closed-loop estimate, the magnitudes of the lower modes increase because of the flat response of the PPF filter at low frequency which inherently causes spill-over.

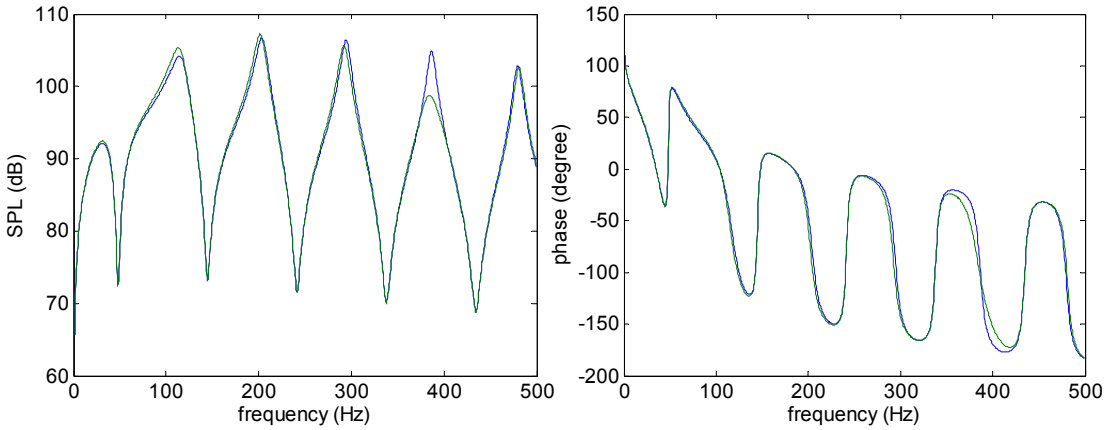

Figure B.5. Analytical model of P_1/V_i (blue) of the duct with the analytical closed-loop controlled estimate (green) overlaid on top with control applied to the fifth mode.

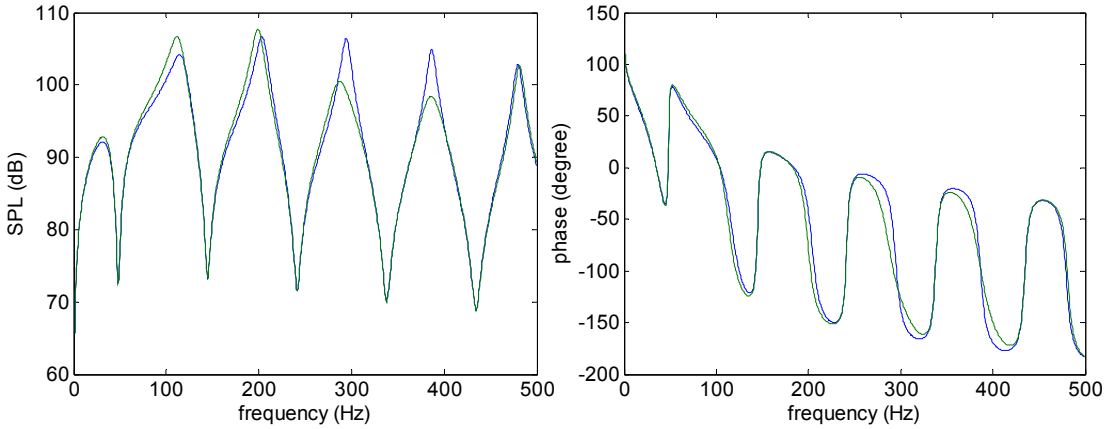

Figure B.6. Analytical model of P_1/V_i (blue) of the duct with the analytical closed-loop controlled estimate (green) overlaid on top with control applied to the fourth and fifth mode.

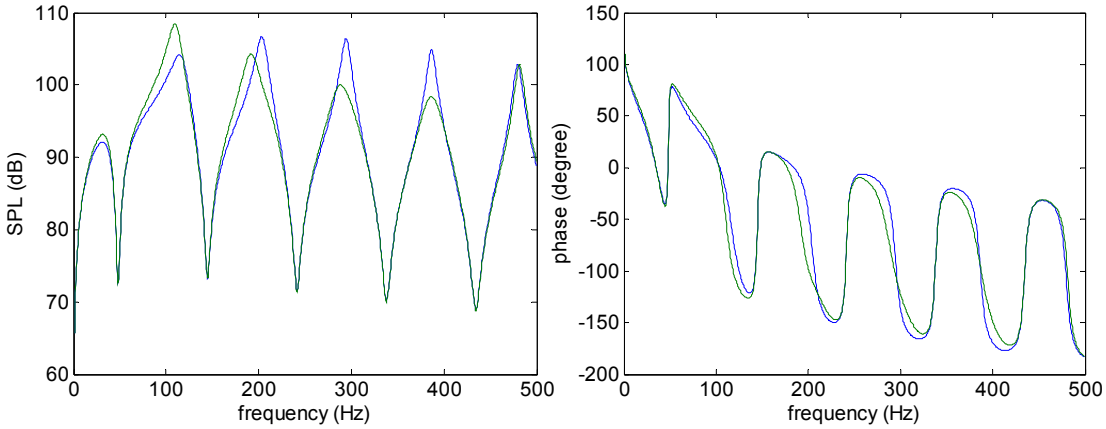

Figure B.7. Analytical model of P_1/V_i (blue) of the duct with the analytical closed-loop controlled estimate (green) overlaid on top with control applied to the third through fifth modes.

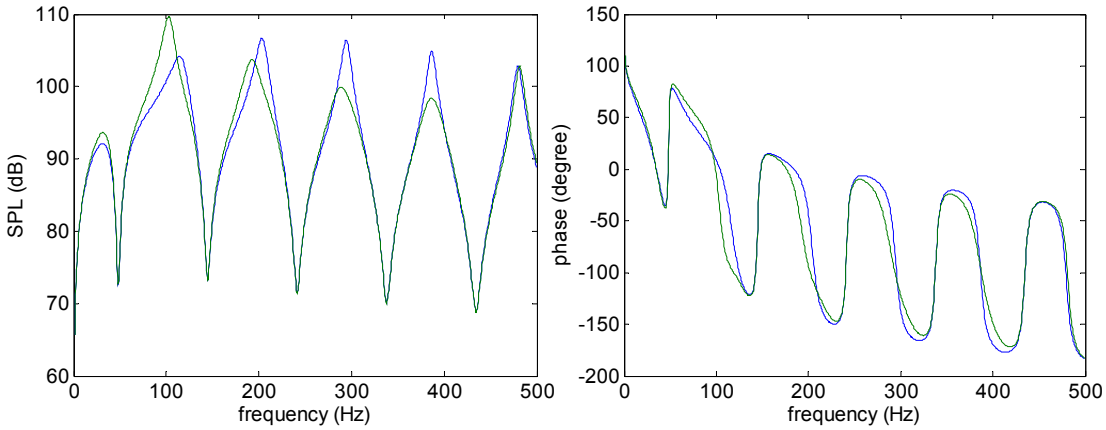

Figure B.8. Analytical model of P_1/V_i (blue) of the duct with the analytical closed-loop controlled estimate (green) overlaid on top with control applied to the second through fifth modes.

Figures B.9 and B.10 show the analytical model of the P_2/V_i and P_3/V_i transfer functions overlaid by the analytical closed-loop control estimate with the frequencies of the filters, found using McEver's algorithm, retuned as explain in Chapter 2.

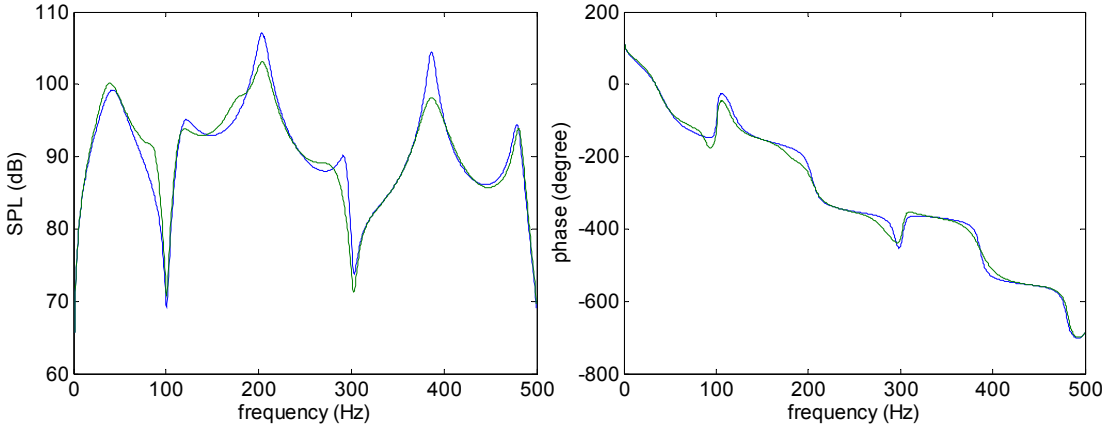

Figure B.9. Analytical model of P_2/V_i (blue) of the duct with the analytical closed-loop controlled estimate (green) overlaid on top with the filter frequencies retuned.

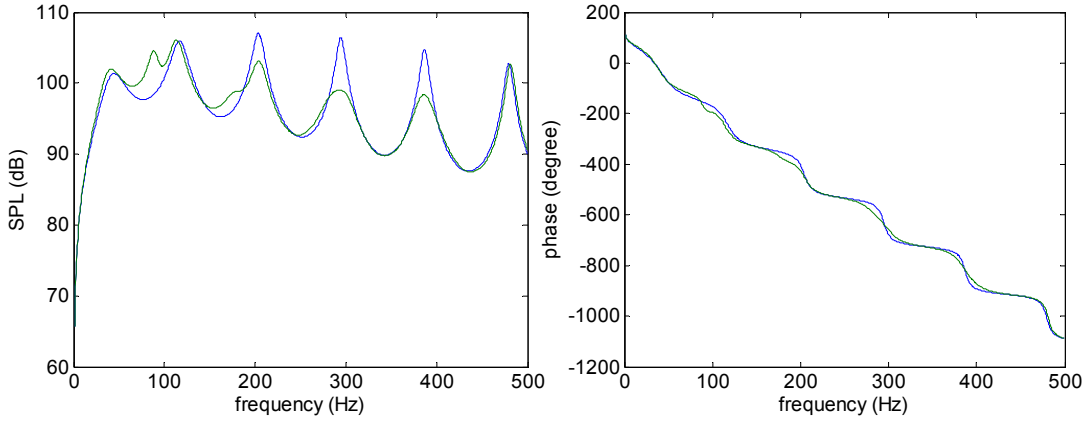

Figure B.10. Analytical model of P_3/V_i (blue) of the duct with the analytical closed-loop controlled estimate (green) overlaid on top with the filter frequencies retuned.

B.2.2 Goh's Equations

Figures B.11 and B.12 show the analytical model of the P_2/V_i and P_3/V_i, transfer functions, respectively, overlaid by the analytical closed-loop controlled estimate where the compensator is designed using Goh's filter equations.

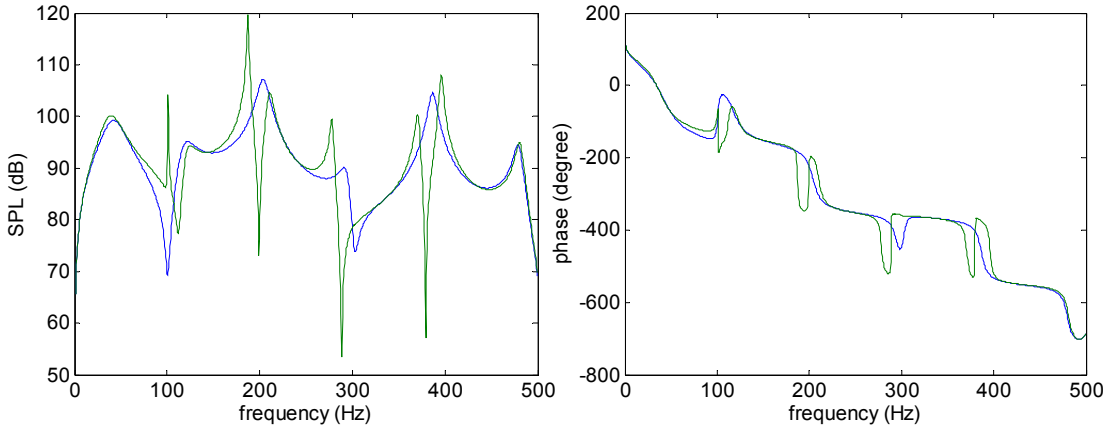

Figure B.11. Analytical model of P_2/V_i (blue) of the duct with the analytical closed-loop controlled estimate (green) overlaid on top.

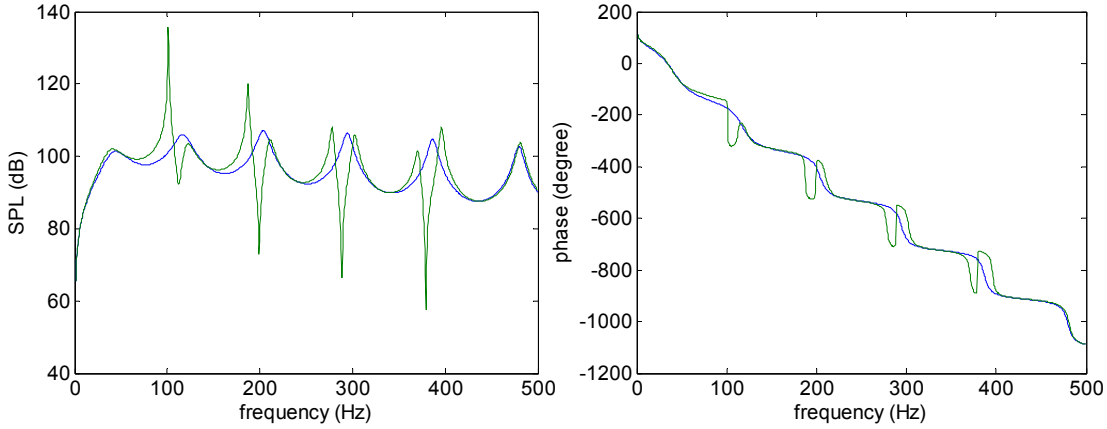

Figure B.12. Analytical model of P_3/V_i (blue) of the duct with the analytical closed-loop controlled estimate (green) overlaid on top.

Figures B.13 and B.14 show the analytical model of the P_2/V_i and P_3/V_i transfer functions, respectively, overlaid by the analytical closed loop control estimate where the compensator is designed from Goh's filter equation with the damping ratios and frequencies of the filters retuned, as explained in Chapter 2.

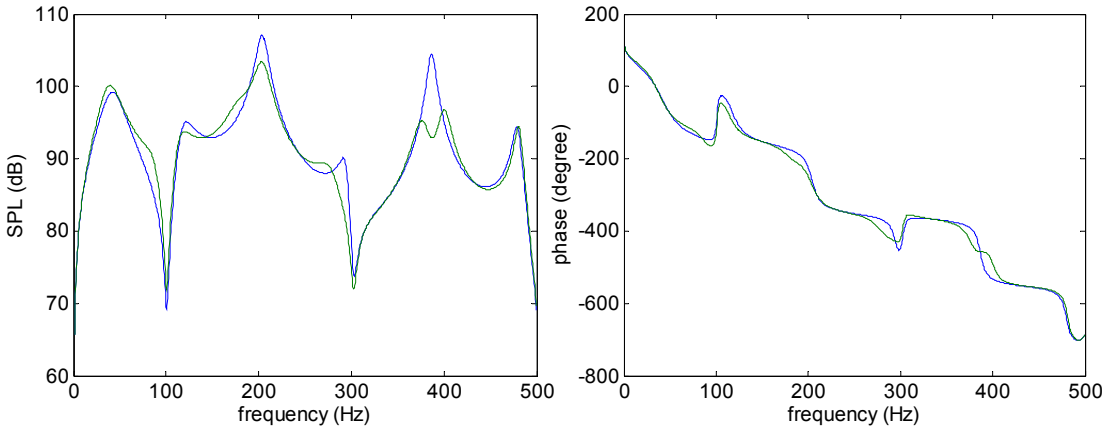

Figure B.13. Analytical model of P_2/V_i (blue) of the duct with the analytical closed-loop controlled estimate (green) overlaid on top with the filter frequencies and filter damping ratios retuned.

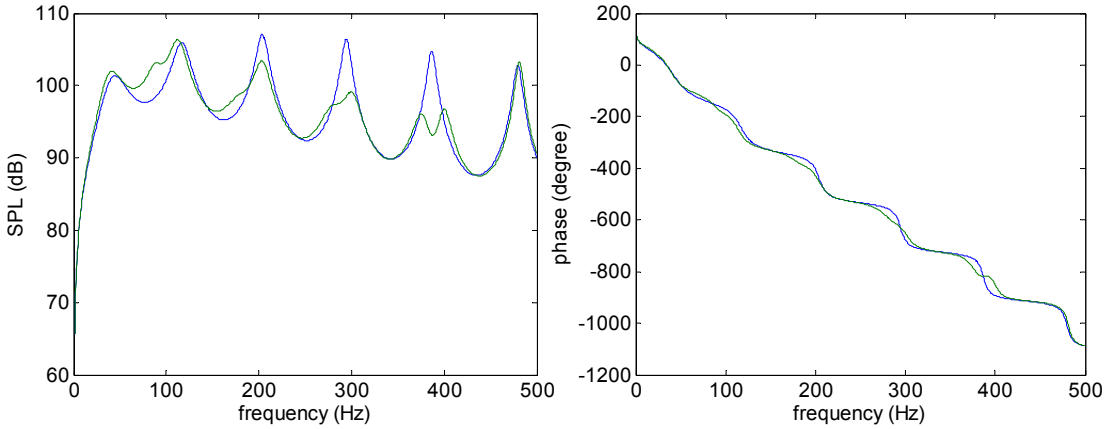

Figure B.14. Analytical model of P_3/V_i (blue) of the duct with the analytical closed-loop controlled estimate (green) overlaid on top with the filter frequencies and filter damping ratios retuned.

Appendix C

Additional Non-Adaptive Control Results

This appendix contains the additional results at other measurement locations not included in Chapter 3. Duct results for control using McEver's algorithm, Goh's equations, and the combined filters are shown as well as a comparison between the measured control response of the system (using the combined filters) and the analytical closed-loop estimation using the measured data (with simulated feedback filters) to simulate the results. Measured baseline fairing transfer functions are presented as well as the measured closed-loop control system at the same locations. The ordinate of the magnitude plots is the output voltage measured by the microphones over the input voltage into the speakers, in decibels, and the ordinate of the phase plots is in degrees. The abscissa of each plot is the frequency in Hz.

C.1 Cylindrical Duct

All the cylindrical duct figures below will be of either the P_2/V_i transfer function of the duct or the P_3/V_i transfer function of the duct.

C.1.1 McEver's Algorithm

The measured P_2/V_i transfer function of the duct and the measured closed-loop controlled transfer function, where the compensator used for control is designed using McEver's algorithm, can be seen in Figure C.1. Figure C.2 shows the measured P_3/V_i transfer functions of the duct.

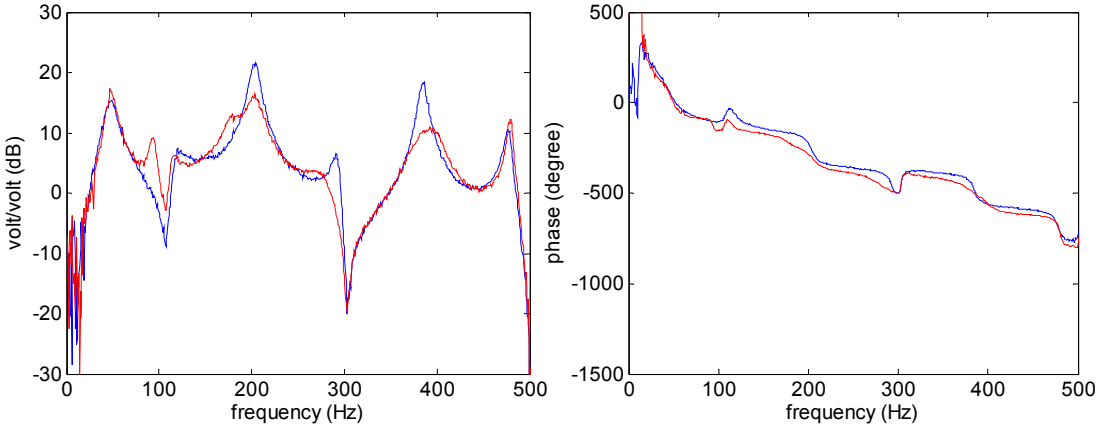

Figure C.1. Measured P_2/V_i transfer function (blue) of the duct with the measured controlled closed-loop transfer function (red) overlaid on top.

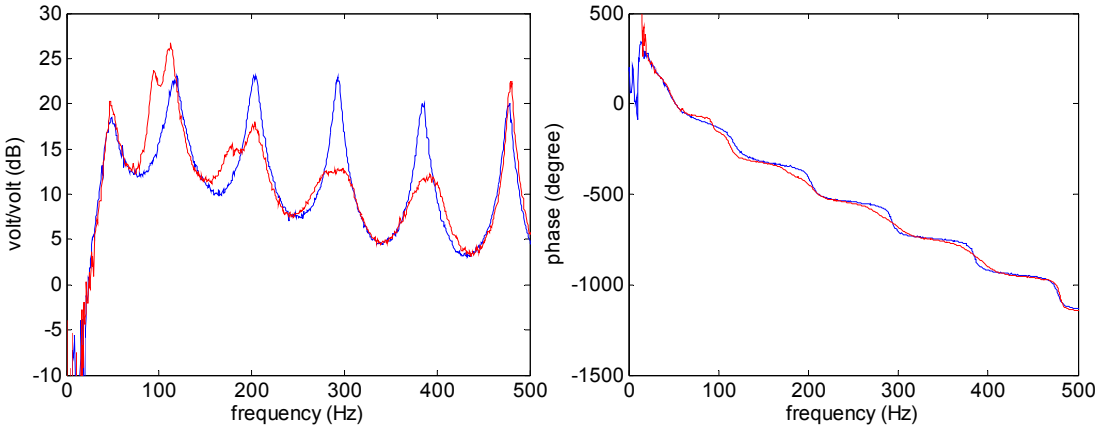

Figure C.2. Measured P_3/V_i transfer function (blue) of the duct with the measured controlled closed-loop transfer function (red) overlaid on top.

C.1.2 Goh' Equations

Figure C.3 shows the P_2/V_i transfer function of the duct and the measured closed-loop controlled transfer function, where the compensator used for control is designed using Goh's filter equations. Figure C.4 shows the P_3/V_i transfer functions of the duct using the same controller for the controlled closed-loop system.

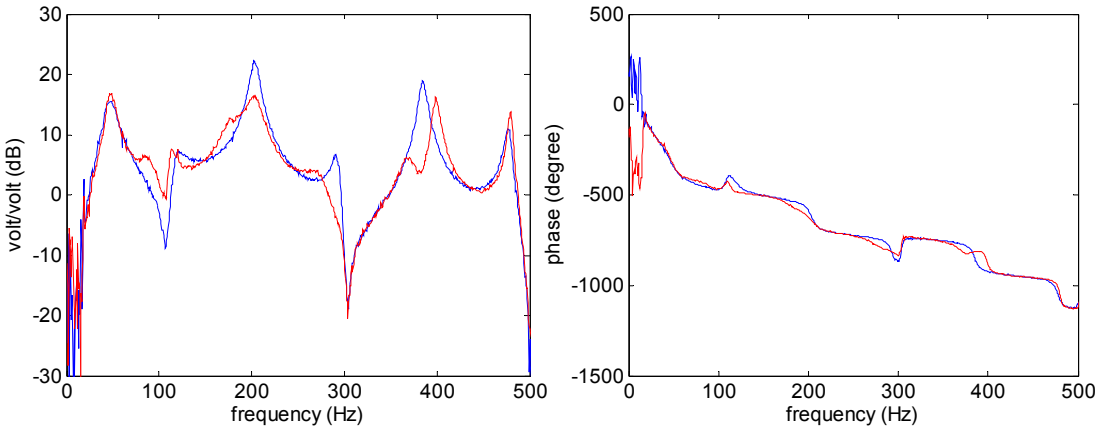

Figure C.3. Measured P_2/V_i transfer function (blue) of the duct with the measured controlled closed-loop transfer function (red) overlaid on top.

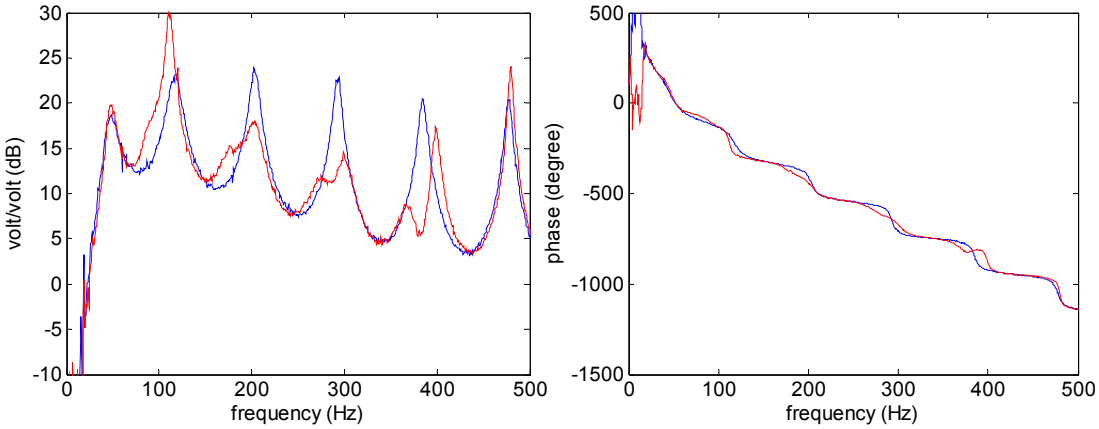

Figure C.4. Measured P_3/V_i transfer function (blue) of the duct with the measured controlled closed-loop transfer function (red) overlaid on top.

C.1.3 Combined Filters

Examining Figures C.2 and C.4 show that the measured controlled P_3/V_i transfer function magnitude is significantly increased for both controllers (McEver's algorithm and Goh's equation). The reason for this increase is the low frequency spill-over inherent with the use of multiple PPF filters as explained in Chapter 3. This spillover causes the overall SPL reduction to be minimal at the collocated and P_3 measurements. Therefore, Butterworth filters are used to design a filter that reduced the inherent PPF filter spillover.

Figure C.5 shows the measured P_2/V_i transfer function of the duct with the measured closed-loop control transfer function, where the controller is designed using the addition of combined filters to reduce the spill-over effect. Figure C.6 shows the

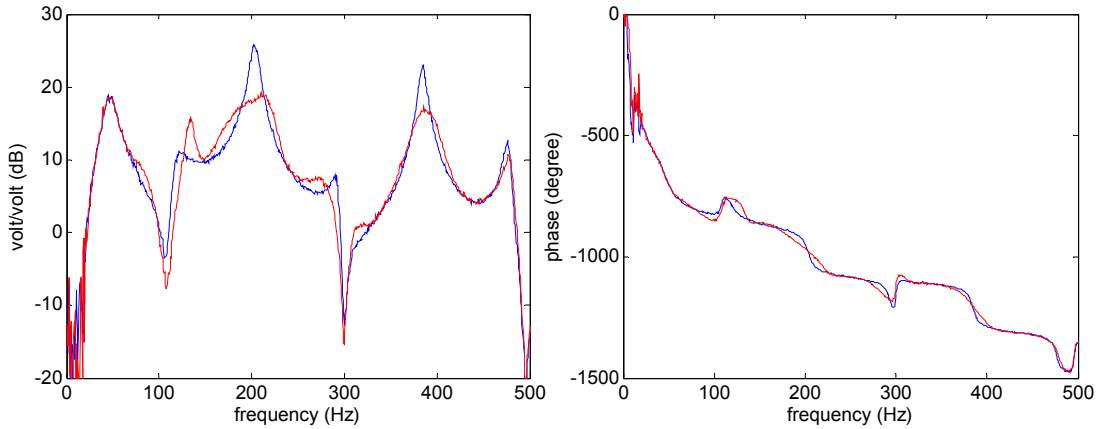

Figure C.5. Measured P_2/V_i transfer function (blue) of the duct with the measured controlled closed-loop transfer function (red) overlaid on top.

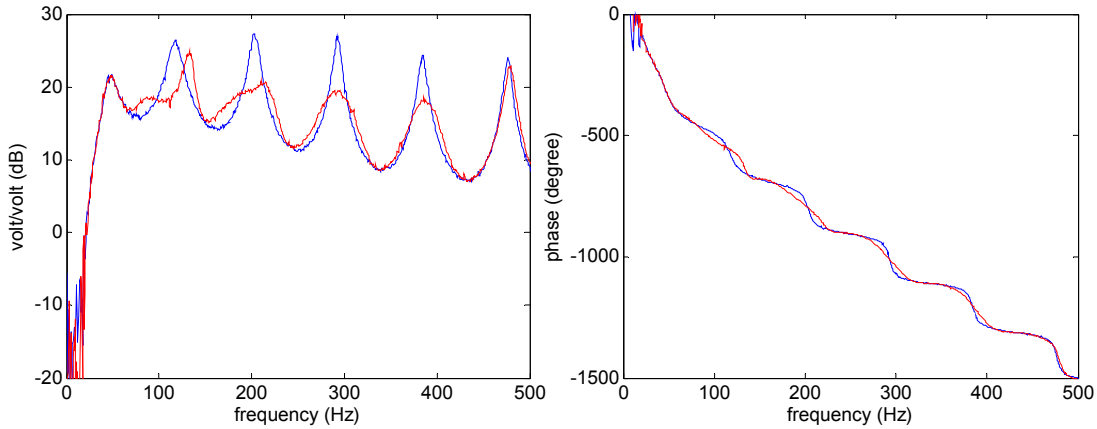

Figure C.6. Measured P_3/V_i transfer function (blue) of the duct with the measured controlled closed-loop transfer function (red) overlaid on top.

measured P_3/V_i transfer function of the duct for the controlled and uncontrolled cases. This figure shows that the spillover effect shown in Figures C.2 and C.4 is reduced.

C.2 Measured/Analytical Comparison

Figure C.7 shows the measured P_2/V_i transfer function overlaid with the measured closed-loop system data and the simulated closed-loop response. The purpose of this figure is to compare the simulated closed-loop response of the system to the actual measured controlled system. The compensator is designed with a combined filter for each mode. Figure C.8 shows the same information for the P_3/V_i transfer functions. Both of these figures show that using the measured baseline data to estimate the potential

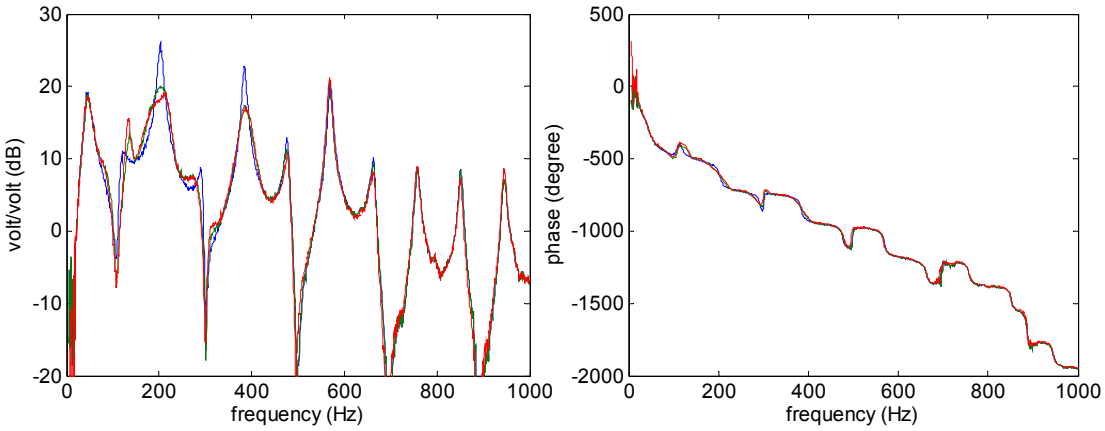

Figure C.7. Measured P_2/V_i transfer function (blue) of the duct with the controlled closed-loop transfer function (red) and the simulated controlled model (green) overlaid on top.

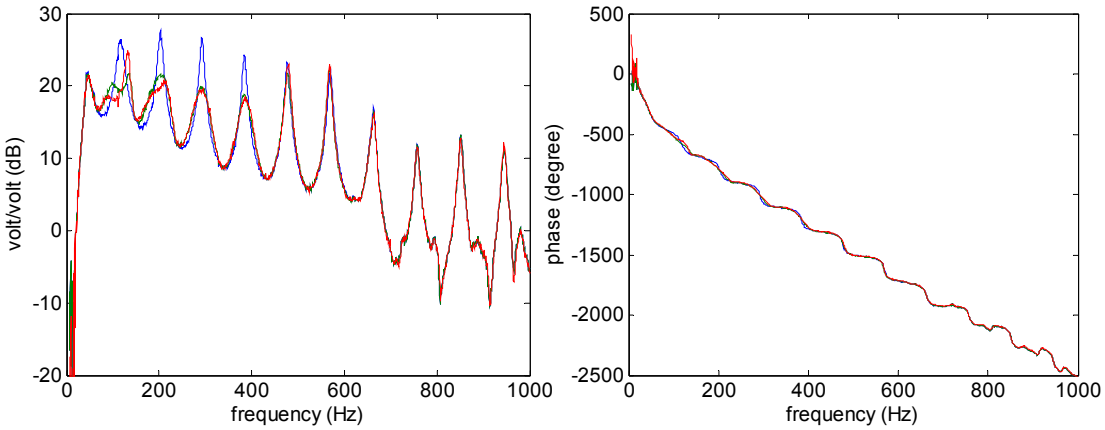

Figure C.8. Measured P_3/V_i transfer function (blue) of the duct with the controlled closed-loop transfer function (red) and the data/model controlled model (green) overlaid on top.

closed-loop response provides a better estimation of what the actual measured closed-loop system will do.

C.3 Payload Fairing

Figure C.9 shows the magnitude of the measured transfer functions in the fairing where the plot on the left is the P_2/V_i transfer function in the fairing and the plot on the right is the P_4/V_i transfer function.

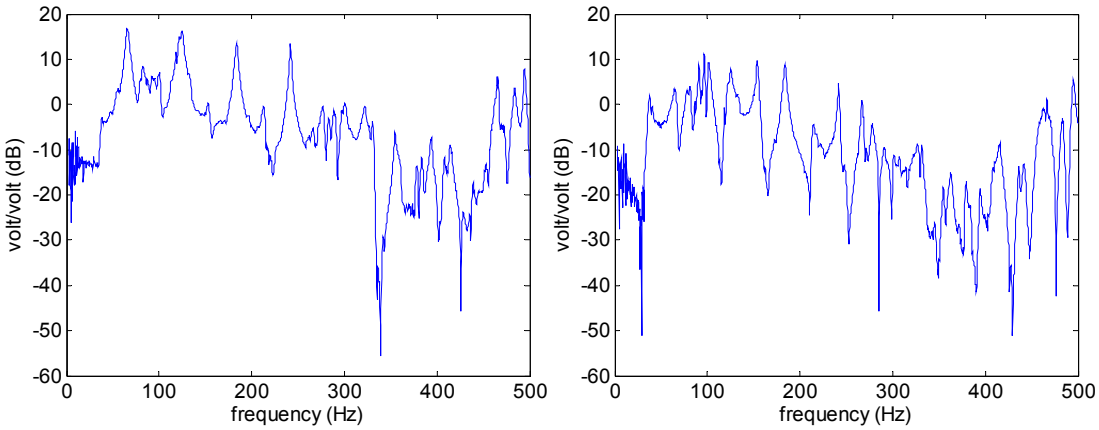

Figure C.9. Magnitude plots of the transfer functions for the payload fairing.

Figure C.10 through C.12 show the collocated transfer functions of the fairing as the input is applied to each individual speaker. The blue transfer functions are associated with the microphone placed in front of speaker A as defined in the figures, the green transfer functions are associated with the microphone placed in front of speaker B, and the red transfer functions are associated with the microphone placed in front of speaker C. All three of the true collocated transfer functions have close pole zero spacing with the pole/zero cancellation in the 350 to 450 Hz range. The other transfer functions for the non-collocated do not have the very close pole zero spacing of the collocated transfer functions. The non-collocated does not have the pole/zero cancellation through the 350 to 450 Hz frequency range. The only difference between the collocated and the non-collocated transfer functions is the location of the microphones in the radial direction, therefore the pole/zero cancellation seen in the collocated measurements here and in Chapter 3 must be caused by the near field effects of the speakers. The phase roll-off between 0 and 150 Hz is similar to the phase roll-off seen with the duct that is caused by the amplifier and is probably the cause of this roll-off.

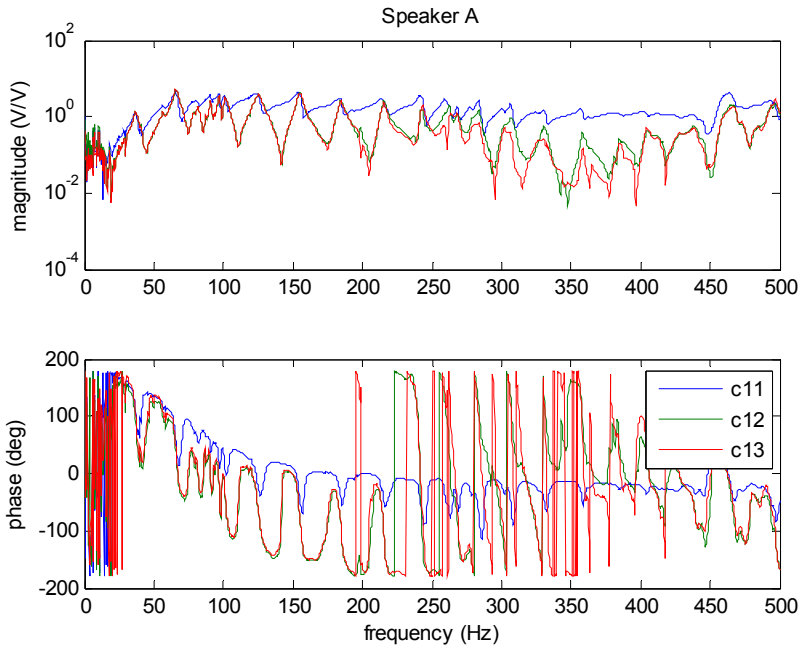

Figure C.10. Transfer functions of the nose microphone outputs over the disturbance input into one of the nose actuators.

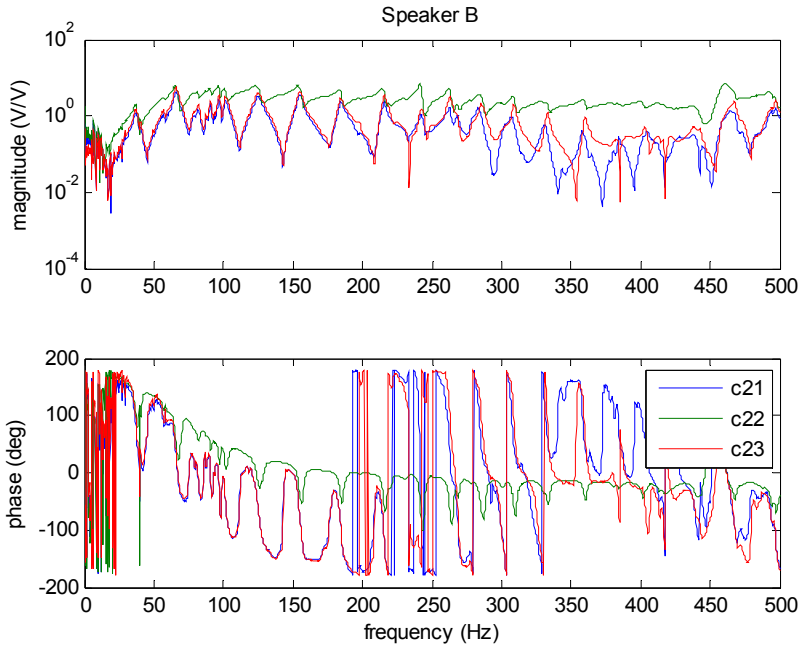

Figure C.11. Transfer functions of the nose microphone outputs over the disturbance input into one of the nose actuators.

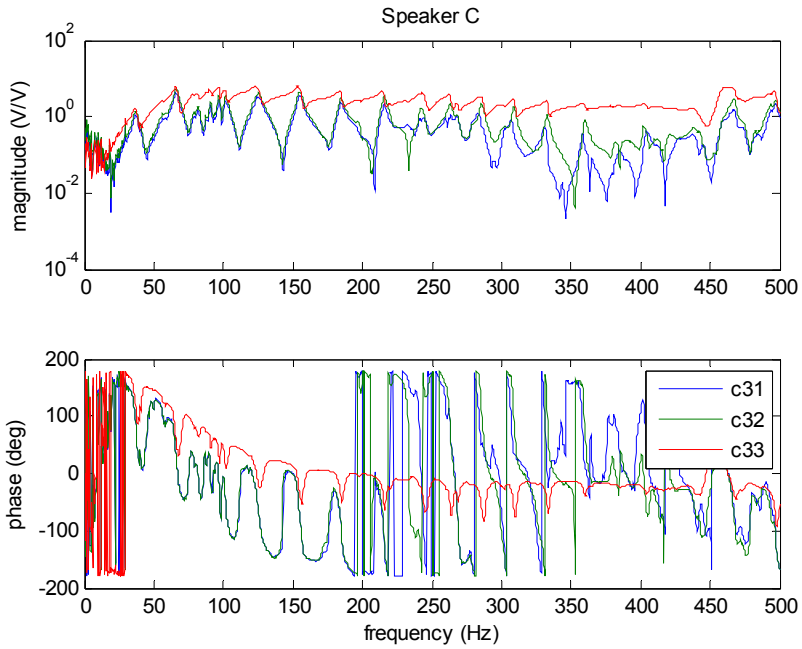

Figure C.12. Transfer functions of the nose microphone outputs over the disturbance input into one of the nose actuators.

Figure C.13 shows the same baseline magnitude plots of Figure C.9 with the closed-loop controlled measured data overlaid on top. The figures show how the peak magnitude responses below 300 Hz of these two locations are reduced with control.

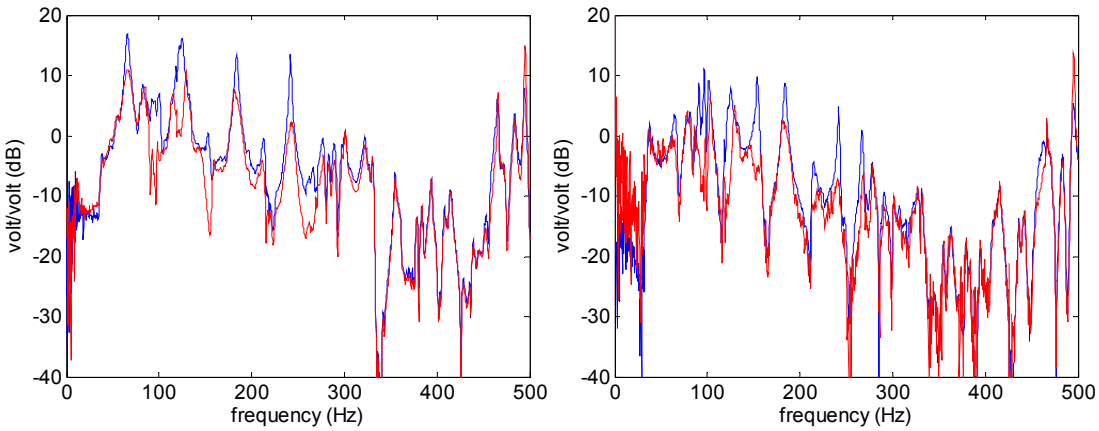

Figure C.13. Magnitude plots (blue) of the transfer functions for the payload fairing overlaid by the closed-loop controlled magnitude (red) of the transfer functions.

Appendix D

Additional Adaptive Control Results

Figures D.1 through D.13 show the magnitudes of the transfer functions for the three measurement locations as the duct is decreased from 72 to 60 inches with the baseline measurement in blue, the non-adaptive control measurement in red, and the adaptive control results in black. The disturbance signal and the control signal are overlaid on the same speaker for these figures. The ordinate for each figure is the voltage of the microphone over the voltage of the disturbance input from Siglab in decibels. The abscissa is the frequency in Hz from 0 to 500 Hz.

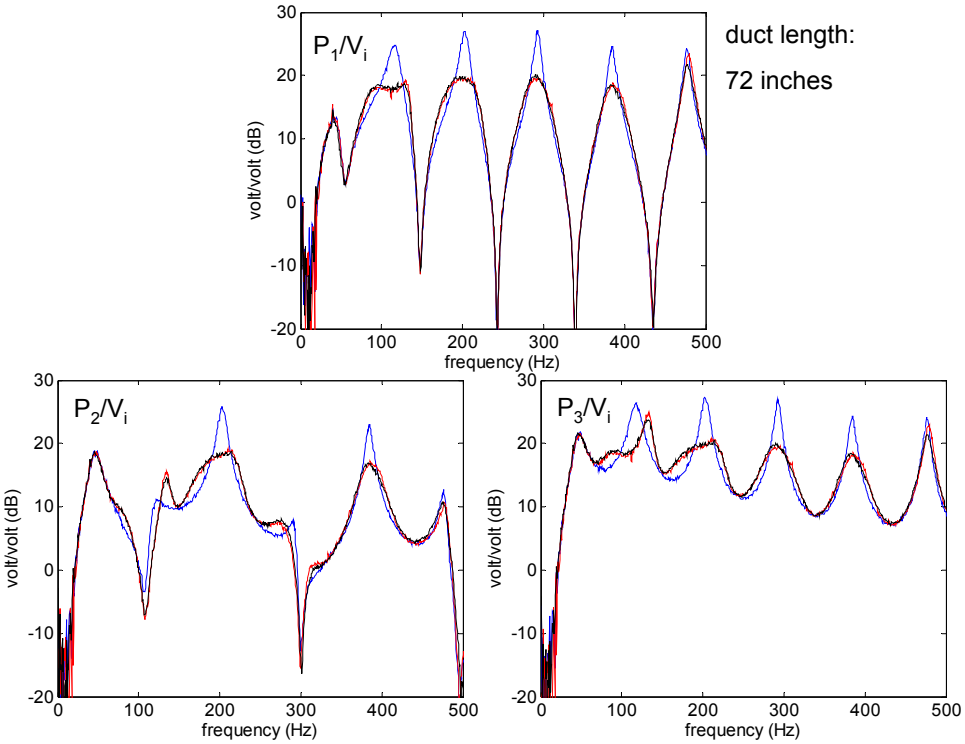

Figure D.1. Magnitude of the measured transfer functions (blue) of the duct with the measured non-adaptive controlled closed-loop transfer function (red) and the measured adaptive controlled closed-loop transfer function (black) overlaid on top.

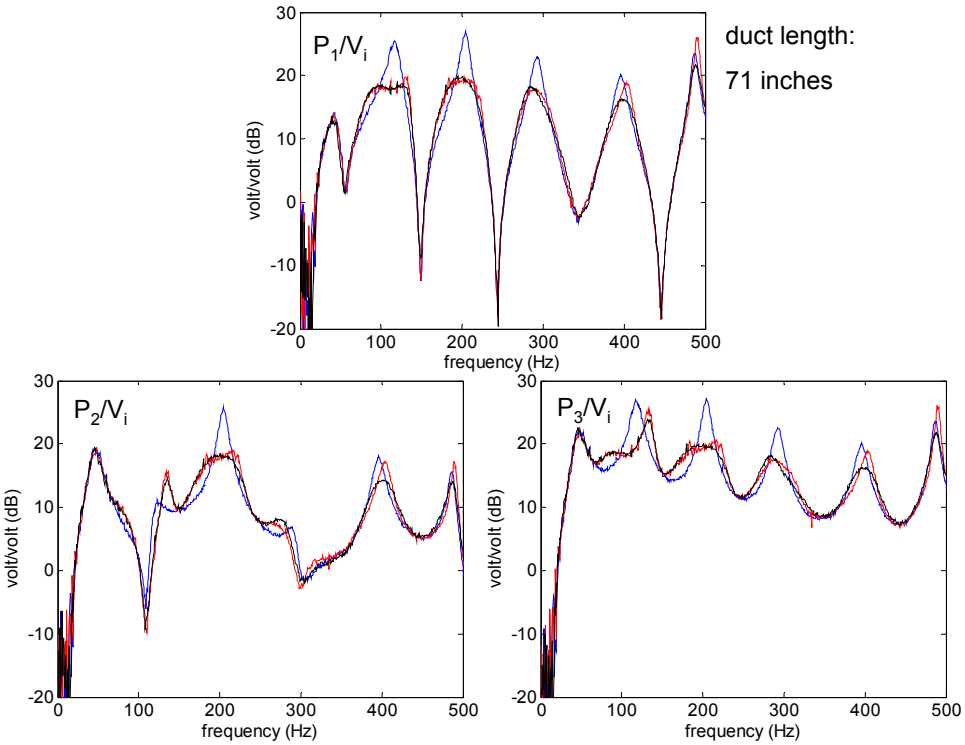

Figure D.2. Magnitude of the measured transfer functions (blue) of the duct with the measured non-adaptive controlled closed-loop transfer function (red) and the measured adaptive controlled closed-loop transfer function (black) overlaid on top.

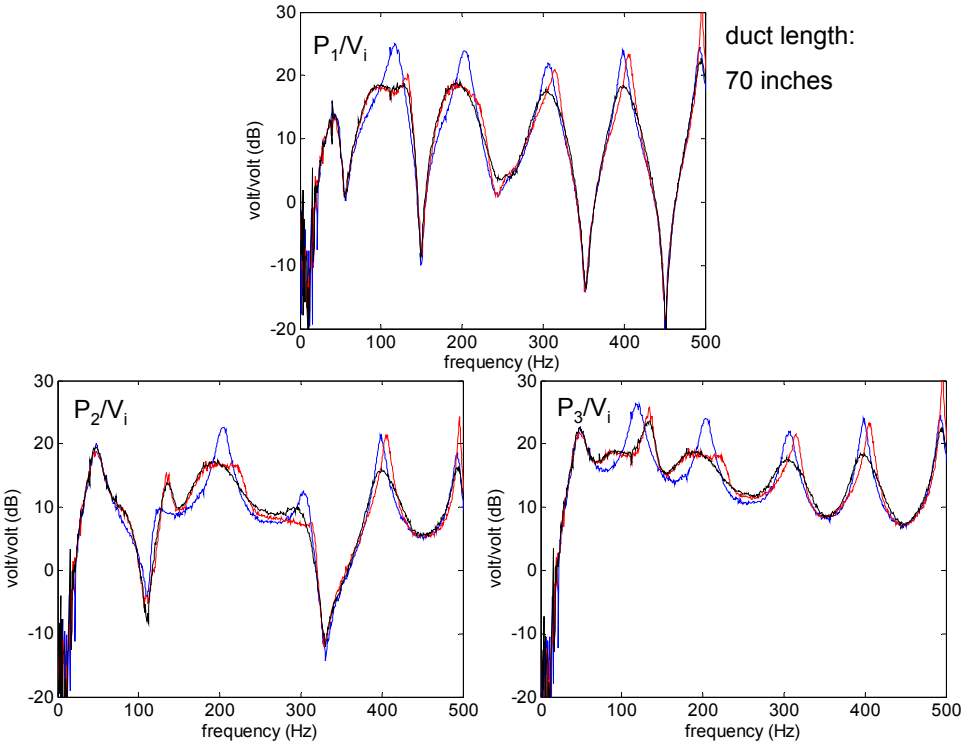

Figure D.3. Magnitude of the measured transfer functions (blue) of the duct with the measured non-adaptive controlled closed-loop transfer function (red) and the measured adaptive controlled closed-loop transfer function (black) overlaid on top.

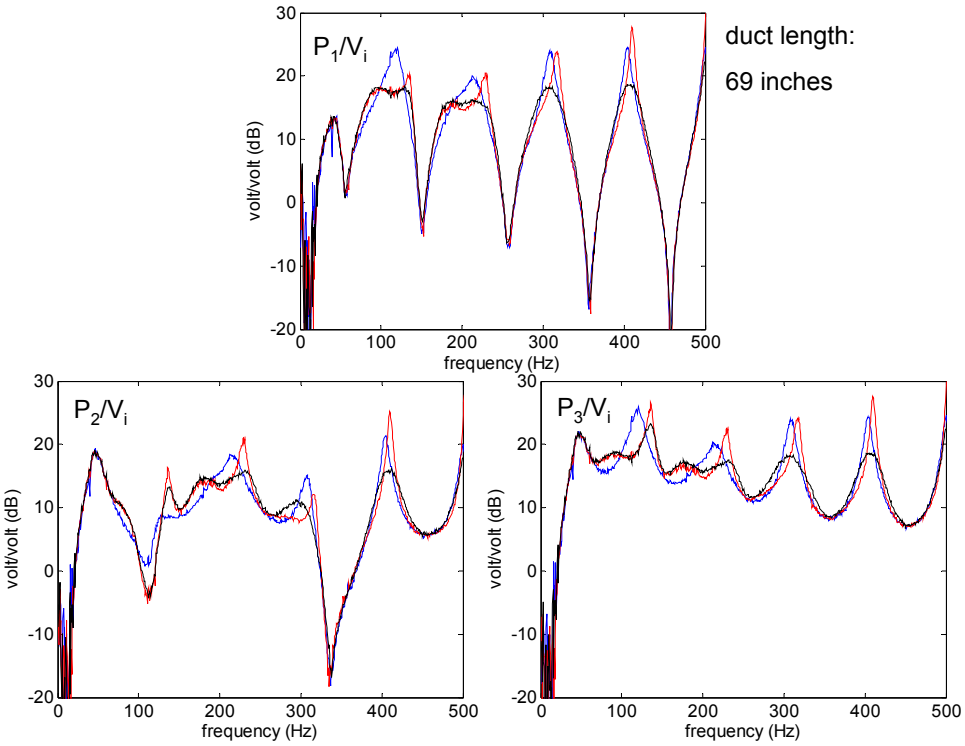

Figure D.4. Magnitude of the measured transfer functions (blue) of the duct with the measured non-adaptive controlled closed-loop transfer function (red) and the measured adaptive controlled closed-loop transfer function (black) overlaid on top.

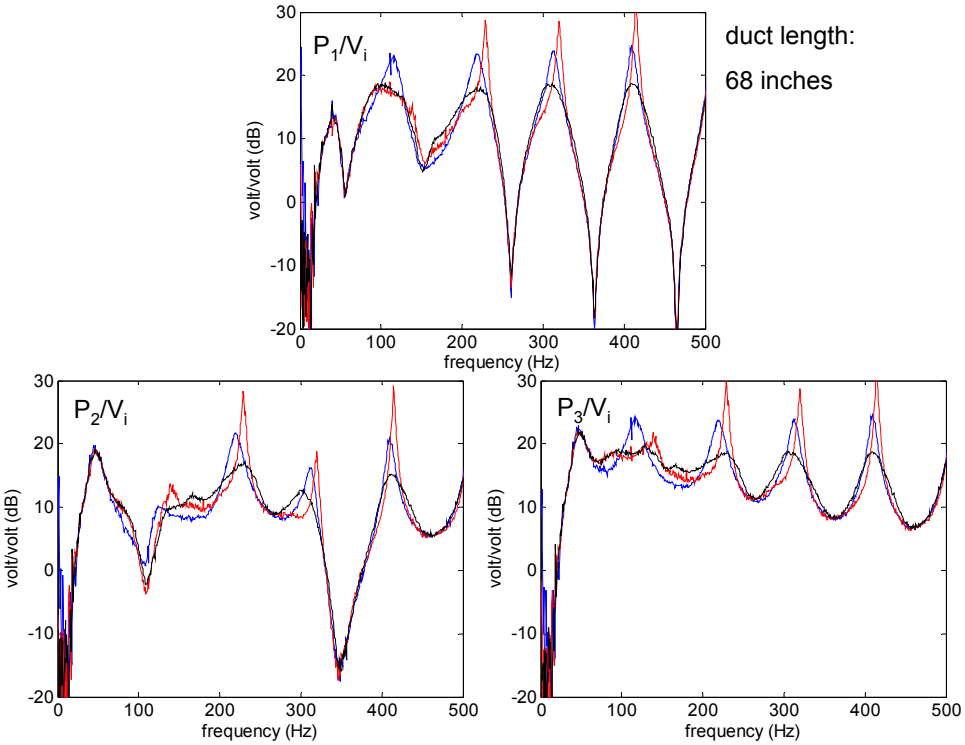

Figure D.5. Magnitude of the measured transfer functions (blue) of the duct with the measured non-adaptive controlled closed-loop transfer function (red) and the measured adaptive controlled closed-loop transfer function (black) overlaid on top.

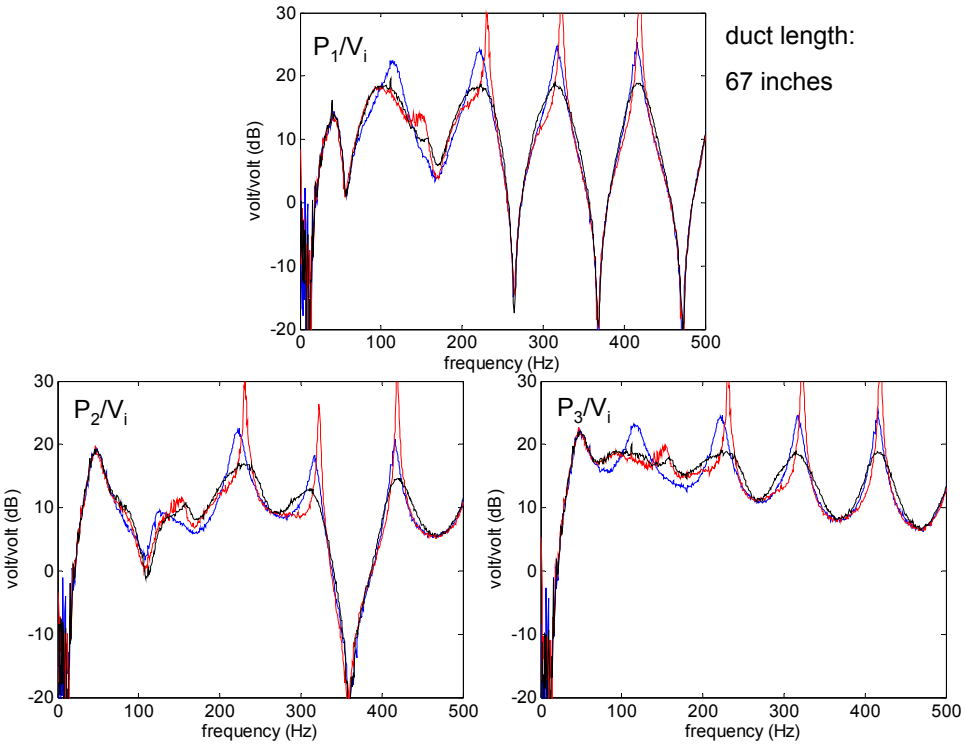

Figure D.6. Magnitude of the measured transfer functions (blue) of the duct with the measured non-adaptive controlled closed-loop transfer function (red) and the measured adaptive controlled closed-loop transfer function (black) overlaid on top.

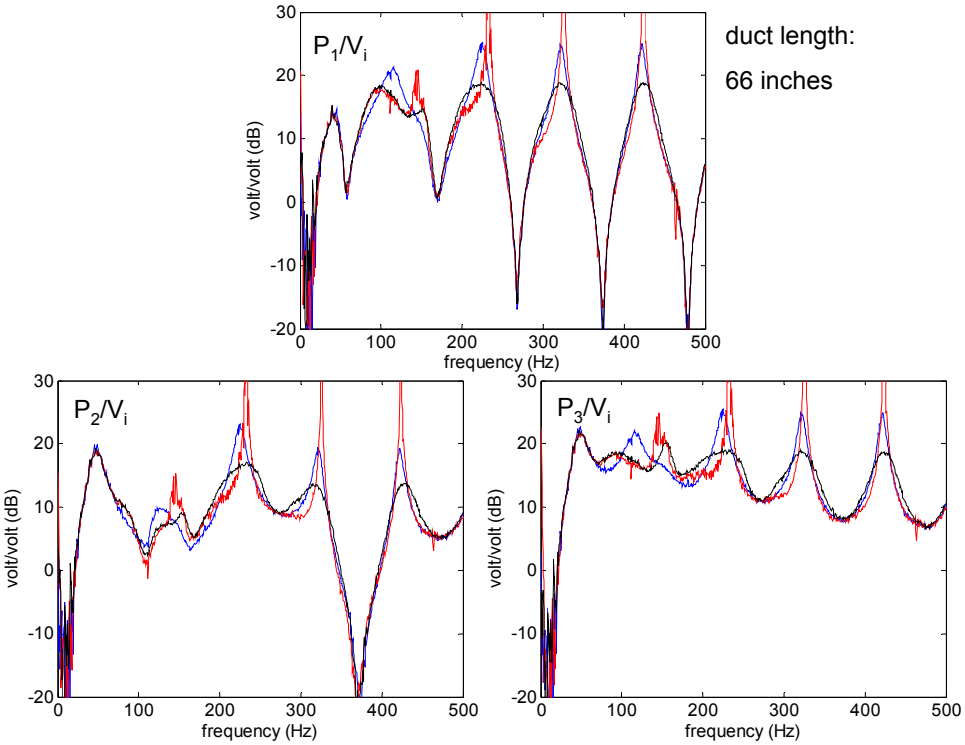

Figure D.7. Magnitude of the measured transfer functions (blue) of the duct with the measured non-adaptive controlled closed-loop transfer function (red) and the measured adaptive controlled closed-loop transfer function (black) overlaid on top.

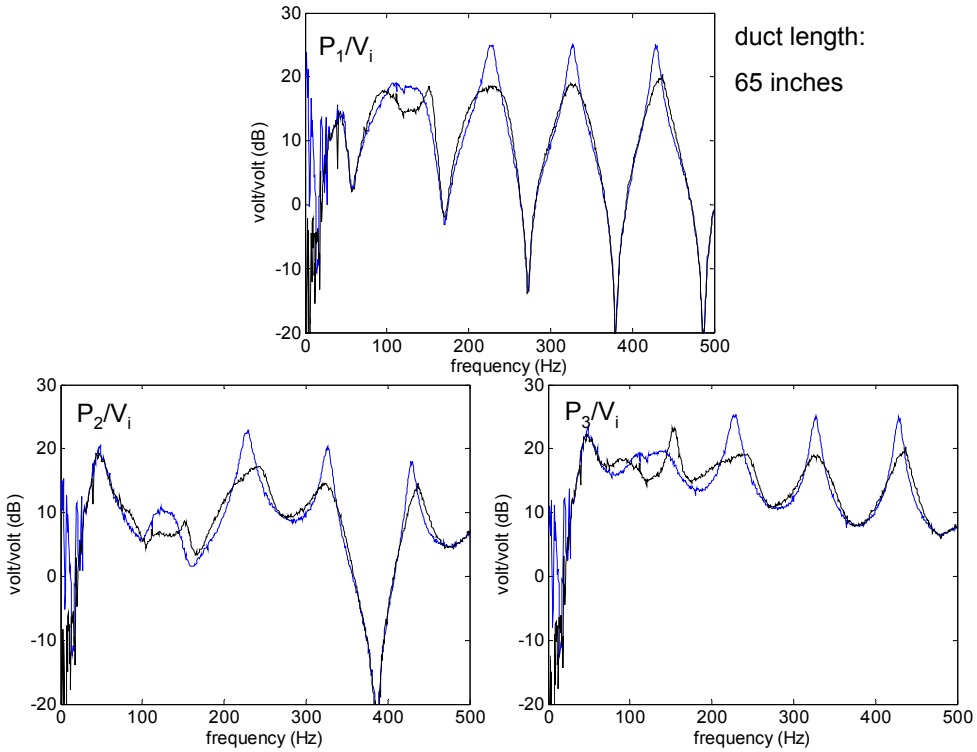

Figure D.8. Magnitude of the measured transfer functions (blue) of the duct with the measured adaptive controlled closed-loop transfer function (black) overlaid on top.

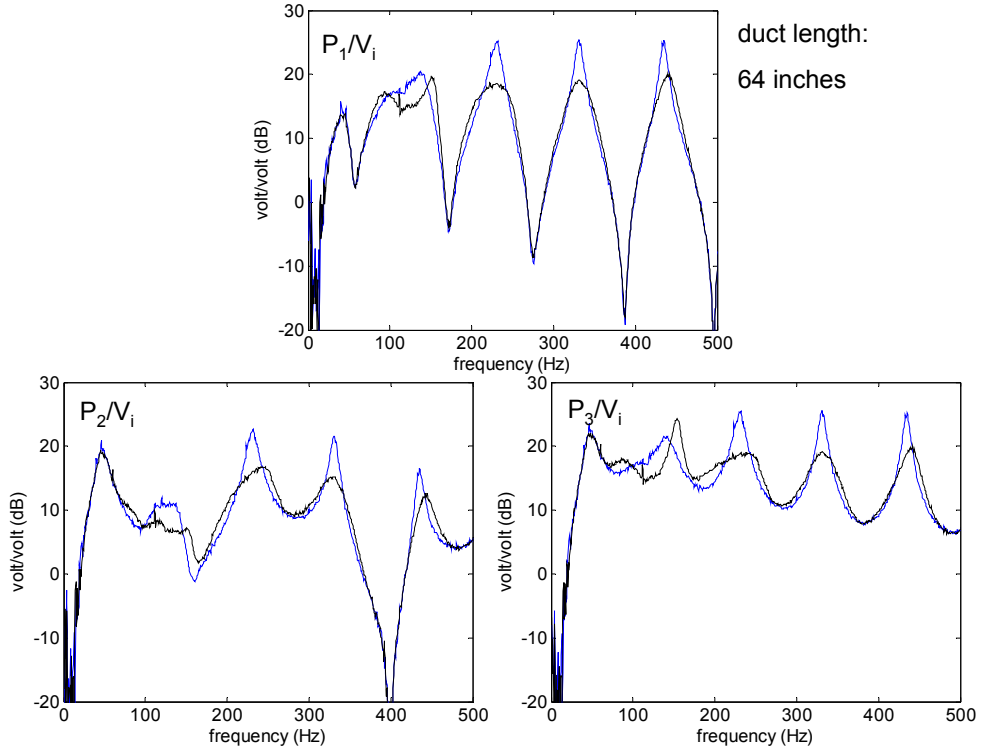

Figure D.9. Magnitude of the measured transfer functions (blue) of the duct with the measured adaptive controlled closed-loop transfer function (black) overlaid on top.

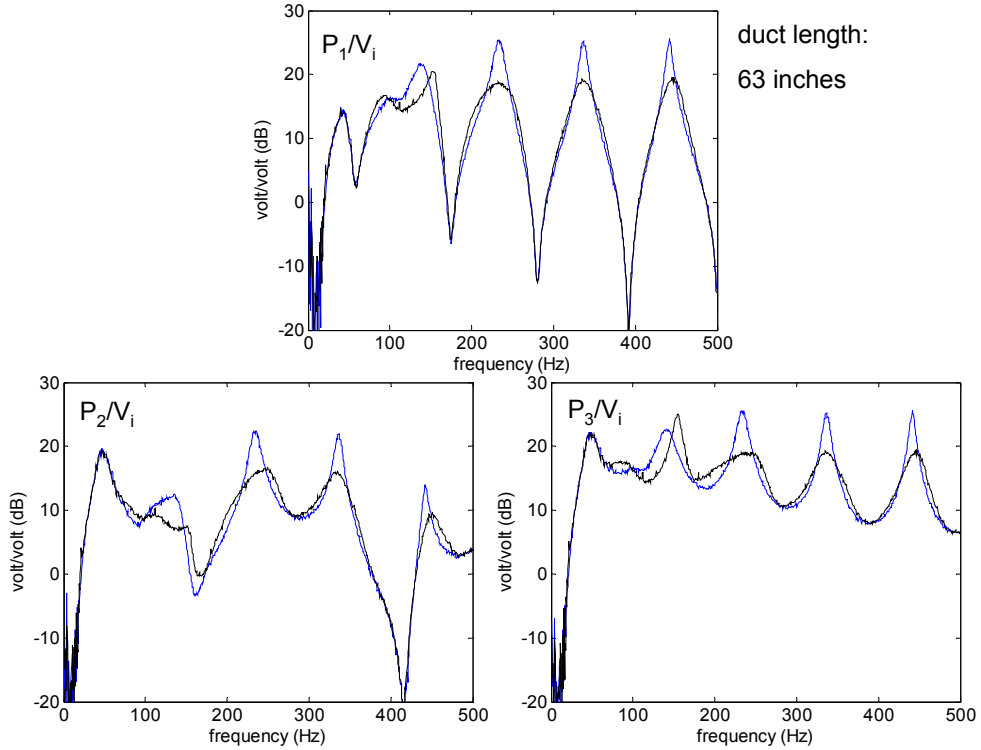

Figure D.10. Magnitude of the measured transfer functions (blue) of the duct with the measured adaptive controlled closed-loop transfer function (black) overlaid on top.

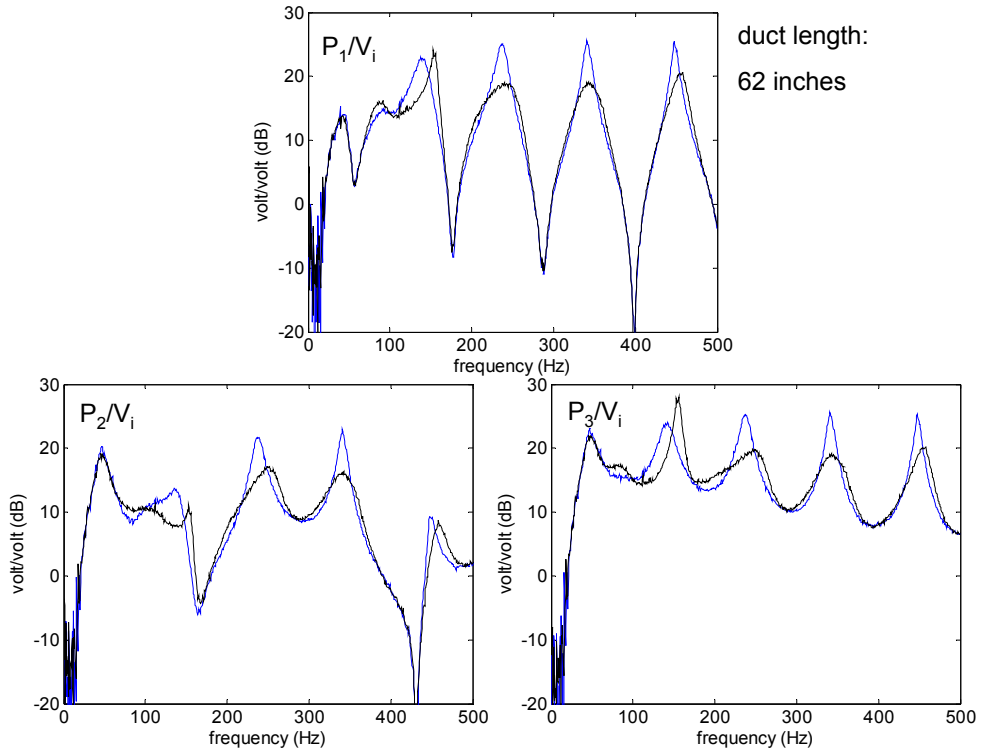

Figure D.11. Magnitude of the measured transfer functions (blue) of the duct with the measured adaptive controlled closed-loop transfer function (black) overlaid on top.

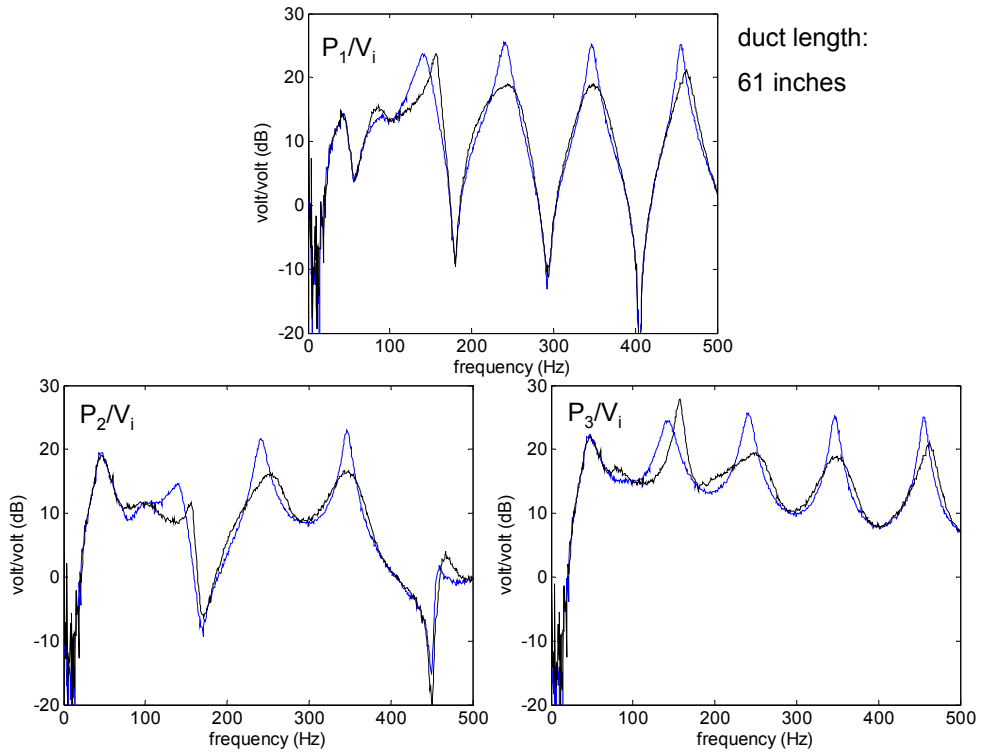

Figure D.12. Magnitude of the measured transfer functions (blue) of the duct with the measured adaptive controlled closed-loop transfer function (black) overlaid on top.

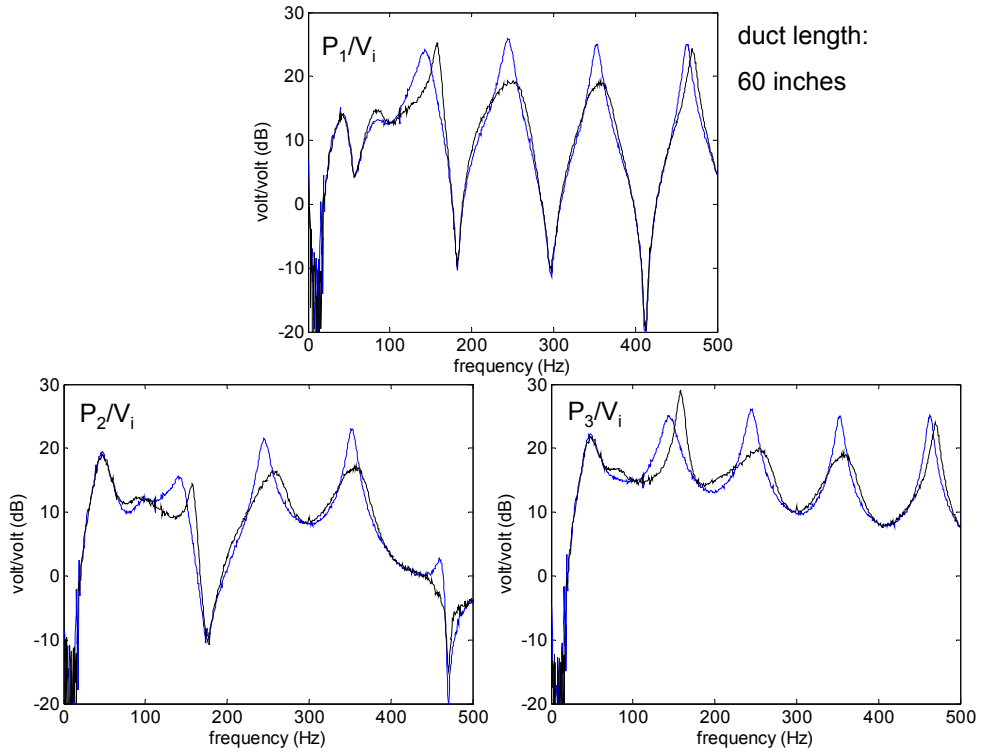

Figure D.13. Magnitude of the measured transfer functions (blue) of the duct with the measured adaptive controlled closed-loop transfer function (black) overlaid on top.

Figures D.14 through D.26 show the magnitudes of the transfer functions for the three measurement locations as the duct length is decreased from 72 to 60 inches with the baseline measurement in blue, the non-adaptive control measurement in red, and the adaptive control results in black. The disturbance signal is sent to an external actuator source these figures. The ordinate for each figure is the voltage of the microphone over the voltage of the disturbance input from Siglab in decibels. The abscissa is the frequency in Hz from 0 to 500 Hz.

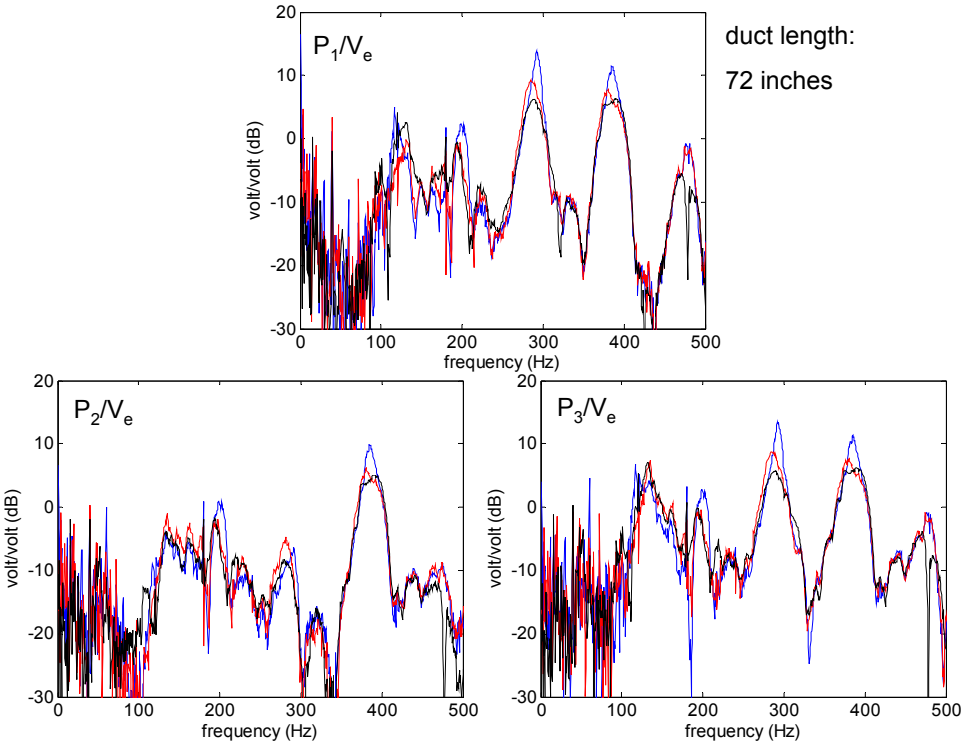

Figure D.14. Magnitude of the measured transfer functions (blue) of the duct with the measured non-adaptive controlled closed-loop transfer function (red) and the measured adaptive controlled closed-loop transfer function (black) overlaid on top.

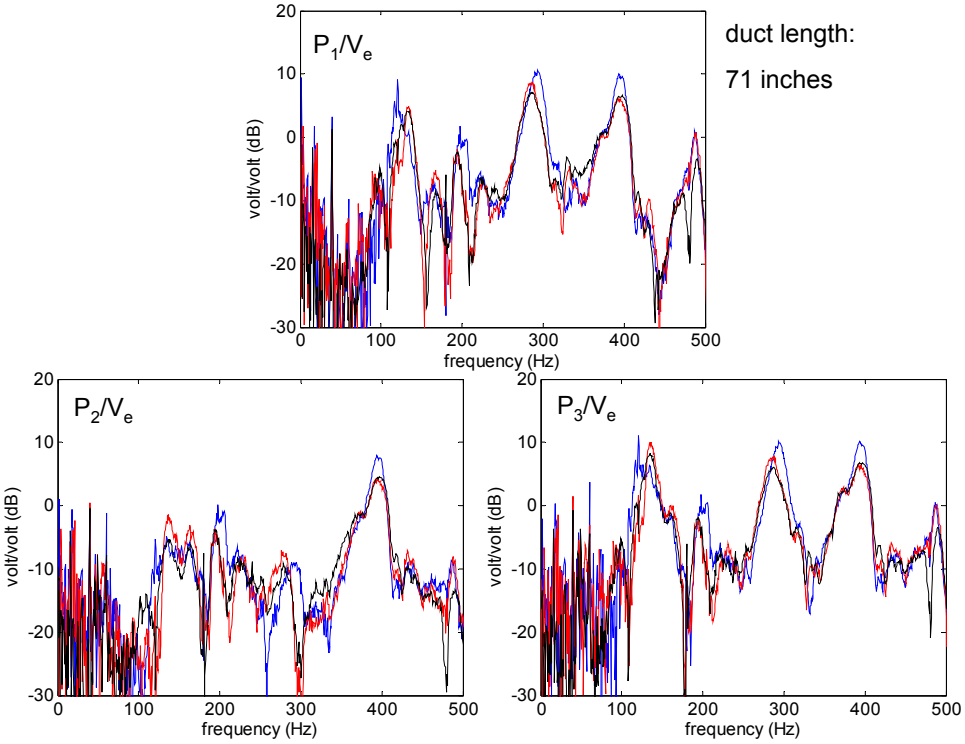

Figure D.15. Magnitude of the measured transfer functions (blue) of the duct with the measured non-adaptive controlled closed-loop transfer function (red) and the measured adaptive controlled closed-loop transfer function (black) overlaid on top.

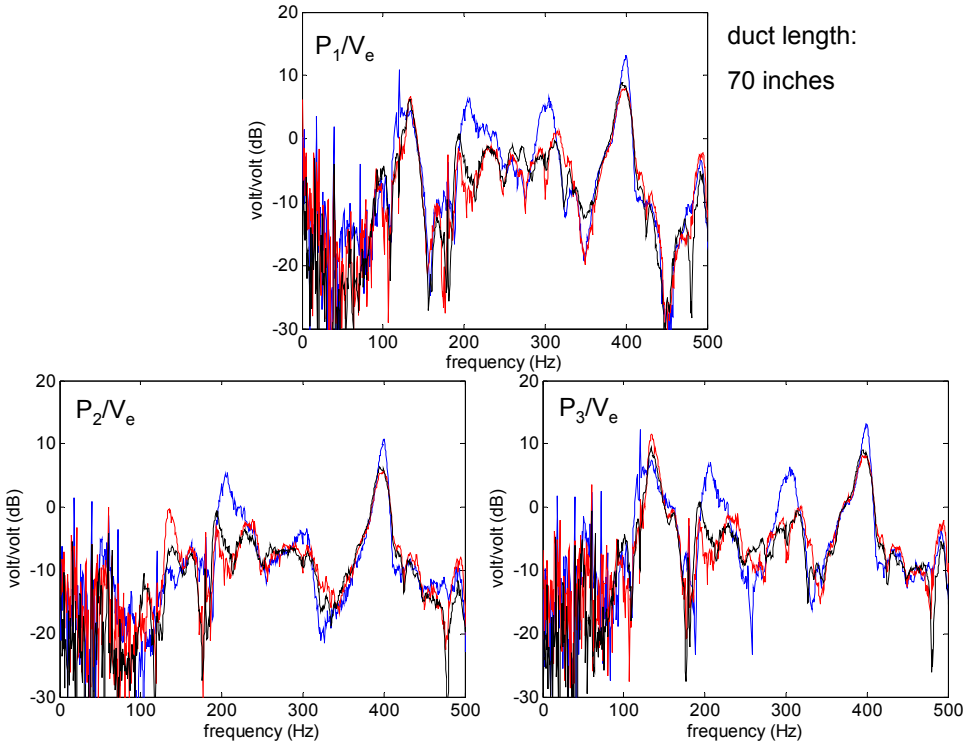

Figure D.16. Magnitude of the measured transfer functions (blue) of the duct with the measured non-adaptive controlled closed-loop transfer function (red) and the measured adaptive controlled closed-loop transfer function (black) overlaid on top.

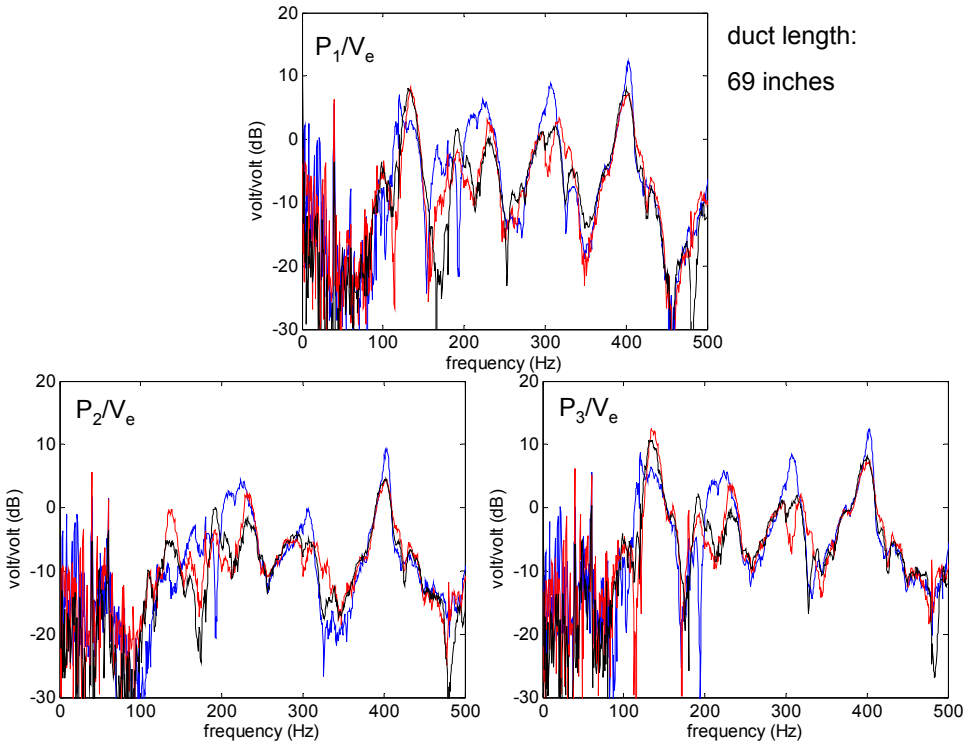

Figure D.17. Magnitude of the measured transfer functions (blue) of the duct with the measured non-adaptive controlled closed-loop transfer function (red) and the measured adaptive controlled closed-loop transfer function (black) overlaid on top.

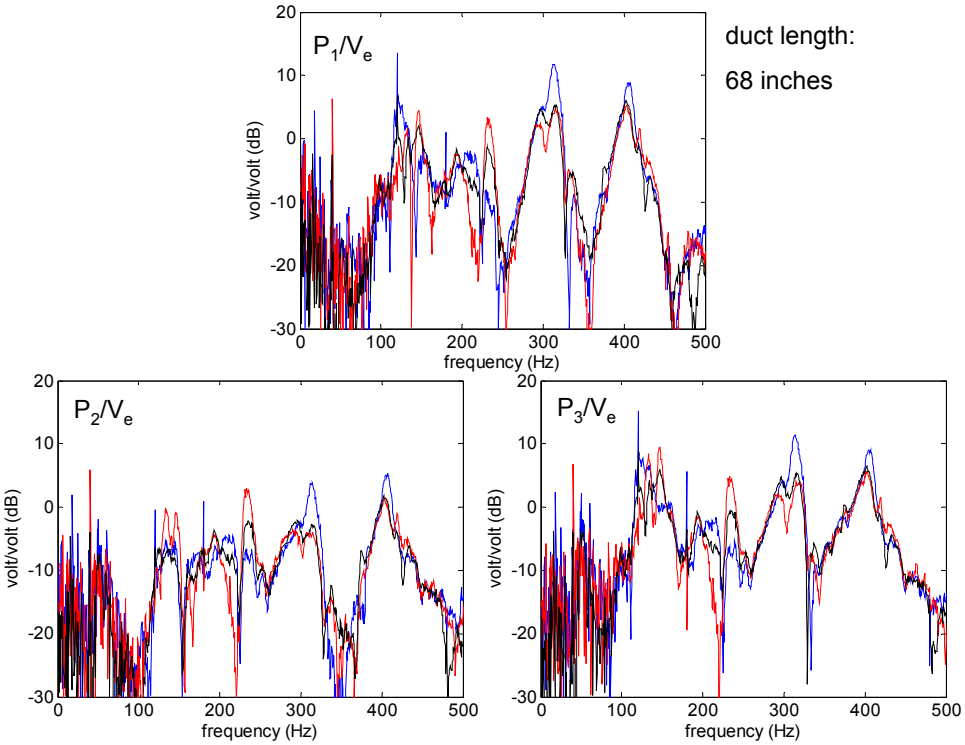

Figure D.18. Magnitude of the measured transfer functions (blue) of the duct with the measured non-adaptive controlled closed-loop transfer function (red) and the measured adaptive controlled closed-loop transfer function (black) overlaid on top.

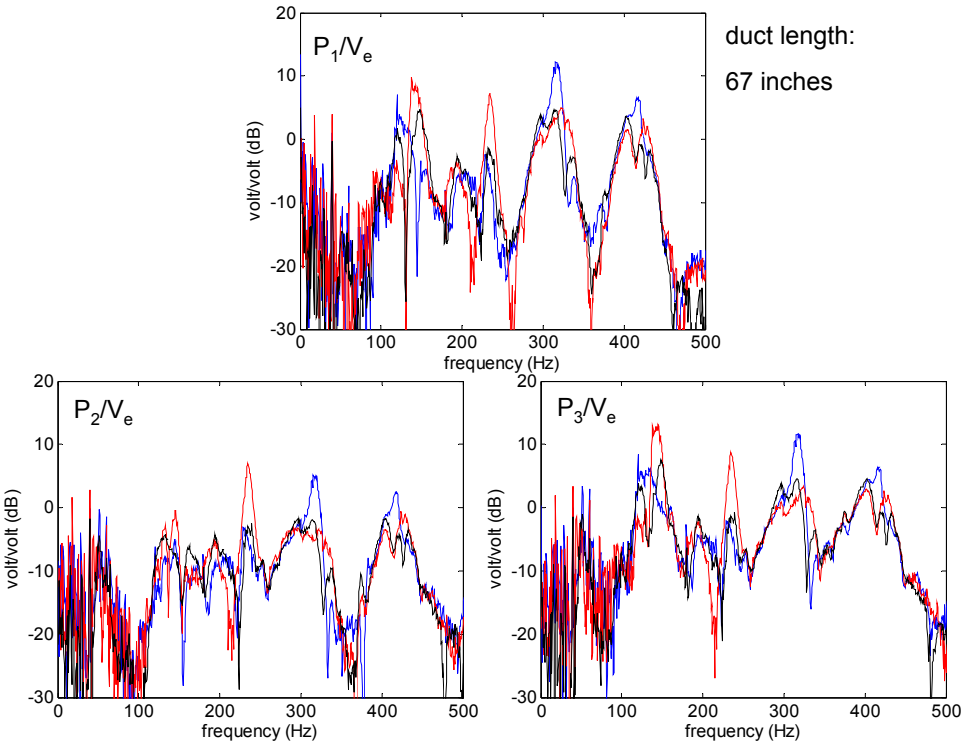

Figure D.19. Magnitude of the measured transfer functions (blue) of the duct with the measured non-adaptive controlled closed-loop transfer function (red) and the measured adaptive controlled closed-loop transfer function (black) overlaid on top.

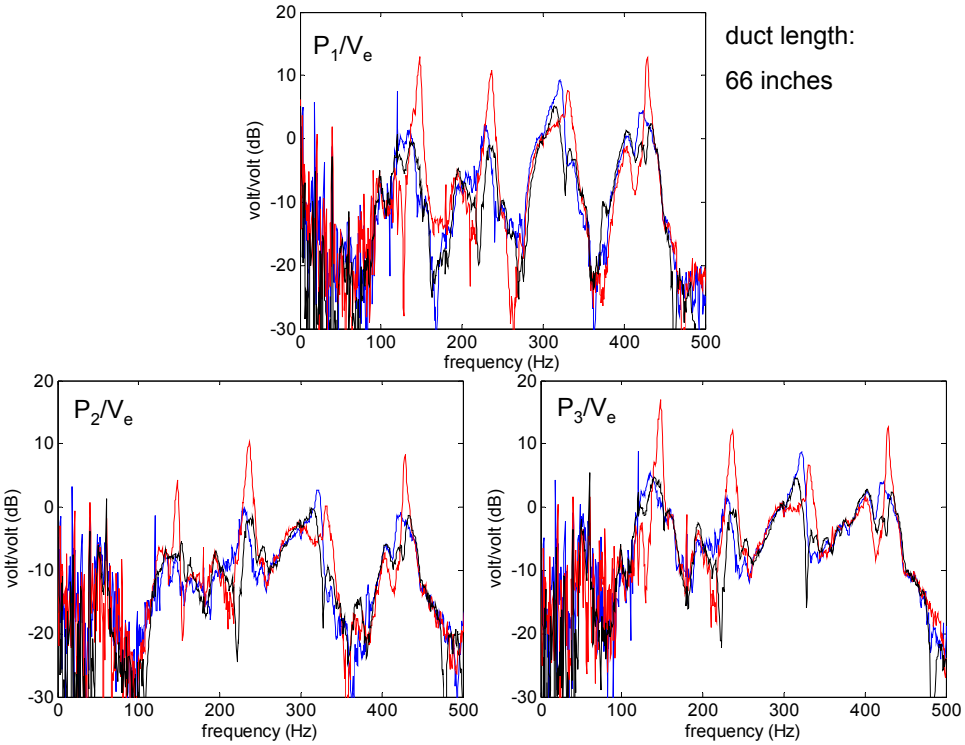

Figure D.20. Magnitude of the measured transfer functions (blue) of the duct with the measured non-adaptive controlled closed-loop transfer function (red) and the measured adaptive controlled closed-loop transfer function (black) overlaid on top.

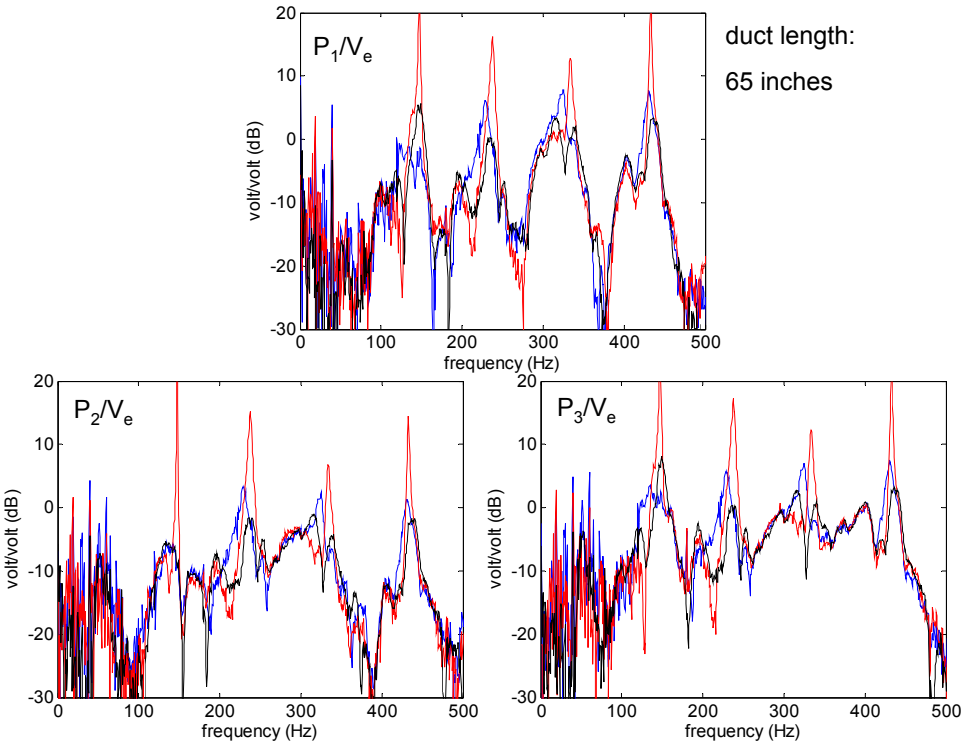

Figure D.21. Magnitude of the measured transfer functions (blue) of the duct with the measured non-adaptive controlled closed-loop transfer function (red) and the measured adaptive controlled closed-loop transfer function (black) overlaid on top.

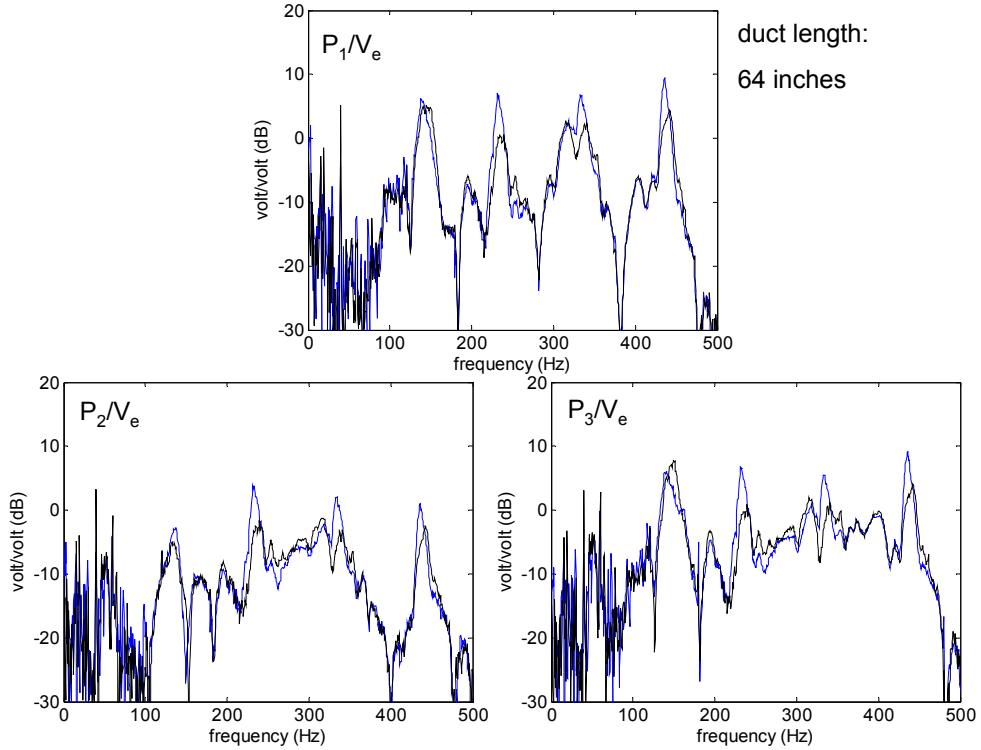

Figure D.22. Magnitude of the measured transfer functions (blue) of the duct with the measured adaptive controlled closed-loop transfer function (black) overlaid on top.

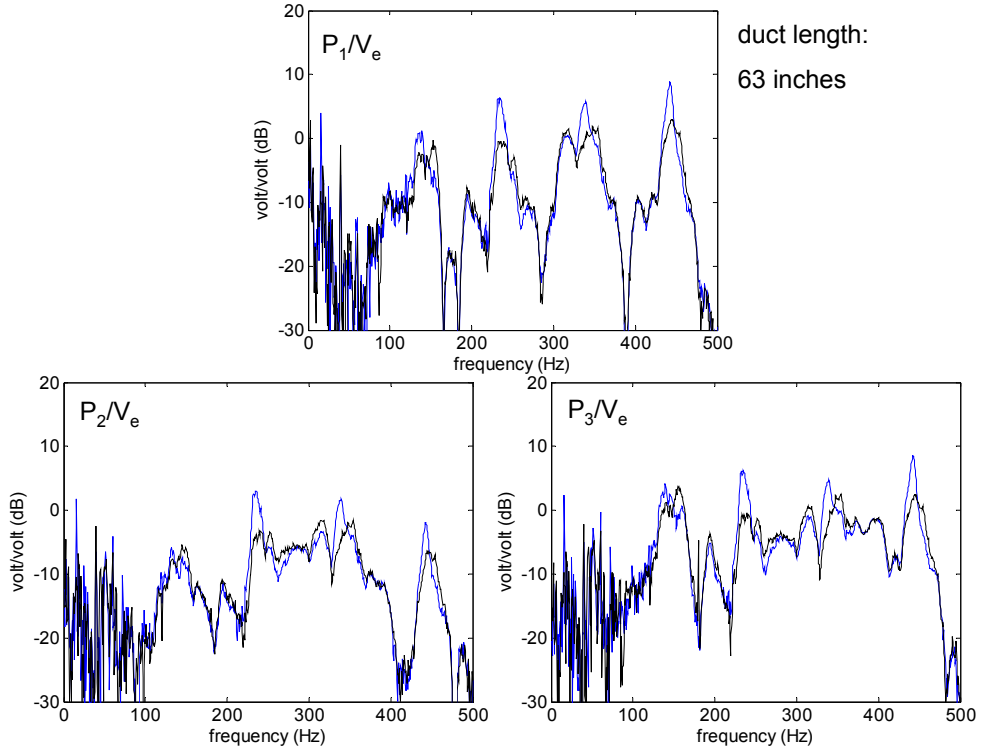

Figure D.23. Magnitude of the measured transfer functions (blue) of the duct with the measured adaptive controlled closed-loop transfer function (black) overlaid on top.

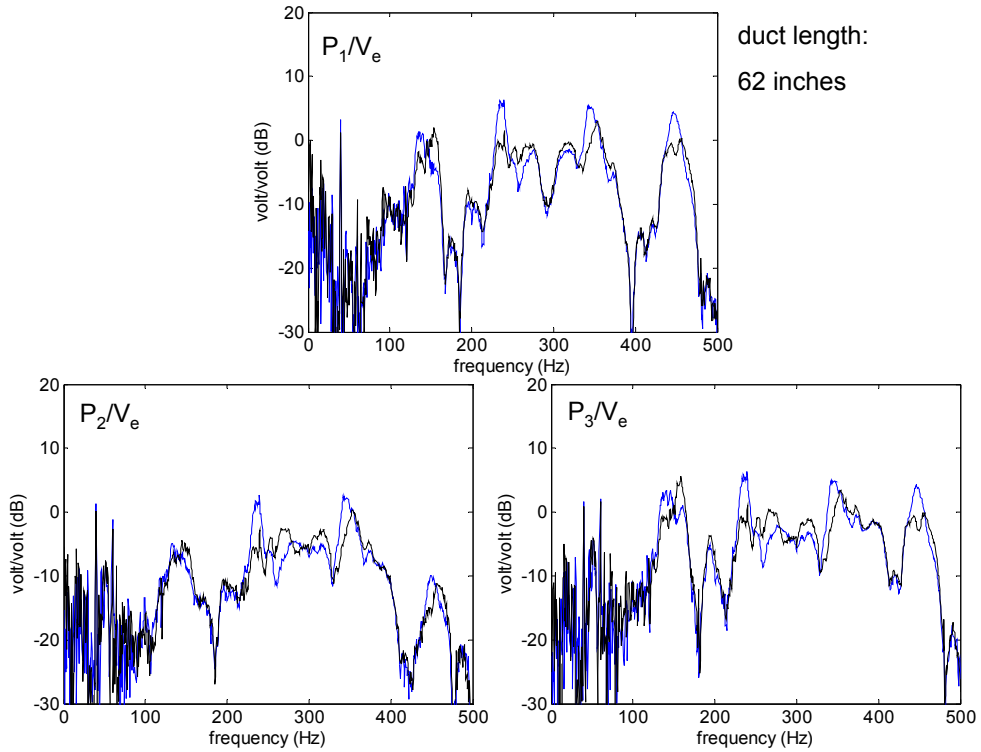

Figure D.24. Magnitude of the measured transfer functions (blue) of the duct with the measured adaptive controlled closed-loop transfer function (black) overlaid on top.

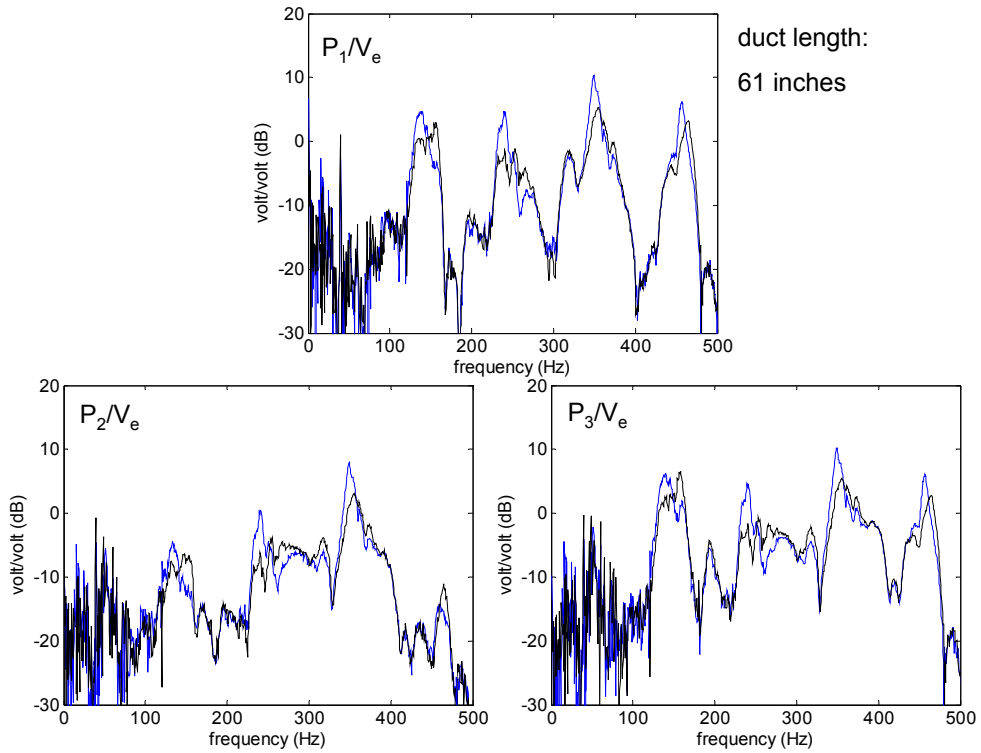

Figure D.25. Magnitude of the measured transfer functions (blue) of the duct with the measured adaptive controlled closed-loop transfer function (black) overlaid on top.

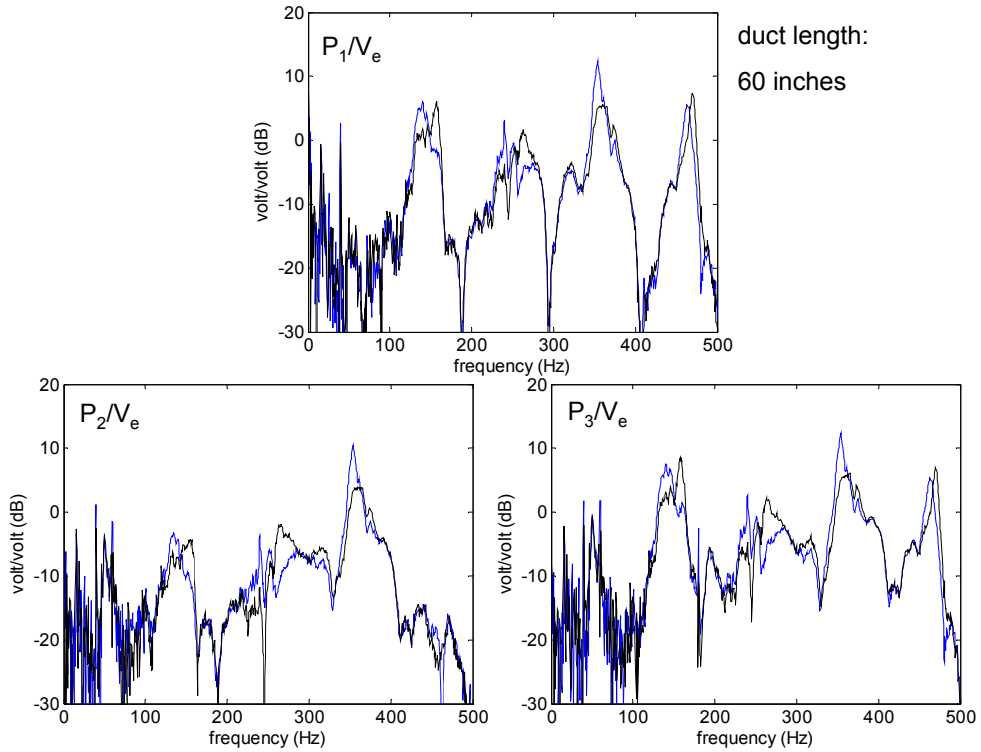

Figure D.26. Magnitude of the measured transfer functions (blue) of the duct with the measured adaptive controlled closed-loop transfer function (black) overlaid on top.

Appendix E

Code and Simulink Models

E.1 Matlab Code Used to Generate the Analytical Model

```
close all;
clear all;

start = 1.1;
last = 500;
division = 0.5;
f = [start:division:last];
omega = 2.*pi.*f;

%properties of the air
    rho = 1.1877;                           %density of air kg/m^3
    c = 345.25;                             %speed of sound in m/s
    k1 = omega./c;                          %real part of wave number

%cylinder properties
    diameter = 8;                            %diameter in inches
    S = ((diameter.*0.0254)./2).^2.*pi;      %area in m^2
    L = 71.9.*0.0254;                        %length of cylinder in m

%speaker properties
    m_speaker = 0.01838;                    %mass of the speaker in kg
    mechanical_compliance = 1174.63;        %compliance in UM/N
    s = (mechanical_compliance.*10.^-6).^-1;%stiffness in N/m
    zeta = 1;                               %damping ratio of speaker
    R = zeta*2*sqrt(s*m_speaker);           %damping of speaker in kg/s
    Re = 6.6;                               %electrical resistance
    inductance = 0.93.*10.^-3;              %electrical impedance
    Bl = 6.77;                        %length of coil and magnetic field

%mass loading of air
    m_air = 8.*((diameter.*0.0254)./2).^3.*rho./c;   %mass of air in kg
    m = m_speaker + m_air;                      %total mass of speaker

%absorption values of the cylinder

    %spatial absorption coefficient
        eta = 1.88.*10^-5;      %coefficient of shear viscosity in Pa-s
        eta_B = 0;              %coefficient of bulk viscosity
        tau_s = (4./3.*eta + eta_B)./(rho.*c.^2);   %relaxation time
        alpha_sac = 0.5.*omega./c.*omega.*tau_s;

    %thermal conduction absorption coefficient
        gamma = 1.402;            %ratios of specific heats
        kappa = 0.0263;           %thermal conductivity in W/(m K)
        Cp = 1.01.*10.^3;         %specific heat at constant pressure
        alpha_kappa = omega.^2./(2.*rho.*c.^3).*(gamma - 1).*kappa./Cp;
```

```
    %molecular thermal relaxation coefficient
        T_01 = 273.16;
        T_0 = 273.15;
        T = 295.15;
        p_s = 100677.32;
        p_s0 = 101325;
        value = -6.8346.*(T_01./T).^1.261 + 4.6151;
        p_sat = p_s0.*10.^value;
        hr = 50;
        h = hr.*(p_sat./p_s0)./(p_s./p_s0);
        F_rN = 1./p_s0.*(T_0./T).^0.5.*(9 + 280.*h.*exp(-
       4.17.*((T_0./T).^(1./3) - 1)));
        f_rN = F_rN.*p_s;
        F_r0 = 1./p_s0.*(24 + 4.04.*10.^4.*h.*(0.02 + h)./(0.391 + h));
        f_r0 = F_r0.*p_s;
        F1 = f./p_s;
        alpha_molecular = f.^2.*((1.84.*10.^-11).*(p_s./p_s0).^-
       1.*(T./T_0).^0.5 + (T./T_0).^(-5./2).*((1.278.*10.^-
       2).*exp(-2239.1./T)./(f_r0 + f.^2./f_r0) + (1.068.*10.^-
       1).*exp(-3352./T)./(f_rN + f.^2./f_rN)));

    %absorption of the cylinder
        Pr = 0.710;                             %Prandtl number
        a = (diameter.*0.0254)./2;              %radius of cylinder in m
        alpha_w = 1./(a.*c).*(eta.*omega./(2.*rho)).^0.5.*(1 + (gamma -
       1)./sqrt(Pr));

    %total absorption
         %alpha = (alpha_sac + alpha_kappa + alpha_w).*6; %classical
        alpha = (alpha_molecular + alpha_w).*10;

k = k1 - i.*alpha;
% k = k1;      %removing the absorption coefficient

%impedances

    %acoustical
        Za = -i.*rho.*c.*S.*cot(k.*L);          %acoustical impedance

    %mechanical
        Zm = R + i.*(omega.*m - s./omega);      %mechanical impedance

    %electrical
        Ze = Re + i.*omega.*inductance;         %electrical impedance

        Z = Za + Zm;

%input
    voltage_rms = 0.05;
    voltage = voltage_rms.*sqrt(2);
    Z_total = Ze + (Zm + S.^2.*Za)./Bl.^2;
    current = voltage./Z_total;
    F = Bl.*current;


[B,A] = butter(1,300,'high','s');
sys = tf(B,A);
% sys = tf([1],[1]); %removing the butterworth filter
[mag,phase1]=bode((sys),2*pi*f);
mag = mag(:);     phase1 = phase1(:);
H = reshape(mag.*exp(i*phase1*pi/180),1,[]);
figure
bode(sys) %bode plot of the fudge factor from above

%pressure calculations

    %end
        place_end = L - 0.02;
        p_end = F./S.*Za./Z.*cos(k.*(L - place_end))./cos(k.*L);

    %front
```

```
        place_front = 0 + 0.05;
        p_front = F./S.*Za./Z.*cos(k.*(L - place_front))./cos(k.*L);

    %middle
        place_middle = 0.97;
        p_middle = F./S.*Za./Z.*cos(k.*(L - place_middle))./cos(k.*L);

pref = 2*10^-5;

load baseline00.vna -mat
freq = SLm.fdxvec;
freq = freq(1,49:1601);
G = SLm.xcmeas(1,2).xfer;
G = G(49:1601,1);
G1 = SLm.xcmeas(1,3).xfer;
G1 = G1(49:1601,1);
G2 = SLm.xcmeas(1,4).xfer;
G2 = G2(49:1601,1);


   figure
   set(gca,'Fontname','TimesNewRoman','Fontsize',14)
   plot(freq,20.*log10(abs(G2)),f,20.*log10(abs(H.*p_end)./pref)-80)
   xlabel('frequency (Hz)')
   ylabel('volt/volt (dB)')
   axis([0 500 0 30])

   figure
   set(gca,'Fontname','TimesNewRoman','Fontsize',14)
   plot(freq,phase(G2).*180./pi+353,f,phase(H.*p_end).*180./pi)
   xlabel('frequency (Hz)')
   ylabel('phase (degree)')
   axis([0 500 -1200 200])

   figure
   set(gca,'Fontname','TimesNewRoman','Fontsize',14)
   plot(freq,20.*log10(abs(G)),f,20.*log10(abs(H.*p_front)./pref)-80)
   xlabel('frequency (Hz)')
   ylabel('volt/volt (dB)')
   axis([0 500 -20 30])

   figure
   set(gca,'Fontname','TimesNewRoman','Fontsize',14)
   plot(freq,phase(G).*180./pi,f,phase(H.*p_front).*180./pi)
   xlabel('frequency (Hz)')
   ylabel('phase (degree)')
   axis([0 500 -300 200])

   figure
   set(gca,'Fontname','TimesNewRoman','Fontsize',14)
   plot(freq,20.*log10(abs(G1)),f,20.*log10(abs(H.*p_middle)./pref)-80)
   xlabel('frequency (Hz)')
   ylabel('volt/volt (dB)')
   axis([0 500 -20 30])

   figure
   set(gca,'Fontname','TimesNewRoman','Fontsize',14)
   plot(freq,phase(G1).*180./pi,f,phase(H.*p_middle).*180./pi)
   xlabel('frequency (Hz)')
   ylabel('phase (degree)')
   axis([0 500 -800 200])
```

E.2 Function Used to Find Poles, Zeros, and Damping Ratios

```
function [poles,zeros,damping] = pole_zero_damping_analytical(f,G)

f_vec = f;
[con,max_f_num] = size(f_vec);     %finding the maximum frequency value
```

```
f_vec = reshape(f_vec,[],1);       %reshaping the frequency vector

y = 0.5;     %finding the frequency step size

pole_max = 6;              %maximum number of poles to find
p = 1;
f1 = 20.2;
aa = find(f_vec==f1);
G1 = G;

%finding the pole locations
while p <= pole_max

    while abs(G(aa)) < abs(G(aa+1))
        f1 = f1 + y;
            if abs(G(aa + 1)) > abs(G(aa + 2))
                if abs(G(aa + 1)) > abs(G(aa + 3))
                    if abs(G(aa + 1)) > abs(G(aa - 1))
                        if abs(G(aa + 1)) > abs(G(aa - 2))
                            freq(p) = f_vec(aa + 1);
                            p = p + 1;
                        end
                    end
                end
            end

        aa = find(f_vec==f1);
        if f1 > 498.2
            G(aa) = 1;
            G(aa + 1) = 0;
            p = 7;
        end
    end
    while abs(G(aa)) > abs(G(aa+1))
        f1 = f1 + y;
        aa = find(f_vec==f1);
        if f1 > 498.2
            G(aa) = 0;
            G(aa+1) = 1;
            p = 7;
        end
    end
end

poles = freq(1:6);
G = G1;
%finding the zeros
Gaa = G(find(f==freq(1)):find(f==freq(2)),1);
Gbb = G(find(f==freq(2)):find(f==freq(3)),1);
Gcc = G(find(f==freq(3)):find(f==freq(4)),1);
Gdd = G(find(f==freq(4)):find(f==freq(5)),1);
Gee = G(find(f==freq(5)):find(f==freq(6)),1);
Gff = G(find(f==freq(6)):find(f==499.7),1);

z(1) = f(find(abs(G)==min(abs(Gaa))));
z(2) = f(find(abs(G)==min(abs(Gbb))));
z(3) = f(find(abs(G)==min(abs(Gcc))));
z(4) = f(find(abs(G)==min(abs(Gdd))));
z(5) = f(find(abs(G)==min(abs(Gee))));
z(6) = f(find(abs(G)==min(abs(Gff))));

zeros = z;

%finding the damping
u = 1;
while u < 7
    aa = find(f_vec==poles(u));
    bb = find(f_vec==poles(u));
    while abs(G(bb))./sqrt(2) < abs(G(aa + 1))
       aa = aa + 1;
       if abs(G(bb))./sqrt(2) >= abs(G(aa + 1))
```

```
            omega_b = f_vec(aa);
        end
    end
    aa = bb;
    while abs(G(bb))./sqrt(2) < abs(G(aa - 1))
        aa = aa - 1;
        if abs(G(bb))./sqrt(2) >= abs(G(aa - 1))
            omega_a = f_vec(aa);
        end
    end

    zeta(u) = (omega_b - omega_a)./(2.*poles(u));
    u = u + 1;
end
damping = zeta;
```

E.3 Automated Code for Setting Duct Controller

```
close all;
clear all;

load baseline.vna -mat;       % loading the baseline data of the system

f = SLm.fdxvec(1,10:1601);                              %frequency data
G = SLm.xcmeas(1,2).xfer(10:1601,1);                    % front plant tf
G1 = SLm.xcmeas(1,3).xfer(10:1601,1);                   % end plant tf
G2 = SLm.xcmeas(1,4).xfer(10:1601,1);
G3 = SLm.xcmeas(1,3).xfer(10:1601,1)./SLm.xcmeas(1,2).xfer(10:1601,1);    % end/front tf
G4 = SLm.xcmeas(1,4).xfer(10:1601,1)./SLm.xcmeas(1,2).xfer(10:1601,1);    % end/front tf

n = 1591;
aa = 1;
bb = 80;
cc = 264;
dd = 400;
ee = 536;
ff = 672;
gg = 808;
hh = 944;
ii = 1144;
jj = 1288;
kk = 1432;

Gaa = G(aa:bb,1);
Gbb = G(bb:cc,1);
Gcc = G(cc:dd,1);
Gdd = G(dd:ee,1);
Gee = G(ee:ff,1);
Gff = G(ff:gg,1);
Ggg = G(gg:hh,1);
Ghh = G(hh:ii,1);
Gii = G(ii:jj,1);
Gjj = G(jj:kk,1);
Gkk = G(kk:n,1);

poles(1) = f(find(abs(G)==max(abs(Gaa))));
poles(2) = f(find(abs(G)==max(abs(Gbb))));
poles(3) = f(find(abs(G)==max(abs(Gcc))));
poles(4) = f(find(abs(G)==max(abs(Gdd))));
poles(5) = f(find(abs(G)==max(abs(Gee))));
poles(6) = f(find(abs(G)==max(abs(Gff))));
poles(7) = f(find(abs(G)==max(abs(Ggg))));
poles(8) = f(find(abs(G)==max(abs(Ghh))));
poles(9) = f(find(abs(G)==max(abs(Gii))));
poles(10) = f(find(abs(G)==max(abs(Gjj))));
poles(11) = f(find(abs(G)==max(abs(Gkk))));
poles
```

```
Gaa = G(find(f==poles(1)):find(f==poles(2)),1);
Gbb = G(find(f==poles(2)):find(f==poles(3)),1);
Gcc = G(find(f==poles(3)):find(f==poles(4)),1);
Gdd = G(find(f==poles(4)):find(f==poles(5)),1);
Gee = G(find(f==poles(5)):find(f==poles(6)),1);
Gff = G(find(f==poles(6)):find(f==poles(7)),1);
Ggg = G(find(f==poles(7)):find(f==poles(8)),1);
Ghh = G(find(f==poles(8)):find(f==poles(9)),1);
Gii = G(find(f==poles(9)):find(f==poles(10)),1);
Gjj = G(find(f==poles(10)):find(f==poles(11)),1);
Gkk = G(find(f==poles(11)):n,1);

zeros(1) = f(find(abs(G)==min(abs(Gaa))));
zeros(2) = f(find(abs(G)==min(abs(Gbb))));
zeros(3) = f(find(abs(G)==min(abs(Gcc))));
zeros(4) = f(find(abs(G)==min(abs(Gdd))));
zeros(5) = f(find(abs(G)==min(abs(Gee))));
zeros(6) = f(find(abs(G)==min(abs(Gff))));
zeros(7) = f(find(abs(G)==min(abs(Ggg))));
zeros(8) = f(find(abs(G)==min(abs(Ghh))));
zeros(9) = f(find(abs(G)==min(abs(Gii))));
zeros(10) = f(find(abs(G)==min(abs(Gjj))));
zeros(11) = f(find(abs(G)==min(abs(Gkk))));
zeros
zeros = zeros - zeros.*.04

% Setting the gains for the controller
    g(1) = 0.0001;
    g(2) = 0.0001;
    g(3) = 0.0001;
    g(4) = 0.0001;
    g(5) = 0.0001;
    g(6) = 0.0001;
    g(7) = 0.0001;
    g(8) = 0.0001;
    g(9) = 0.0001;
% Setting the ppf controller filters
n = 2;
    freq = zeros(n) - poles(n).*0.0;
    omega = freq.*2.*pi;
    zeta = 0.08;
    num = [omega.^2];
    den = [1 2.*zeta.*omega omega.^2];
    sys = tf(num,den);
    [B,A] = butter(6,2*pi*[zeros(1,n-1)],'high','s');
    butter_sys = tf(B,A);
    [B,A] = butter(2,2*pi*([zeros(1,n+1)]),'low','s');
    butter_sys1 = tf(B,A);
    sys_t(n) = sys*butter_sys*butter_sys1;

n = 3;
    freq = zeros(n) - poles(n).*0.000;
    omega = freq.*2.*pi;
    zeta = 0.08;
    num = [omega.^2];
    den = [1 2.*zeta.*omega omega.^2];
    sys = tf(num,den);
    [B,A] = butter(6,2*pi*[zeros(1,n-1)],'high','s');
    butter_sys = tf(B,A);
    [B,A] = butter(2,2*pi*[zeros(1,n)],'low','s');
    butter_sys1 = tf(B,A);
    sys_t(n) = sys*butter_sys*butter_sys1;

 n = 4;
    freq = zeros(n) - poles(n).*0.000;
    omega = freq.*2.*pi;
    zeta = 0.08;
    num = [omega.^2];
    den = [1 2.*zeta.*omega omega.^2];
    sys = tf(num,den);
    [B,A] = butter(6,2*pi*[zeros(1,n-1)],'high','s');
```

```
    butter_sys = tf(B,A);
    [B,A] = butter(2,2*pi*[zeros(1,n)],'low','s');
    butter_sys1 = tf(B,A);
    sys_t(n) = sys*butter_sys*butter_sys1;

n = 5;
    freq = zeros(n) - poles(n).*0.000;
    omega = freq.*2.*pi;
    zeta = 0.08;
    num = [omega.^2];
    den = [1 2.*zeta.*omega omega.^2];
    sys = tf(num,den);
    [B,A] = butter(6,2*pi*[zeros(1,n-1)],'high','s');
    butter_sys = tf(B,A);
    [B,A] = butter(2,2*pi*[zeros(1,n)],'low','s');
    butter_sys1 = tf(B,A);
    sys_t(n) = sys*butter_sys*butter_sys1;

n = 6;
    freq = zeros(n) - poles(n).*0.000;
    omega = freq.*2.*pi;
    zeta = 0.08;
    num = [omega.^2];
    den = [1 2.*zeta.*omega omega.^2];
    sys = tf(num,den);
    [B,A] = butter(6,2*pi*[zeros(1,n-1)],'high','s');
    butter_sys = tf(B,A);
    [B,A] = butter(2,2*pi*[zeros(1,n)],'low','s');
    butter_sys1 = tf(B,A);
    sys_t(n) = sys*butter_sys*butter_sys1;

n = 7;
    freq = zeros(n) - poles(n).*0.000;
    omega = freq.*2.*pi;
    zeta = 0.08;
    num = [omega.^2];
    den = [1 2.*zeta.*omega omega.^2];
    sys = tf(num,den);
    [B,A] = butter(6,2*pi*[zeros(1,n-1)],'high','s');
    butter_sys = tf(B,A);
    [B,A] = butter(2,2*pi*[zeros(1,n)],'low','s');
    butter_sys1 = tf(B,A);
    sys_t(n) = sys*butter_sys*butter_sys1;

n = 8;
    freq = zeros(n) - poles(n).*0.000;
    omega = freq.*2.*pi;
    zeta = 0.08;
    num = [omega.^2];
    den = [1 2.*zeta.*omega omega.^2];
    sys = tf(num,den);
    [B,A] = butter(6,2*pi*[zeros(1,n-1)],'high','s');
    butter_sys = tf(B,A);
    [B,A] = butter(2,2*pi*[zeros(1,n)],'low','s');
    butter_sys1 = tf(B,A);
    sys_t(n) = sys*butter_sys*butter_sys1;

n = 9;
    freq = zeros(n) - poles(n).*0.000;
    omega = freq.*2.*pi;
    zeta = 0.08;
    num = [omega.^2];
    den = [1 2.*zeta.*omega omega.^2];
    sys = tf(num,den);
    [B,A] = butter(6,2*pi*[zeros(1,n-1)],'high','s');
    butter_sys = tf(B,A);
    [B,A] = butter(2,2*pi*[zeros(1,n)],'low','s');
    butter_sys1 = tf(B,A);
    sys_t(n) = sys*butter_sys*butter_sys1;

phaseOL = unwrap(angle(G)).*180./pi;
```

```
n = 8; p = n;
dummy = 5;

while n > 1
    half = 0;
    sys_total = g(1)*sys_t(1) + g(2)*sys_t(2) + g(3)*sys_t(3) + g(4)*sys_t(4) +
g(5)*sys_t(5) + g(6)*sys_t(6) + g(7)*sys_t(7) + g(8)*sys_t(8) + g(9)*sys_t(9);
    [mag,phase] = bode(sys_total,2*pi*f);
    mag = mag(:);     phase = phase(:);
    H = mag.*exp(i*phase*pi/180);      %  Coupled compensator
    PC_C = G./(1 + G.*H);           % Closed loop transfer function
    phasePC_C = unwrap(angle(PC_C)).*180./pi;

    if phaseOL > phasePC_C - 50
        g(n) = g(n).*10
        dummy = dummy - 1;
    else
        g(n) = g(n)./10

        while dummy < 5
                sys_total = g(1)*sys_t(1) + g(2)*sys_t(2) + g(3)*sys_t(3) + g(4)*sys_t(4)
+ g(5)*sys_t(5) + g(6)*sys_t(6) + g(7)*sys_t(7) + g(8)*sys_t(8) + g(9)*sys_t(9);
                [mag,phase] = bode(sys_total,2*pi*f);
                mag = mag(:);     phase = phase(:);
                H = mag.*exp(i*phase*pi/180); %  Coupled compensator
                PC_C = G./(1 + G.*H);   % Closed loop transfer function
                phasePC_C = unwrap(angle(PC_C)).*180./pi;

                if phaseOL > phasePC_C - 50
                    g(n) = g(n) + 10.^(-dummy)
                else
                    g(n) = g(n) - 10.^(-dummy)
                    dummy = dummy + 1;
                    half = 1;
                end
        end
        if half == 1;
            if n == p
                g(n) = g(n)./1.5
            elseif n == p - 1
                g(n) = g(n)./1.35
            else
            g(n) = g(n)./1.35
            end
        end
        n = n - 1;
    end
end

    sys_total = g(1)*sys_t(1) + g(2)*sys_t(2) + g(3)*sys_t(3) + g(4)*sys_t(4) +
g(5)*sys_t(5) + g(6)*sys_t(6) + g(7)*sys_t(7) + g(8)*sys_t(8) + g(9)*sys_t(9);
    [mag,phase] = bode(sys_total,2*pi*f);
    mag = mag(:);     phase = phase(:);
    H = mag.*exp(i*phase*pi/180);      %  Coupled compensator
    PC_C = G./(1 + G.*H);           % Closed loop transfer function
    magPC_C = abs(PC_C);
    phasePC_C = unwrap(angle(PC_C)).*180./pi;
    PC_C1 = PC_C.*G3;               % Closed loop transfer function
    magPC_C1 = abs(PC_C1);
    phasePC_C1 = unwrap(angle(PC_C1))*180/pi;
    PC_C2 = PC_C.*G4;               % Closed loop transfer function
    magPC_C2 = abs(PC_C2);
    phasePC_C2 = unwrap(angle(PC_C2))*180/pi;

figure
plot(f,20.*log10(abs(G)),f,20.*log10(magPC_C))
figure
plot(f,phaseOL,f,phasePC_C)
figure
plot(f,20.*log10(abs(G1)),f,20.*log10(magPC_C1))
phaseOL1 = unwrap(angle(G1)).*180./pi;
```

```
figure
plot(f,phaseOL1,f,phasePC_C1);
phaseOL2 = unwrap(angle(G2)).*180./pi;
figure
plot(f,20.*log10(abs(G2)),f,20.*log10(magPC_C2))
figure
plot(f,phaseOL2,f,phasePC_C2);
```

E.4 Simulink Adaptive Block Diagram

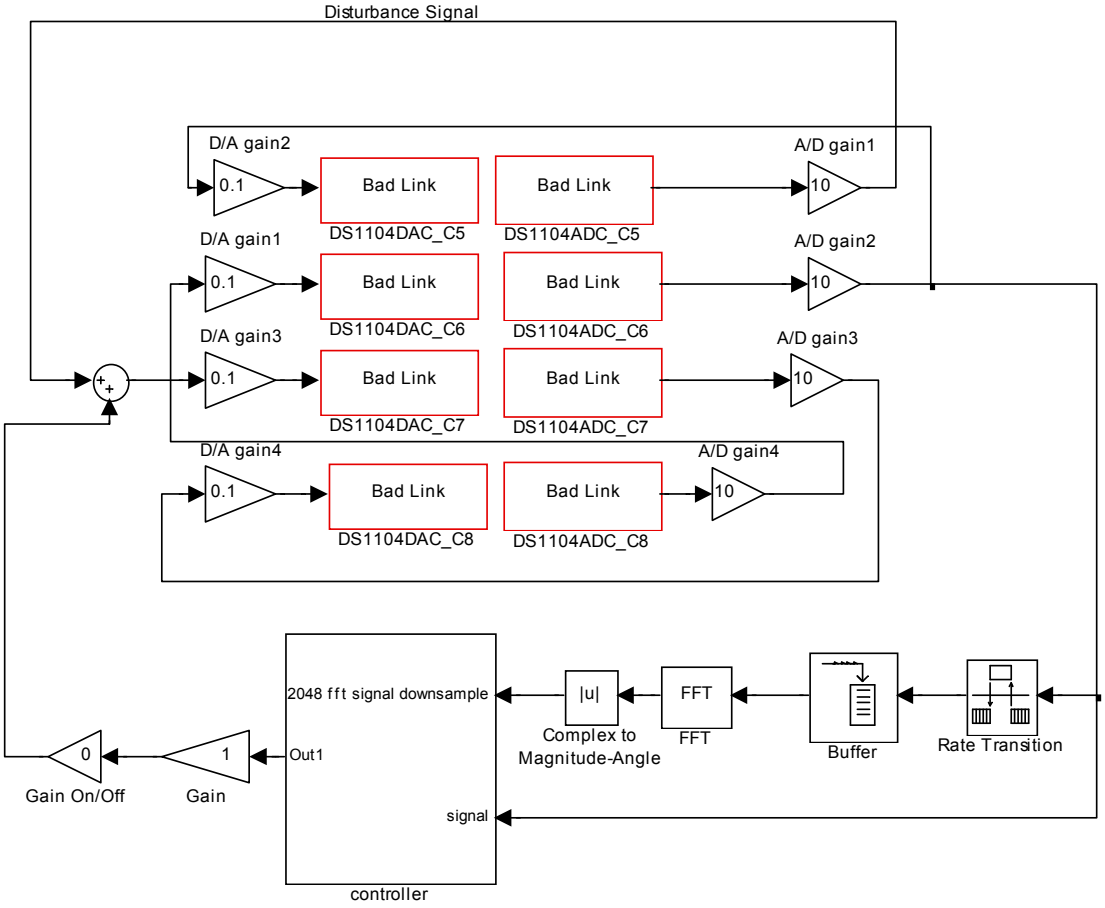

Figure E.1. Adaptive controller block diagram for Simulink.

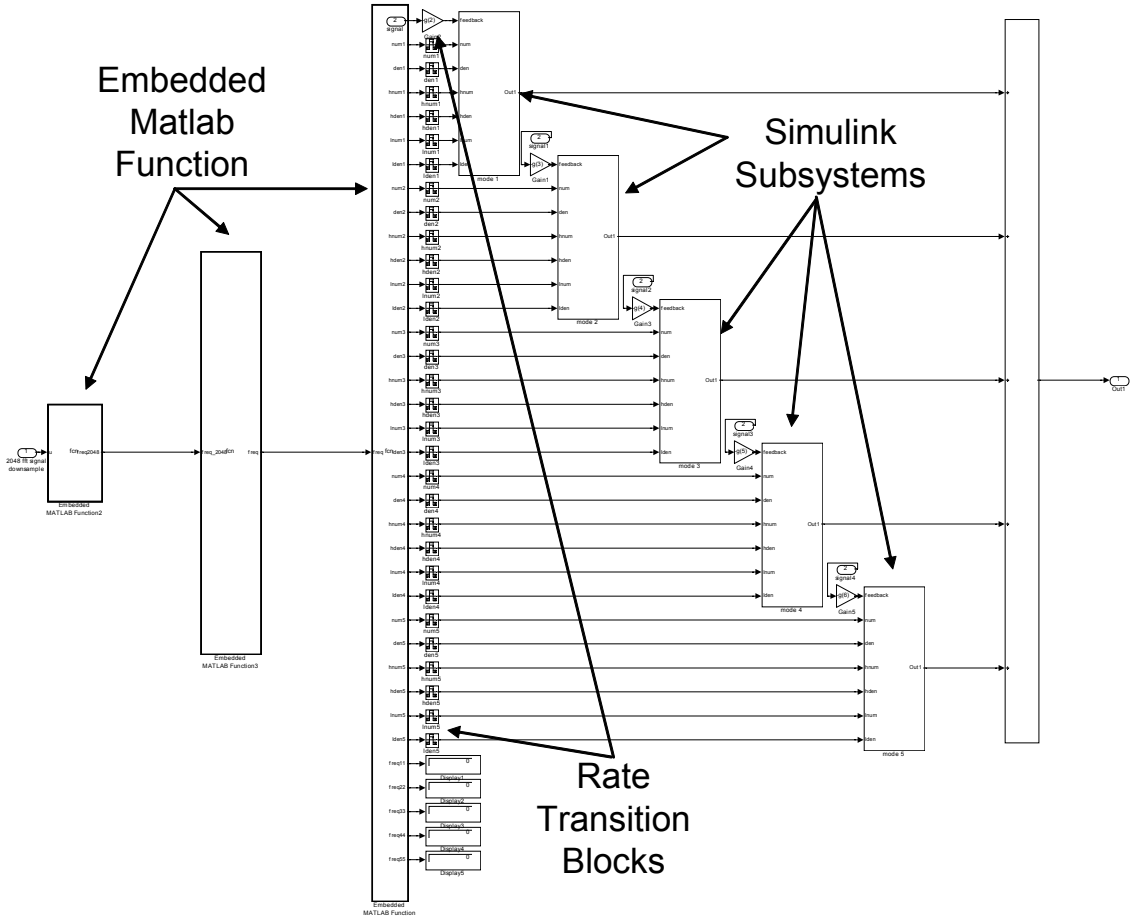

Figure E.2. Controller subsystem block from previous figure.

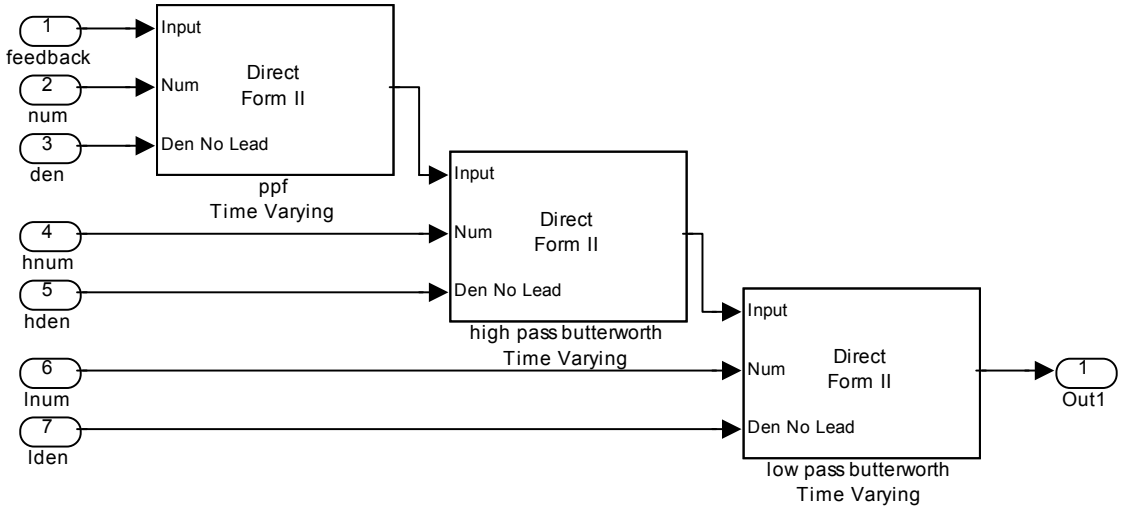

Figure E.3. Subsystem block from previous figure.

E.4.1 Embedded Matlab Function Code 1

This embedded matlab function finds the current zeros of the FFT data. The code is put into two columns to save space.

```
function freq2048     = fcn(u)
% This block supports an embeddable subset of the MATLAB language.
% See the help menu for details.

TT = 5000
buf = 2048
delay = 3
fs = 1/((delay/TT))
deltaf = fs/(buf - 1)
f = [0:deltaf:fs*deltaf];
freq = [149,243,339,436,531];
p = [149,243,339,436,531];
%finding the second pole
valuep11 = u(135:144)
[t,ff1] = max(valuep11)
valuep12 = u(150:195)
[t,ff2] = max(valuep12)
if valuep11(ff1) > valuep12(ff2)
    p(1) = f(ff1 + 135)
else
    p(1) = f(ff2 + 150)
end

%finding the third pole
valuep2 = u(240:305);
[t,ff] = max(valuep2);
p(2) = f(ff + 240);

%finding the fourth pole
valuep3 = u(355:440);
[t,ff] = max(valuep3);
p(3) = f(ff + 355);

%finding the fifth pole
valuep4 = u(470:570);
[t,ff] = max(valuep4);
p(4) = f(ff + 470);

%finding the sixth pole
valuep5 = u(585:685);
[t,ff] = max(valuep5);
p(5) = f(ff + 585);

%finding the third zero
    valuez2 = u(298:366)
    [t,ff] = min(valuez2)
    freq(2) = f(ff + 298)
    freq(2) = ((p(2) + p(2).*0.2) +
freq(2))./2
    x = (freq(2) - 240)./4.6635

%finding the second zero
if x <= 5
    valuez1 = u(165:190);
    [t,ff] = min(valuez1);
    freq(1) = f(ff + 165);
else
    valuez = u(175:235);
    [t,ff] = min(valuez);
    freq(1) = f(ff + 175);
end
freq(1) = ((p(1) + p(1)*0.28) +
freq(1))./2

%find the fourth zero
if x <=4.5
    valuez = u(405:465)
    [t,ff] = min(valuez)
    freq(3) = f(ff + 410)
elseif x <= 9
    valuez = u(440:500)
    [t,ff] = min(valuez)
    freq(3) = f(ff + 440)
else
    valuez = u(460:520)
    [t,ff] = min(valuez)
    freq(3) = f(ff + 460)
end
freq(3) = ((p(3) + p(3)*0.165) +
freq(3))./2

%find the fifth zero
if x <= 3.25
    valuez = u(525:585)
    [t,ff] = min(valuez)
    freq(4) = f(ff + 525)
elseif x <= 6.5
    valuez = u(555:615)
    [t,ff] = min(valuez)
    freq(4) = f(ff + 555)
elseif x <= 9.75
    valuez = u(575:635)
    [t,ff] = min(valuez)
    freq(4) = f(ff + 575)
else
    valuez = u(600:660)
    [t,ff] = min(valuez)
    freq(4) = f(ff + 600)
end
freq(4) = ((p(4) + p(4)*0.135) +
freq(4))./2

%finding the sixth zero
if x <= 3.25
    valuez = u(650:710)
    [t,ff] = min(valuez)
    freq(5) = f(ff + 650)
elseif x <= 6.5
    valuez = u(680:740)
    [t,ff] = min(valuez)
    freq(5) = f(ff + 680)
elseif x <= 9.75
    valuez = u(710:770)
    [t,ff] = min(valuez)
    freq(5) = f(ff + 710)
else
    valuez = u(750:810)
    [t,ff] = min(valuez)
    freq(5) = f(ff + 750)
end
freq(5) = ((p(5) + p(5)*0.12) +
freq(5))./2

x1 = (freq(2) - 240)/4.6635
```

```
x2 = (freq(3) - 335)/6.1538
x3 = (freq(4) - 430)/8.0769

xavg = (x1 + x2 + x3)/3

freq(1) = 2.9327*xavg + 145
freq(5) = 9.6154*xavg + 530

freq2048 = freq
```

E.4.2 Embedded Matlab Function Code 2

This embedded matlab function buffers the zeros values and averages 20 previous values with the current value. Some of the code is placed in columns for space purposes.

```
function freq     = fcn(freq_2048)
% This block supports an embeddable subset of the MATLAB language.
% See the help menu for details.
persistent freq11 freq21 freq31 freq41 freq51 freq12 freq22 freq32 freq42 freq52 freq13
freq23 freq33 freq43 freq53 freq14 freq24 freq34 freq44 freq54 freq15 freq25 freq35
freq45 freq55 freq16 freq26 freq36 freq46 freq56 freq17 freq27 freq37 freq47 freq57
freq18 freq28 freq38 freq48 freq58 freq19 freq29 freq39 freq49 freq59 freq110 freq210
freq310 freq410 freq510 freq111 freq211 freq311 freq411 freq511 freq112 freq212 freq312
freq412 freq512 freq113 freq213 freq313 freq413 freq513 freq114 freq214 freq314 freq414
freq514 freq115 freq215 freq315 freq415 freq515 freq116 freq216 freq316 freq416 freq516
freq117 freq217 freq317 freq417 freq517 freq118 freq218 freq318 freq418 freq518 freq119
freq219 freq319 freq419 freq519 freq120 freq220 freq320 freq420 freq520
if isempty(freq11)
    freq11 = 145;
end
if isempty(freq21)
    freq21 = 243;
end
if isempty(freq31)
    freq31 = 339;
end
if isempty(freq41)
    freq41 = 437;
end
if isempty(freq51)
    freq51 = 532;
end
if isempty(freq12)
    freq12 = 145;
end
if isempty(freq22)
    freq22 = 243;
end
if isempty(freq32)
    freq32 = 339;
end
if isempty(freq42)
    freq42 = 437;
end
if isempty(freq52)
    freq52 = 532;
end
if isempty(freq13)
    freq13 = 145;
end
if isempty(freq23)
    freq23 = 243;
end
if isempty(freq33)
    freq33 = 339;
end
if isempty(freq43)
    freq43 = 437;
end
if isempty(freq53)
    freq53 = 532;
end
if isempty(freq14)
    freq14 = 145;
end
if isempty(freq24)
    freq24 = 243;
end
if isempty(freq34)
    freq34 = 339;
end
if isempty(freq44)
    freq44 = 437;
end
if isempty(freq54)
    freq54 = 532;
end
if isempty(freq15)
    freq15 = 145;
end

if isempty(freq25)
    freq25 = 243;
end
if isempty(freq35)
    freq35 = 339;
end
if isempty(freq45)
    freq45 = 437;
end
if isempty(freq55)
    freq55 = 532;
end
if isempty(freq16)
    freq16 = 145;
end
if isempty(freq26)
    freq26 = 243;
end
if isempty(freq36)
    freq36 = 339;
end
if isempty(freq46)
    freq46 = 437;
end
if isempty(freq56)
    freq56 = 532;
end
if isempty(freq17)
    freq17 = 145;
end
if isempty(freq27)
    freq27 = 243;
end
if isempty(freq37)
    freq37 = 339;
end
if isempty(freq47)
    freq47 = 437;
end
if isempty(freq57)
    freq57 = 532;
end
if isempty(freq18)
    freq18 = 145;
end
if isempty(freq28)
    freq28 = 243;
end
if isempty(freq38)
    freq38 = 339;
end
if isempty(freq48)
    freq48 = 437;
end
if isempty(freq58)
    freq58 = 532;
end
if isempty(freq19)
    freq19 = 145;
end
if isempty(freq29)
    freq29 = 243;
end
if isempty(freq39)
    freq39 = 339;
end
if isempty(freq49)
    freq49 = 437;
end
if isempty(freq59)
    freq59 = 532;
end
if isempty(freq110)
    freq110 = 145;
```

```
end
if isempty(freq210)
    freq210 = 243;
end
if isempty(freq310)
    freq310 = 339;
end
if isempty(freq410)
    freq410 = 437;
end
if isempty(freq510)
    freq510 = 532;
end
if isempty(freq111)
    freq111 = 145;
end
if isempty(freq211)
    freq211 = 243;
end
if isempty(freq311)
    freq311 = 339;
end
if isempty(freq411)
    freq411 = 437;
end
if isempty(freq511)
    freq511 = 532;
end
if isempty(freq112)
    freq112 = 145;
end
if isempty(freq212)
    freq212 = 243;
end
if isempty(freq312)
    freq312 = 339;
end
if isempty(freq412)
    freq412 = 437;
end
if isempty(freq512)
    freq512 = 532;
end
if isempty(freq113)
    freq113 = 145;
end
if isempty(freq213)
    freq213 = 243;
end
if isempty(freq313)
    freq313 = 339;
end
if isempty(freq413)
    freq413 = 437;
end
if isempty(freq513)
    freq513 = 532;
end
if isempty(freq114)
    freq114 = 145;
end
if isempty(freq214)
    freq214 = 243;
end
if isempty(freq314)
    freq314 = 339;
end
if isempty(freq414)
    freq414 = 437;
end
if isempty(freq514)
    freq514 = 532;
end
if isempty(freq115)
    freq115 = 145;
end
if isempty(freq215)
    freq215 = 243;
end
if isempty(freq315)
    freq315 = 339;
end
if isempty(freq415)
    freq415 = 437;
end
if isempty(freq515)
    freq515 = 532;
end
if isempty(freq116)
    freq116 = 145;
end
if isempty(freq216)
    freq216 = 243;
end
if isempty(freq316)
    freq316 = 339;
end
if isempty(freq416)
    freq416 = 437;
end
if isempty(freq516)
    freq516 = 532;
end
if isempty(freq117)
    freq117 = 145;
end
if isempty(freq217)
    freq217 = 243;
end
if isempty(freq317)
    freq317 = 339;
end
if isempty(freq417)
    freq417 = 437;
end
if isempty(freq517)
    freq517 = 532;
end
if isempty(freq118)
    freq118 = 145;
end
if isempty(freq218)
    freq218 = 243;
end
if isempty(freq318)
    freq318 = 339;
end
if isempty(freq418)
    freq418 = 437;
end
if isempty(freq518)
    freq518 = 532;
end
if isempty(freq119)
    freq119 = 145;
end
if isempty(freq219)
    freq219 = 243;
end
if isempty(freq319)
    freq319 = 339;
end
if isempty(freq419)
    freq419 = 437;
end
if isempty(freq519)
    freq519 = 532;
end
if isempty(freq120)
    freq120 = 145;
end
if isempty(freq220)
    freq220 = 243;
end
if isempty(freq320)
    freq320 = 339;
end
if isempty(freq420)
    freq420 = 437;
end
if isempty(freq520)
    freq520 = 532;
end
freq = [149,243,339,436,531];
freq(1) = (freq_2048(1))
freq(2) = (freq_2048(2))
freq(3) = (freq_2048(3))
freq(4) = (freq_2048(4))
freq(5) = (freq_2048(5))
a = freq(1)
b = freq(2)
c = freq(3)
d = freq(4)
e = freq(5)
freq(1) = (freq(1) + freq11 + freq12 + freq13 + freq14 + freq15 + freq16 + freq17 +
freq18 + freq19 + freq110 + freq111 + freq112 + freq113 + freq114 + freq115 + freq116 +
freq117 + freq118 + freq119 + freq120)./21
```

```
freq(2) = (freq(2) + freq21 + freq22 + freq23 + freq24 + freq25 + freq26 + freq27 +
freq28 + freq29 + freq210 + freq211 + freq212 + freq213 + freq214 + freq215 + freq216 +
freq217 + freq218 + freq219 + freq220)./21
freq(3) = (freq(3) + freq31 + freq32 + freq33 + freq34 + freq35 + freq36 + freq37 +
freq38 + freq39 + freq310 + freq311 + freq312 + freq313 + freq314 + freq315 + freq316 +
freq317 + freq318 + freq319 + freq320)./21
freq(4) = (freq(4) + freq41 + freq42 + freq43 + freq44 + freq45 + freq46 + freq47 +
freq48 + freq49 + freq410 + freq411 + freq412 + freq413 + freq414 + freq415 + freq416 +
freq417 + freq418 + freq419 + freq420)./21
freq(5) = (freq(5) + freq51 + freq52 + freq53 + freq54 + freq55 + freq56 + freq57 +
freq58 + freq59 + freq510 + freq511 + freq512 + freq513 + freq514 + freq515 + freq516 +
freq517 + freq518 + freq519 + freq520)./21

freq120 = freq119
freq220 = freq219
freq320 = freq319
freq420 = freq419
freq520 = freq519

freq119 = freq118
freq219 = freq218
freq319 = freq318
freq419 = freq418
freq519 = freq518

freq118 = freq117
freq218 = freq217
freq318 = freq317
freq418 = freq417
freq518 = freq517

freq117 = freq116
freq217 = freq216
freq317 = freq316
freq417 = freq416
freq517 = freq516

freq116 = freq115
freq216 = freq215
freq316 = freq315
freq416 = freq415
freq516 = freq515

freq115 = freq114
freq215 = freq214
freq315 = freq314
freq415 = freq414
freq515 = freq514

freq114 = freq113
freq214 = freq213
freq314 = freq313
freq414 = freq413

freq514 = freq513

freq113 = freq112
freq213 = freq212
freq313 = freq312
freq413 = freq412
freq513 = freq512

freq112 = freq111
freq212 = freq211
freq312 = freq311
freq412 = freq411
freq512 = freq511

freq111 = freq110
freq211 = freq210
freq311 = freq310
freq411 = freq410
freq511 = freq510

freq110 = freq19
freq210 = freq29
freq310 = freq39
freq410 = freq49
freq510 = freq59

freq19 = freq18
freq29 = freq28
freq39 = freq38
freq49 = freq48
freq59 = freq58

freq18 = freq17
freq28 = freq27
freq38 = freq37
freq48 = freq47
freq58 = freq57

freq17 = freq16
freq27 = freq26

freq37 = freq36
freq47 = freq46
freq57 = freq56

freq16 = freq15
freq26 = freq25
freq36 = freq35
freq46 = freq45
freq56 = freq55

freq15 = freq14
freq25 = freq24
freq35 = freq34
freq45 = freq44
freq55 = freq54

freq14 = freq13
freq24 = freq23
freq34 = freq33
freq44 = freq43
freq54 = freq53

freq13 = freq12
freq23 = freq22
freq33 = freq32
freq43 = freq42
freq53 = freq52

freq12 = freq11
freq22 = freq21
freq32 = freq31
freq42 = freq41
freq52 = freq51

freq11 = a
freq21 = b
freq31 = c
freq41 = d
freq51 = e
```

E.4.3 Embedded Matlab Function Code 3

This embedded matlab function sets all of the vectors for the numerators and denominators of the transfer functions for the controller where the vectors are sent to time varying transfer function blocks for controlling 5 modes.

```
function
[num1,den1,hnum1,hden1,lnum1,lden1,num2,den2,hnum2,hden2,lnum2,lden2,num3,den3,hnum3,hden
3,lnum3,lden3,num4,den4,hnum4,hden4,lnum4,lden4,num5,den5,hnum5,hden5,lnum5,lden5,freq11,
freq22,freq33,freq44,freq55]    = fcn(freq)
% This block supports an embeddable subset of the MATLAB language.
% See the help menu for details.
TT = 5000
%freq = [149,243,339,436,531];
```

```
freq11 = freq(1)
freq22 = freq(2)
freq33 = freq(3)
freq44 = freq(4)
freq55 = freq(5)

    freq2 = 2*pi*(freq11 - freq11*0.04);
    freq3 = 2*pi*(freq22 - freq22*0.04);
    freq4 = 2*pi*(freq33 - freq33*0.04);
    freq5 = 2*pi*(freq44 - freq44*0.04);
    freq6 = 2*pi*(freq55 - freq55*0.04);

%setting constants
zeta = 0.08;
T = 1/TT;
    a = sin(15*pi/180) + sin(45*pi/180) + sin(75*pi/180)
    b = 3 + 4*sin(15*pi/180)*sin(45*pi/180) + 4*sin(15*pi/180)*sin(75*pi/180) +
4*sin(45*pi/180)*sin(75*pi/180)
    c = 2*sin(15*pi/180) + 2*sin(45*pi/180) + 2*sin(75*pi/180) +
4*sin(15*pi/180)*sin(45*pi/180)*sin(75*pi/180)

%first mode controller
freq1 = 2*pi*53;
    A = 64/T^6 + 64*freq1*a/T^5 + 16*freq1^2*b/T^4 + 16*freq1^3*c/T^3 + 4*freq1^4*b/T^2 +
4*freq1^5*a/T + freq1^6
    B = -384/T^6 - 256*freq1*a/T^5 - 32*freq1^2*b/T^4 + 8*freq1^4*b/T^2 + 16*freq1^5*a/T
+ 6*freq1^6
    C = 960/T^6 + 320*freq1*a/T^5 - 16*freq1^2*b/T^4 - 48*freq1^3*c/T^3 - 4*freq1^4*b/T^2
+ 20*freq1^5*a/T + 15*freq1^6
    D = -1280/T^6 + 64*freq1^2*b/T^4 - 16*freq1^4*b/T^2 + 20*freq1^6
    E = 960/T^6 - 320*freq1*a/T^5 - 16*freq1^2*b/T^4 + 48*freq1^3*c/T^3 - 4*freq1^4*b/T^2
- 20*freq1^5*a/T + 15*freq1^6
    F = -384/T^6 + 256*freq1*a/T^5 - 32*freq1^2*b/T^4 + 8*freq1^4*b/T^2 - 16*freq1^5*a/T
+ 6*freq1^6
    G = 64/T^6 - 64*freq1*a/T^5 + 16*freq1^2*b/T^4 - 16*freq1^3*c/T^3 + 4*freq1^4*b/T^2 -
4*freq1^5*a/T + freq1^6

    d = (4/T^2 + 4*zeta*freq2/T + freq2^2);
    y1 = [freq2^2/d 2*freq2^2/d freq2^2/d];
    y2 = [(-8/T^2 + 2*freq2^2)/d (4/T^2 - 4*zeta*freq2/T + freq2^2)/d]
    %high pass filter (use lower zero value)
     den = A*T^6
     hnum1 = [64/den -384/den 960/den -1280/den 960/den -384/den 64/den]
     hden1 = [B/A C/A D/A E/A F/A G/A]
     %low pass filter and ppf (use higher zero value)
     num1 = y1;
     den1 = y2;

     den = (4/T^2 + 2*sqrt(2)*freq2/T + freq2^2)
     lnum1 = [freq2^2/den 2*freq2^2/den freq2^2/den]
     lden1 = [(-8/T^2 + 2*freq2^2)/den (4/T^2 - 2*sqrt(2)*freq2/T + freq2^2)/den]

 %second mode controller

    A = 64/T^6 + 64*freq2*a/T^5 + 16*freq2^2*b/T^4 + 16*freq2^3*c/T^3 + 4*freq2^4*b/T^2 +
4*freq2^5*a/T + freq2^6
    B = -384/T^6 - 256*freq2*a/T^5 - 32*freq2^2*b/T^4 + 8*freq2^4*b/T^2 + 16*freq2^5*a/T
+ 6*freq2^6
    C = 960/T^6 + 320*freq2*a/T^5 - 16*freq2^2*b/T^4 - 48*freq2^3*c/T^3 - 4*freq2^4*b/T^2
+ 20*freq2^5*a/T + 15*freq2^6
    D = -1280/T^6 + 64*freq2^2*b/T^4 - 16*freq2^4*b/T^2 + 20*freq2^6
    E = 960/T^6 - 320*freq2*a/T^5 - 16*freq2^2*b/T^4 + 48*freq2^3*c/T^3 - 4*freq2^4*b/T^2
- 20*freq2^5*a/T + 15*freq2^6
    F = -384/T^6 + 256*freq2*a/T^5 - 32*freq2^2*b/T^4 + 8*freq2^4*b/T^2 - 16*freq2^5*a/T
+ 6*freq2^6
    G = 64/T^6 - 64*freq2*a/T^5 + 16*freq2^2*b/T^4 - 16*freq2^3*c/T^3 + 4*freq2^4*b/T^2 -
4*freq2^5*a/T + freq2^6

    d = (4/T^2 + 4*zeta*freq3/T + freq3^2);
    y1 = [freq3^2/d 2*freq3^2/d freq3^2/d];
    y2 = [(-8/T^2 + 2*freq3^2)/d (4/T^2 - 4*zeta*freq3/T + freq3^2)/d]
```

```
    %high pass filter (use lower zero value)
     den = A*T^6
     hnum2 = [64/den -384/den 960/den -1280/den 960/den -384/den 64/den]
     hden2 = [B/A C/A D/A E/A F/A G/A]
     %low pass filter and ppf (use higher zero value)
     num2 = y1;
     den2 = y2;
     den = (4/T^2 + 2*sqrt(2)*freq3/T + freq3^2)
     lnum2 = [freq3^2/den 2*freq3^2/den freq3^2/den]
     lden2 = [(-8/T^2 + 2*freq3^2)/den (4/T^2 - 2*sqrt(2)*freq3/T + freq3^2)/den]

 %third mode controller

    A = 64/T^6 + 64*freq3*a/T^5 + 16*freq3^2*b/T^4 + 16*freq3^3*c/T^3 + 4*freq3^4*b/T^2 +
4*freq3^5*a/T + freq3^6
    B = -384/T^6 - 256*freq3*a/T^5 - 32*freq3^2*b/T^4 + 8*freq3^4*b/T^2 + 16*freq3^5*a/T
+ 6*freq3^6
    C = 960/T^6 + 320*freq3*a/T^5 - 16*freq3^2*b/T^4 - 48*freq3^3*c/T^3 - 4*freq3^4*b/T^2
+ 20*freq3^5*a/T + 15*freq3^6
    D = -1280/T^6 + 64*freq3^2*b/T^4 - 16*freq3^4*b/T^2 + 20*freq3^6
    E = 960/T^6 - 320*freq3*a/T^5 - 16*freq3^2*b/T^4 + 48*freq3^3*c/T^3 - 4*freq3^4*b/T^2
- 20*freq3^5*a/T + 15*freq3^6
    F = -384/T^6 + 256*freq3*a/T^5 - 32*freq3^2*b/T^4 + 8*freq3^4*b/T^2 - 16*freq3^5*a/T
+ 6*freq3^6
    G = 64/T^6 - 64*freq3*a/T^5 + 16*freq3^2*b/T^4 - 16*freq3^3*c/T^3 + 4*freq3^4*b/T^2 -
4*freq3^5*a/T + freq3^6

    d = (4/T^2 + 4*zeta*freq4/T + freq4^2);
    y1 = [freq4^2/d 2*freq4^2/d freq4^2/d];
    y2 = [(-8/T^2 + 2*freq4^2)/d (4/T^2 - 4*zeta*freq4/T + freq4^2)/d]
    %high pass filter (use lower zero value)
     den = A*T^6
     hnum3 = [64/den -384/den 960/den -1280/den 960/den -384/den 64/den]
     hden3 = [B/A C/A D/A E/A F/A G/A]
     %low pass filter and ppf (use higher zero value)
     num3 = y1;
     den3 = y2;

     den = (4/T^2 + 2*sqrt(2)*freq4/T + freq4^2)
     lnum3 = [freq4^2/den 2*freq4^2/den freq4^2/den]
     lden3 = [(-8/T^2 + 2*freq4^2)/den (4/T^2 - 2*sqrt(2)*freq4/T + freq4^2)/den]

 %forth mode controller

    A = 64/T^6 + 64*freq4*a/T^5 + 16*freq4^2*b/T^4 + 16*freq4^3*c/T^3 + 4*freq4^4*b/T^2 +
4*freq4^5*a/T + freq4^6
    B = -384/T^6 - 256*freq4*a/T^5 - 32*freq4^2*b/T^4 + 8*freq4^4*b/T^2 + 16*freq4^5*a/T
+ 6*freq4^6
    C = 960/T^6 + 320*freq4*a/T^5 - 16*freq4^2*b/T^4 - 48*freq4^3*c/T^3 - 4*freq4^4*b/T^2
+ 20*freq4^5*a/T + 15*freq4^6
    D = -1280/T^6 + 64*freq4^2*b/T^4 - 16*freq4^4*b/T^2 + 20*freq4^6
    E = 960/T^6 - 320*freq4*a/T^5 - 16*freq4^2*b/T^4 + 48*freq4^3*c/T^3 - 4*freq4^4*b/T^2
- 20*freq4^5*a/T + 15*freq4^6
    F = -384/T^6 + 256*freq4*a/T^5 - 32*freq4^2*b/T^4 + 8*freq4^4*b/T^2 - 16*freq4^5*a/T
+ 6*freq4^6
    G = 64/T^6 - 64*freq4*a/T^5 + 16*freq4^2*b/T^4 - 16*freq4^3*c/T^3 + 4*freq4^4*b/T^2 -
4*freq4^5*a/T + freq4^6

    d = (4/T^2 + 4*zeta*freq5/T + freq5^2);
    y1 = [freq5^2/d 2*freq5^2/d freq5^2/d];
    y2 = [(-8/T^2 + 2*freq5^2)/d (4/T^2 - 4*zeta*freq5/T + freq5^2)/d]
    %high pass filter (use lower zero value)
     den = A*T^6
     hnum4 = [64/den -384/den 960/den -1280/den 960/den -384/den 64/den]
     hden4 = [B/A C/A D/A E/A F/A G/A]
     %low pass filter and ppf (use higher zero value)
     num4 = y1;
     den4 = y2;

     den = (4/T^2 + 2*sqrt(2)*freq5/T + freq5^2)
     lnum4 = [freq5^2/den 2*freq5^2/den freq5^2/den]
```

```
     lden4 = [(-8/T^2 + 2*freq5^2)/den (4/T^2 - 2*sqrt(2)*freq5/T + freq5^2)/den]

 %fifth mode controller

    A = 64/T^6 + 64*freq5*a/T^5 + 16*freq5^2*b/T^4 + 16*freq5^3*c/T^3 + 4*freq5^4*b/T^2 +
4*freq5^5*a/T + freq5^6
    B = -384/T^6 - 256*freq5*a/T^5 - 32*freq5^2*b/T^4 + 8*freq5^4*b/T^2 + 16*freq5^5*a/T
+ 6*freq5^6
    C = 960/T^6 + 320*freq5*a/T^5 - 16*freq5^2*b/T^4 - 48*freq5^3*c/T^3 - 4*freq5^4*b/T^2
+ 20*freq5^5*a/T + 15*freq5^6
    D = -1280/T^6 + 64*freq5^2*b/T^4 - 16*freq5^4*b/T^2 + 20*freq5^6
    E = 960/T^6 - 320*freq5*a/T^5 - 16*freq5^2*b/T^4 + 48*freq5^3*c/T^3 - 4*freq5^4*b/T^2
- 20*freq5^5*a/T + 15*freq5^6
    F = -384/T^6 + 256*freq5*a/T^5 - 32*freq5^2*b/T^4 + 8*freq5^4*b/T^2 - 16*freq5^5*a/T
+ 6*freq5^6
    G = 64/T^6 - 64*freq5*a/T^5 + 16*freq5^2*b/T^4 - 16*freq5^3*c/T^3 + 4*freq5^4*b/T^2 -
4*freq5^5*a/T + freq5^6

    d = (4/T^2 + 4*zeta*freq6/T + freq6^2);
    y1 = [freq6^2/d 2*freq6^2/d freq6^2/d];
    y2 = [(-8/T^2 + 2*freq6^2)/d (4/T^2 - 4*zeta*freq6/T + freq6^2)/d]
    %high pass filter (use lower zero value)
     den = A*T^6
     hnum5 = [64/den -384/den 960/den -1280/den 960/den -384/den 64/den]
     hden5 = [B/A C/A D/A E/A F/A G/A]
     %low pass filter and ppf (use higher zero value)
     num5 = y1;
     den5 = y2;
     den = (4/T^2 + 2*sqrt(2)*freq6/T + freq6^2)
     lnum5 = [freq6^2/den 2*freq6^2/den freq6^2/den]
     lden5 = [(-8/T^2 + 2*freq6^2)/den (4/T^2 - 2*sqrt(2)*freq6/T + freq6^2)/den]
```

Vita

M. Austin Creasy was born on June 18, 1978 to Miles and Wanda Creasy of Charlottesville, Virginia. He graduated from Fluvanna County High School in June of 1996 and began his college education at Virginia Tech in August of that year. In August of 1997 he took a break from school to serve as a missionary for The Church of Jesus Christ of Latter-day Saints in Guayaquil Ecuador until August of 1999. He returned to Virginia Tech in August of 1999 to study Mechanical Engineering. In August of 2000 he was married to Mary Crystal Danielson of Florence, Oregon and they are now the parents of two daughters. In May of 2002 he graduated Cum Laude with a Bachelor of Science in Mechanical Engineering and started working for Energetics, Inc in Columbia, Maryland in July of 2002 as a Junior Mechanical Engineer. In August of 2004 he returned to Virginia Tech to start his graduate studies as a Graduate Teaching Assistant and began his Master's research in January of 2005 under Dr. Donald Leo with the Center for Intelligent Material Systems and Structures (CIMSS) in the area of acoustic control of enclosures.

Address: Center for Intelligent Material Systems and Structures
310 Durham Hall
Blacksburg, Va. 24061